Ravi Raghunathan
_____
Candidate

Optical Science and Engineering (Physics)
_____
Department

This dissertation is approved, and it is acceptable in quality and form for publication:

Approved by the Dissertation Committee:

Luke F. Lester, Chairperson
_____

Sudhakar Prasad
_____

Ganesh Balakrishnan
_____

Frederic Grillot
_____

_____

_____

_____

_____

THEORETICAL AND EXPERIMENTAL INVESTIGATION OF THE

NONLINEAR DYNAMICAL TRENDS OF PASSIVELY MODE-LOCKED

QUANTUM DOT LASERS

by

RAVI RAGHUNATHAN

B. A. Sc. (Honours), Electrical Engineering, University of Windsor,
Canada, 2003
M.S., Electrical Engineering (Electrophysics), University of Southern
California, USA, 2006
M.S., Optical Science and Engineering, University of New Mexico,
USA, 2010

DISSERTATION

Submitted in Partial Fulfillment of the
Requirements for the Degree of

Doctor of Philosophy
Optical Science and Engineering

The University of New Mexico
Albuquerque, New Mexico

July, 2013

<u>DEDICATION</u>

To Mom, Dad, Jyotsna, Deepak and Vaishnavi – your boundless and unending

love, support and encouragement mean everything to me, and words cannot

express how thankful I am for all that you have done for me.

ACKNOWLEDGEMENTS

I would like to start by expressing my heartfelt gratitude and deepest appreciation for my research advisor and dissertation committee Chair, Professor Luke F. Lester. His expert guidance, insights, support and encouragement have helped me greatly during the course of my graduate research here, and the skills and techniques I have learned as his student are sure to benefit me in my future endeavors.

Special thanks are also due to my dissertation committee members, Professor Sudhakar Prasad, Professor Ganesh Balakrishnan and Professor Frédéric Grillot, whose help and insightful suggestions have greatly assisted in the timely completion of this work.

My sincere thanks and gratitude also go to Dr. Vassilios Kovanis at the Air Force Research Laboratory, Wright – Patterson Air Force Base for numerous highly insightful and stimulating discussions relating to the mathematical modeling and numerical simulation of nonlinear dynamics in semiconductor lasers. In addition, I am extremely grateful to Dr. Mark Crowley, Jesse Mee, Dr. Chang-Yi Lin, Dr. Yan Li, Dr. Alexandre Braga and Dr. Antonio Hurtado for their help and collaboration on various aspects of the theoretical and experimental studies constituting this work, and to Ms. Susan Pinter for her assistance in formatting the manuscript. I would also like to thank Dr. Thomas Rotter, Nassim Rahimi, David Murrell, Huiwen Xu, Jing Ju, Nishant Patel, and all my other friends and colleagues for their friendship and support throughout my time here.

Above all, I will be forever indebted to my mother, Dr. Vaijayanthi Raghunathan, father, Dr. Parthasarathy Raghunathan, sister, Jyotsna, brother-in-law, Deepak and my beloved niece, Vaishnavi for their unbounded love, unwavering support and constant encouragement over the years.

THEORETICAL AND EXPERIMENTAL INVESTIGATION OF THE NONLINEAR DYNAMICAL TRENDS OF PASSIVELY MODE-LOCKED QUANTUM DOT LASERS

by

RAVI RAGHUNATHAN

B. A. Sc. (Honours), Electrical Engineering, University of Windsor,
Canada, 2003
M.S., Electrical Engineering (Electrophysics), University of Southern
California, USA, 2006
M.S., Optical Science and Engineering, University of New Mexico,
USA, 2010
Ph. D., Optical Science and Engineering, University of New Mexico, USA, 2013

ABSTRACT

In recent years, passively mode-locked quantum dot lasers have shown great promise as compact, efficient and reliable pulsed sources of light for a range of precision and high performance applications, such as high bit-rate optical communications, diverse waveform generation, metrology, and clock distribution in high-performance computing (HPC) processors. For such applications, stable optical pulses with short picosecond pulse durations and multi-gigahertz repetition rates are required. In addition, a low pulse-to-pulse timing jitter is also necessary to prevent errors arising from the ambiguity between neighboring pulses. In order to optimize pulse quality in terms of optical characteristics such as pulse shape and pulse train behavior, as well as RF characteristics such as phase noise and timing jitter, understanding the nonlinear output dynamics of

such devices is of critical importance, not only to get a sense of the regimes of operation where device output might be stable or unstable, but also to gain insight into the parameters that influence the output characteristics the most, and how they can be accessed and exploited to optimize design and performance for next generation applications.

In this dissertation, theoretical and experimental studies have been combined to investigate the dynamical trends of two-section passively mode-locked quantum dot lasers. On the theoretical side, a novel numerical modeling scheme is presented as a powerful and versatile framework to study the nonlinear dynamics specific to a device, with device-specific parameters extracted over a range of operating conditions. The practical utility of this scheme is then demonstrated, first, in an analytical capability to interpret and explain dynamical trends observed in experiment, and subsequently, as a predictive tool to guide experiment to operate in a desired dynamical regime. Modeling results are compared to experimental findings where possible. Finally, optical feedback from an external reflector is experimentally studied as an additional control mechanism over the output dynamics of the device, and shown to enable invaluable insight into the behavior of the RF and optical spectra of the output. Together, the theoretical and experimental findings of this dissertation are shown to offer a systematic approach to understand, control and exploit the dynamical trends of passively mode-locked two-section quantum dot lasers.

TABLE OF CONTENTS

List of Figures

List of Tables

Publications Associated with This Dissertation

Journal Articles

i. **R. Raghunathan**, M. T. Crowley, F. Grillot, Y. Li, J. K. Mee, V. Kovanis, and L. F. Lester, "Pulse Characterization of Passively Mode-Locked Quantum-Dot Lasers Using a Delay Differential Equation Model Seeded With Measured Parameters," IEEE Journal of Selected Topics in Quantum Electronics, vol.19, no.4, pp.1100311,1100311, July-Aug. 2013.

ii. J. K. Mee, M. Crowley, D. Murrell, **R. Raghunathan**, and L. F. Lester, "Temperature Performance of Monolithic Passively Mode-Locked Quantum Dot Lasers: Experiments and Analytical Modeling," IEEE Journal of Selected Topics in Quantum Electronics,, vol.19, no.4, pp.1101110,1101110, July-Aug. 2013.

iii. J. K. Mee, M. T. Crowley, N. Patel, D. Murrell, **R. Raghunathan**, A. Aboketaf, A. Elshaari, S. F. Preble, P. Ampadu, and L. F. Lester, "A passively mode-locked quantum-dot laser operating over a broad temperature range" App. Phys. Lett. vol.101, no.7, pp. 071112-1 - 071112-4 (2012).

iv. F. Grillot, N. A. Naderi, J. B. Wright, **R. Raghunathan**, M. T. Crowley and L. F. Lester, A dual-mode quantum dot laser operating in the excited state, Applied Physics Letters, Vol. 99, 23, pp. 1110-1113 (2011).

v. C.-Y. Lin, F. Grillot, N. A. Naderi, Y. Li, **R. Raghunathan** and L. F. Lester, Microwave Characterization and Stabilization of Timing Jitter in a Quantum-Dot

Passively Mode-Locked Laser via External Optical Feedback, IEEE Journal of Selected Topics in Quantum Electronics, Vol. 17, 5, pp. 1311-1317 (2011).

vi.   C.-Y. Lin, F. Grillot, Y. Li, **R. Raghunathan** and L. F. Lester, Characterization of timing jitter in a 5 GHz quantum dot passively mode-locked laser, Optics Express, Vol. 18, pp. 21932-21937 (2010).

Conference Publications

i.   **R. Raghunathan**, A. Braga, M. T. Crowley, J. K. Mee, and L. F. Lester, "Dynamics of Split-Pulsing in a Two-Section Passively Mode Locked Quantum Dot Laser," in CLEO: 2013, OSA Technical Digest (online) (Optical Society of America, 2013), paper JTh2A.112.

ii.   **R. Raghunathan**, J. K. Mee, M. T. Crowley, F. Grillot, V. I. Kovanis and L. F. Lester, "Modeling and characterization of pulse shape and pulse train dynamics in two-section passively mode-locked quantum dot lasers ", *Proc. SPIE* 8619, Physics and Simulation of Optoelectronic Devices XXI.

iii.   **R. Raghunathan**, F. Grillot, M. T. Crowley, V. Kovanis, N. G. Usechak and L. F. Lester, Enhanced temperature performance of a quantum dot nanostructure mode-locked laser operating under external control, Semiconductor and Integrated Optoelectronics (SIOE), Cardiff, April 2-4, Wales, UK, 2012.

iv.   **R. Raghunathan**, M. T. Crowley, F. Grillot, S. D. Mukherjee, N. G. Usechak, V. Kovanis, Luke F. Lester, "Delay differential equation-based modeling of

passively mode-locked quantum dot lasers using measured gain and loss spectra",
Proc. SPIE 8255, Physics and Simulation of Optoelectronic Devices XX.

v. **R. Raghunathan**, M. Crowley, F. Grillot, V. Kovanis and L. F. Lester, Direct Characterization of Carrier Relaxation in a Passively Mode-Locked Quantum Dot Laser, (*Oral Presentation*), The 24th Photonics Society Meeting, Arlington, 9-13 October, USA, 2011**.**

vi. J. K. Mee, **R. Raghunathan**, D. Murrell, M. T. Crowley and L. F. Lester, "Expanded Operational Range in Quantum Dot Passively Mode-Locked Lasers with Low Unsaturated Absorption", CLEO: Science and Innovations, 2013.

vii. J. K. Mee, M. T. Crowley, **R. Raghunathan**, D. Murrell and L. F. Lester," Characteristics of passively mode-locked quantum dot lasers from 20 to 120°C ", *Proc. SPIE* 8619, Physics and Simulation of Optoelectronic Devices XXI.

viii. J. K. Mee, M. T. Crowley, N. Patel, D. Murrell, **R. Raghunathan**, A. Aboketaf, A. Elshaari, S. F. Preble, P. Ampadu, L. F. Lester, 110℃ Operation of monolithic quantum dot passively mode-locked lasers", 23rd IEEE International Semiconductor Laser Conference (ISLC), 2012.

ix. D. Murrell, M. T. Crowley, M. Breivik, **R. Raghunathan,** J. K. Mee, A. Aboketaf, A. Elshaara, S. F. Preble, B. O. Fimland, P. Ampadu, and L. F. Lester, "Design of High-Bandwidth Ultra-Low Energy per Bit Quantum Dot Laser Transmitters for Chip to Chip Optical Interconnects," IEEE Optical Interconnects Conf., Santa Fe, New Mexico, 2012.

x.   F. Grillot, N. A. Naderi, J. Wright, N. Rahimi, **R. Raghunathan**, M. Crowley and L. F. Lester, Dual-Mode Quantum Dot Laser Operating in the Excited State, (*Oral Presentation*), The 24th Photonics Society Meeting, Arlington, 9-13 October, USA, 2011.

xi.   C.-Y. Lin, F. Grillot, Y. Li, **R. Raghunathan**, and L. F. Lester, Characterization of timing jitter in a quantum dot passively mode-locked laser at low offset frequency, (*Oral Presentation*), The 23rd Photonics Society Annual Meeting, Denver, 7-11 November, USA, 2010.

Chapter 1

Introduction

Semiconductor lasers represent the most common type of laser in use today, with a range of applications spanning diverse fields of application from ultrafast optical communications, optical data storage and spectroscopy, to medical imaging and environmental sensing, among others. Depending upon their structural composition and operating conditions, they exhibit a rich diversity in their output dynamics. Extensive theoretical and experimental studies over the past five decades have sought to improve device performance and reliability using two broad approaches – i.) through improvements in materials growth/processing techniques, and designing and engineering better laser cavity structures, and ii.) using an external control mechanism to manipulate output device dynamics, while in operation.

The materials growth, processing and device design aspect of performance enhancement has seen numerous achievements since the early sixties. Following the first demonstrations of p-n junction GaAs lasers in 1962 [1, 2], which were plagued by very low output efficiencies due to the high optical and electrical losses, significant performance improvements were achieved with the double heterostructure (DH), whereby, improved carrier confinement was achieved by sandwiching a relatively narrow bandgap layer between two layers of more broadband material [3, 4]. This led to a drastic reduction of threshold current density in such devices, along with stable continuous wave emission at room temperature.

The next key milestone was the realization of the power of confining carriers in lower dimensional structures. As dimensionality decreases, the density of states function transitions from continuous or quasi-continuous to a discretized form. For a given energy range, the number of carriers required to fill-out the available states reduces substantially with a decrease in dimensionality, which makes it easier for the device to achieve transparency, and eventually, population inversion for stimulated emission [5]. This paved the way for the demonstration of the first quantum well (QW) structure in 1978 by Dupuis et al [6], where carrier confinement in one dimension enabled a further reduction in threshold current density.

In 1982, Arakawa and Sakaki theoretically predicted vast improvements to the performance of the conventional quantum well laser with three-dimensional carrier confinement, by virtue of lower threshold, temperature-insensitive operation [7]. While it took more than a decade for such structures to be realized, the development of the first quantum dot (QD) laser in 1994 [8] stimulated extensive efforts to grow, process and characterize such structures, so that the predictions of lower threshold currents and temperature-insensitive operation were soon to come true. In the early 2000s, a group at the University of New Mexico pioneered the fabrication of the so-called "Dots-in-a-Well" (DWELL) structures, leading to record-low threshold current densities of 10 A/cm^2 [9, 10].

In the following year, the group at the University of New Mexico also pioneered the demonstration of the first passively mode-locked quantum dot laser [11]. Since that time, various groups around the world have actively pursued theoretical and experimental research into various aspects of passively mode-locked devices aimed at improving their

performance with innovative growth, processing and device-design ideas on the one hand, and techniques seeking to understand, control and exploit the nonlinear dynamics of the device output using an external control mechanism, on the other. The overarching theme of this dissertation pursues the latter approach.

1.1   Motivation and Dissertation Objectives

Since their first demonstration over a decade ago [11], quantum dot mode-locked lasers (QDMLLs) have generated considerable interest as promising alternatives to quantum well (QW) sources, owing to their demonstrably superior performance characteristics ([5] and [12-17]). Much of this interest in QDMLLs arises from the fact that certain properties unique to QD systems, such as low linewidth enhancement factors and reduced values of unsaturated gain and absorption enable a considerably wider map of operational stability, compared to their bulk and quantum well (QW) counterparts [14-17]. This is important, because most target applications require stable pulse generation over variable operating conditions. For instance, typical operating environments such as data centers require components to be able to tolerate high temperatures accompanied by rapid and considerable heat generation within the system. Consequently, devices need to be engineered to be able to sustain stable output pulses over a range of operating conditions [19-23]. This, in turn, necessitates the need to not only map-out the parameter space of the device over a range of possible operating conditions, but also to gain insight into the functional parameters that are unique to QD systems and modify the properties of the device, compared to QW-based devices. With this objective, although a considerable amount of effort has gone into developing robust analytical and numerical models to

describe passive mode locking in semiconductor lasers (and even modified specifically for QDMLLs), the information available in the literature about the properties unique to QD structures that give them superior performance characteristics relative to QW structures, and how they can be accessed and exploited so as to optimize device performance, is rather scarce. This has led to the associated theoretical and experimental work following two distinct paths, with the former focusing on developing analytical/numerical models of varying degrees of complexity to describe specific physical processes/phenomena, while the latter typically relies on a process of iterative design through extensive testing and characterization.

1.1.1 Theoretical Investigation – Modeling and Simulations

On the theoretical side, as more physical effects and processes are incorporated into the analysis, the model grows in complexity and evolves to encompass a large parameter space. But while this added complexity might enable a better understanding of the underlying device physics and operation, the lack of access to realistic values of many of the associated parameters at various operating conditions severely hinders the process of practical device design/engineering through numerical simulation. Thus, it is highly desirable to have a robust and systematic formalism, whereby a theoretical modeling scheme that is mathematically elegant and computationally tractable, yet able to accurately model/predict key dynamical trends specific to individual devices, can be used as a guide and complement to experiment.

To this end, the primary objective of this dissertation is to develop a systematic approach toward using a Delay Differential Equation (DDE) – based model for passive mode-locking in a semiconductor laser [24-27] as a powerful and versatile tool to simulate

QDMLL device behavior over a range of operating conditions, and to potentially serve as a quantitative map to guide device design. Recent work has shown that variants of this model can be used to study phenomena such as injection locking [28], and a multi-section version of the model has been recently developed to study passive mode-locking [29, 30]. Relative to the other models used to study passive mode locking in semiconductor lasers, the DDE model has a parameter space of just 9 parameters that can be mostly extracted from measurable physical quantities.

In fulfilling this objective, one of the key accomplishments of this dissertation involved the derivation of novel expressions to transform experimentally measured quantities to dimensionless model parameters. This, in turn, led to some novel findings, such as an alternative method of estimating the carrier relaxation ratio of a QDMLL. The standard technique to determine this parameter, which is defined as the ratio of the gain relaxation rate to the absorber relaxation rate, involves measuring gain and absorber recovery times using pump–probe techniques, individually for the semiconductor optical amplifier [31] corresponding to the gain section, and for the saturable absorber [32, 33] corresponding to the absorber section of the two-section laser. The approach discussed in this work provides an analytical expression for the carrier relaxation ratio as a function of static parameters that can be easily measured on a multi-section QD laser test structure over temperature, current density, bias voltage and wavelength. This allows mapping-out the carrier relaxation ratio of the QDMLL over a range of operating conditions, each of which can then be used as an input parameter in the DDE model in order to simulate device performance at that condition, while circumventing the need to perform pump-probe measurements.

5

In using the DDE model in its original form, it was found that the important operational characteristics of the device under study are captured without the need for additional equations or parameters, thereby preserving its relatively simple formalism. For example, numerous analyses are shown to simulate experimental trends accurately, without the need to include additional equations/transitions specific to dot energy levels in the model. Thus, the simulations accurately predict commonly observed experimental phenomena, such as pulse narrowing with increasing absorber bias. In addition, the model and simulations enable novel insight into properties unique to QD systems, such as the lower values of unsaturated gain and absorption compared to the corresponding values for QW devices and key trends in the behavior of the linewidth enhancement factor close to threshold in QD devices. In other words, the properties inherent and unique to QD structures appear to manifest in the measurement-extracted model parameters.

Finally, important trends in the nonlinear dynamics of the device output, such as pulse asymmetry-switching, split-pulsation and stable harmonic mode-locking are found to be not only simulated by the methodology developed in this dissertation, but the model is able to provide invaluable insight into such phenomena, as well as being able to approximately predict the operating conditions under which such effects may be found. This is critical to achieving controllability over device behavior.

1.1.2 Experimental Investigation

The second main objective of this work is to acquire insight into the output nonlinear dynamics of a device through experimentation. Such a methodology complements theoretical analyses in two important ways. First, experimental setups provide the ultimate test bed for the investigation of theoretical predictions. In turn, the dynamical

trends unveiled during experimentation might reveal a certain trend(s), not predicted previously by the model, which could provide a prototypical case for further theoretical analysis.

Secondly, there are certain instances, where the limitations inherent in the model may leave experimental analysis as the sole option to get a sense of the dynamical trends of the device output. A common example of such an instance is when investigating the device behavior well above threshold, where the linewidth enhancement factor seen by the pulse becomes extremely difficult to estimate. In such cases, meticulously conducted experiments provide an indispensable tool to get a sense of the output dynamics. This is also the case when the number of variables/control parameters starts increasing, as in the case of externally-applied optical feedback at elevated temperature (discussed in detail in Chapter 5), and a complete characterization of device output may require information in addition to time-domain pulse width data, such as RF and optical spectral characteristics.

1.2   Brief Overview of Nonlinear Laser Dynamics

Irregular pulse shape and erratic intensity fluctuations have been known to scientists, engineers and other professionals working with all types of lasers, since the very first demonstration of a working laser by Theodore Maiman [34], when it was found that the output of the ruby laser displayed irregular spiking. The first correlations of laser dynamics to nonlinear dynamics and chaos were made by Haken [35, 36], wherein he proposed the isomorphism of the dynamics of certain types of lasers to turbulent fluid flow in atmospheric dynamics [37], so that the mathematical framework used to model the dynamics of lasers could possibly follow from the framework used to study

atmospheric dynamics. However, it was not until the early 1980s, after years of very careful and meticulous analyses of extensive experimental data sets and trends, that laser physicists understood that the pulsating outputs were driven by light-matter interactions within the laser cavity, as opposed to external perturbation due to environmental fluctuations [38]. In the early 1990s, the wide acceptance of the idea that lasers exhibit the same types of bifurcations (qualitative change of dynamical behavior) as oscillating mechanical, chemical and biological systems, coupled with the shift of interest to the nonlinear dynamics of semiconductor lasers (wherein understanding such phenomena becomes especially important, considering the widespread use of such lasers as discussed in the previous section), propelled the field of Nonlinear Laser Dynamics to a hot topic of research worldwide [38-43]. Given the ever-increasing range of applications where such lasers are finding use, extensive theoretical and experimental work has been undertaken by various groups across the world over the last couple of decades, resulting in an improved understanding of the output dynamics of such devices. One common approach is to solve the system of equations describing the system repeatedly while sweeping over one particular parameter, known as the control parameter. A plot of the output dynamics as a function of the control parameter, also referred to as a bifurcation diagram, is then generated, as shown in Fig. 1-1 [27].
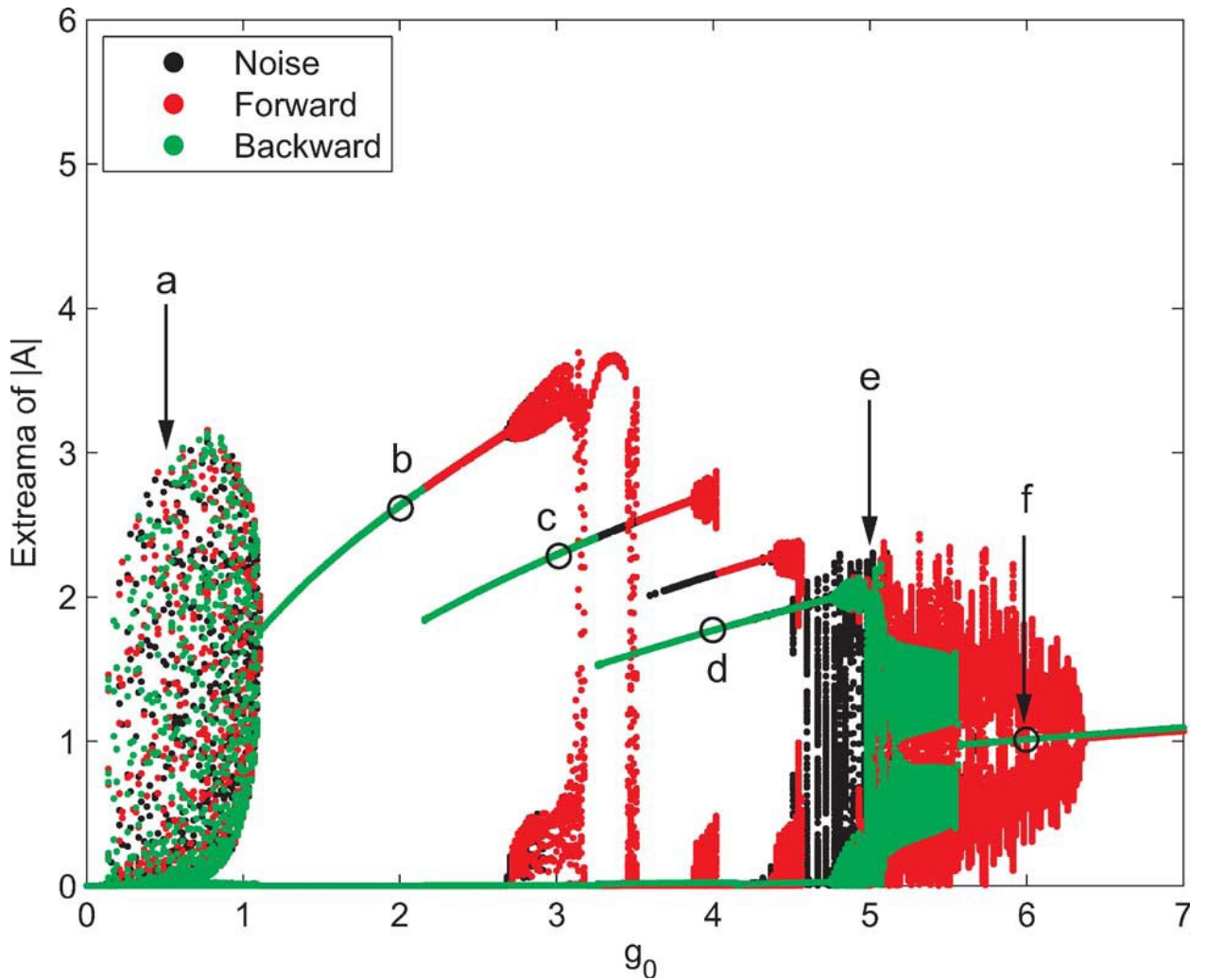
Figure 1-1: *Prototypical bifurcation diagram showing regimes of dynamical behavior at the*

output as a function of the control parameter (in this case, the unsaturated gain parameter). For

a complete analysis, see [27].

Points on the diagram where a qualitative change in the dynamical behavior of the system are seen (marked a-f in Figure 1-1), i.e., bifurcation points, are then individually analyzed in detail. The objective is to be able to predict the dynamical transitions characterizing this behavior, so that unstable regimes of operation may be avoided, and transitions to

stable regimes with desirable characteristics (such as stable harmonic mode-locking) may be controlled and exploited to benefit target applications.

1.3   Key QD Laser Parameters Expected to Impact Output Dynamics

A comparison of experimentally – determined regions of stable mode-locked operation for QW and QD devices of similar structure and composition is shown below in Fig. 1-2 ([15], [44]):
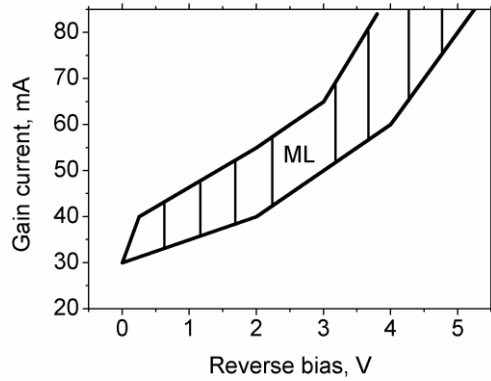
a.)
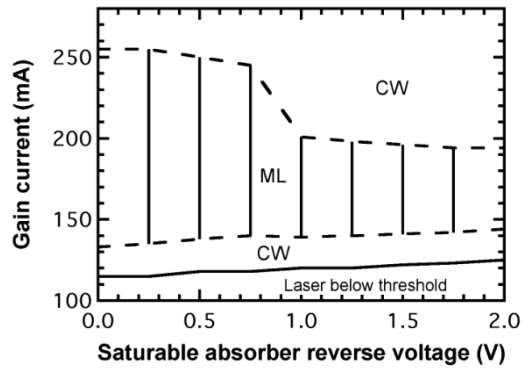
b.)

Figure 1-2: *Mode-Locking Stability Maps for a.) a QW device, and b.) a QD device with similar structure and dimensions.*

Clearly, the QD device shows a much wider region of operational stability, as compared to the QW device. In this section, the important laser parameters responsible for this trend and their expected impact on the output pulse dynamics are briefly reviewed [5].

1.3.1 Threshold Current Density

The three-dimensional spatial confinement of carriers in quantum dots allows only a restricted set of energy levels for occupation. Thus, for a given energy range, the number of carriers required to completely fill the required energy levels is considerably less than for higher dimensional nanostructures, such as bulk or QW structures. In addition, advances in growth and device processing techniques have meant reduced active region volumes enabling tighter carrier confinement, which translates to improved recombination rates.

The combination of the above factors makes it easier to achieve the population inversion required for lasing. This property is also true for mode-locked operation, since in most cases, the onset of mode-locking occurs at lasing threshold. This low threshold translates to lower levels of non-stimulated emission, and hence, to lower levels of spontaneous emission noise.

1.3.2 Temperature Resilience

Due to the delta function-like nature of their density of states, QD lasers exhibit a considerable degree of resilience to temperature-variation, making them attractive for uncooled operation in environments where a wide variation of temperature may be expected. Recent work has demonstrated stable mode-locked operation up to 80℃ in the ground state, and continued pulse generation in the excited state from 80-120℃ ([20-23],

[45]). Furthermore, the mode-locking pulse quality has been shown to improve at elevated temperatures in these works, owing to a combination of faster absorber recovery times and decreasing values of unsaturated gain and absorption, both of which tend to favor mode-locked operation.

Thus, QDMLLs are expected to exhibit stable pulse generation in the ground state up to ~ 80℃, past which a wavelength-switch to the excited state may be expected.

1.3.3 Ultrafast Carrier Dynamics

One of the quintessential requirements for mode-locking action is the interplay between gain and absorber saturation and recovery times. As will be discussed in Chapter 2, the physical mechanism driving passive mode-locking is determined by this interplay, which opens up a brief window of net gain (where the net gain exceeds the total loss in the cavity), enabling pulse generation. The faster the absorber saturation and recovery timescales, the narrower the output pulses. It has been shown that the absorber recovery time decreases rapidly with applied absorber bias [32] and operating temperature [33], although the effect of the former is more drastic.

The ratio of these timescales is quantified by a parameter defined as the carrier relaxation ratio:

$$\Gamma = \left(\tau_{abs} / \tau_{gain} \right)$$

(1-1)

As will be seen in the following chapters, the carrier relaxation ratio of a device is a key parameter required to model the passive mode-locking process.

1.3.4 Lower Values of Unsaturated Gain and Absorption

It was mentioned in §1.3.2, that lower values of unsaturated gain and absorption have been associated with better pulse quality at elevated temperatures. The numerical model used in this dissertation requires these two quantities as input variables, and numerous dynamical studies using the model have performed bifurcation analyses with the unsaturated gain or absorption as a bifurcation parameter, resulting in a range of dynamical regimes associated with the output [24-27]. This is indicative of the fact that both parameters are important in determining the output dynamics of the system.

1.3.5 Gain Saturation

Yet another feature unique to quantum dots is their abrupt gain saturation with carrier density compared to higher dimensional nanostructures, as seen from the modal gain characteristics below [15]:
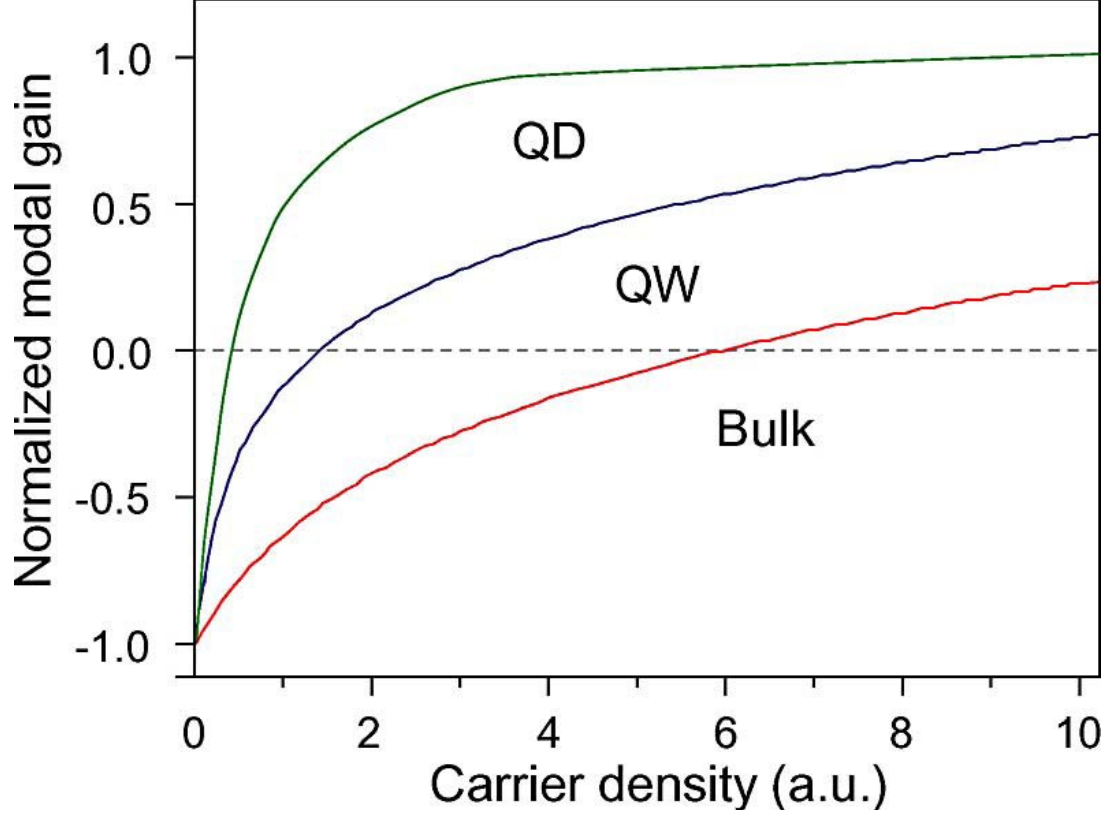
Figure 1-3: *Normalized modal gain versus carrier density, in bulk (red), QW (blue) and QD (green) media [15]. Note the fast rise and rapid saturation of the QD (green) curve.*

The saturation parameter quantifies the gain saturation effect, and is given by the expression:

$$s \equiv \frac{[\partial q_{\mathrm{mod}}(N)/\partial N]\Gamma_q}{[\partial g_{\mathrm{mod}}(N)/\partial N]\Gamma_g}$$

(1-2)

where, $[\partial g_{\mathrm{mod}}(N)/\partial N]$ and $[\partial q_{\mathrm{mod}}(N)/\partial N]$ denote the differential gain and absorption with respect to carrier density, respectively, while Γ_g and Γ_q denote the transverse modal confinement factors in the gain and absorber sections, respectively.

14

The gain saturation effect leads to very low values for the differential gain in the denominator of equation (1-2), indicating that higher values of the saturation parameter favor mode-locking.

1.3.6 Linewidth Enhancement Factor

One of the most important (yet elusive) parameters characterizing nanostructured lasers is the linewidth enhancement factor, also known as the Henry α - factor [46] (in honor of Charles Henry, the scientist who first proposed it) or the amplitude-phase coupling factor. It uses the Kramers –Krönig relation to relate the differential index of refraction to the differential gain of the medium

$$\alpha = -\frac{\partial\{\mathrm{Re}(\chi)\}}{\partial\{\mathrm{Im}(\chi)\}} = -\frac{4\pi}{\lambda}\frac{[\partial n/\partial N]}{[\partial g/\partial N]}$$

(1-3)

This parameter is crucial to semiconductor lasers, and quantifies the asymmetry of the gain spectrum. A high value of this quantity is associated with numerous deleterious effects, including pulse chirp, RF linewidth-broadening and phase noise, pulse-to-pulse timing jitter, etc. Thus, reducing this parameter to as low a value as possible is highly desirable in order to simultaneously improve device performance in numerous aspects [47].

As will be seen in the following chapters, this parameter is also predicted to have a dramatic impact on the temporal pulse dynamics at the output. Considering the ambiguities inherent in physically measuring this parameter, simulations serve as an

excellent tool to analyze the nonlinear dynamics of the output as a function of the α - parameter.

As mentioned earlier in § 1.1, insight into the underlying physical mechanisms driving the dynamical transitions at the output is not only essential to predict and avoid regimes of dynamical instability, but also to achieve controllability over device behavior. To this end, this dissertation aims to serve as a detailed theoretical and experimental investigation into whether and how the various parameters discussed above, critical to the mode-locking performance of a device, can be exploited/manipulated to analyze observed dynamical trends, or to predict a desired output dynamic, particularly in the context of their uniqueness to QD materials.

1.4   Organization of the Dissertation

Chapter 2 starts with a detailed discussion of the numerical model used in this work. After a brief introduction to some of the more advanced treatments being used to model passive mode-locking, the Delay Differential Equation (DDE) formalism originally presented in [24]-[26] is introduced. The chapter then proceeds to derive novel equations to transform data measured experimentally on a given device to dimensionless model parameters, thereby developing a scheme to make the model device-specific.

In Chapter 3, the analytical capabilities of the model are presented. After a brief description of the layer structure and geometry of the device, a novel approach toward estimating the carrier relaxation ratio of a device from gain and loss measurements, specific to its operating conditions is discussed. The approach discussed therein provides a convenient and elegant alternative to conventional pump-probe techniques used to

typically infer this value. The chapter then proceeds to perform parameter sensitivity-analysis studies devoted, respectively, to the linewidth enhancement parameter and to the unsaturated gain and absorption parameters in order to get a sense of how parameters extracted from an actual QDMLL impact the output dynamics. Finally, the chapter demonstrates the powerful capabilities afforded by the model in analyzing dynamical anomalies, such as pulse asymmetry-reversal.

Chapter 4 continues to explore the powerful capabilities of the model, embarking on an investigation of its predictive capabilities. The first part of this chapter studies instabilities in the output dynamics. The newly-developed formalism of the DDE model is used to perform a detailed analysis of what combination of input parameters will lead to device operation in an unstable dynamical regime at the output. The second part of the chapter exploits this capability to predict what combination of inputs will generate a desired output dynamical regime. Based on this approach, a promising scheme to dynamically switch a device from one stable dynamical regime to another is proposed, with the goal of producing higher repetition rates using just electrical biasing controls, as opposed to re-engineering the device.

After a thorough exploration of the model's analytical and predictive capabilities in Chapters 3 and 4, Chapter 5 is devoted to a detailed experimental investigation of the behavior of the RF and optical spectra of the device at elevated temperature, well above threshold, with and without the influence of externally-applied optical feedback. This chapter demonstrates the power of combining theory and experiment as complementary tools to investigate the complicated dynamical trends of a system. Based on previous work and the model's predictions of improved mode-locking performance at elevated

temperatures, combined with the model's predictions of the critical role played by the linewidth enhancement factor in determining output pulse shape and dynamics, this chapter experimentally investigates the dynamical aspects currently unobtainable from the model, namely, the dynamics of the RF and optical spectra. While the former (RF dynamics) is shown to offer qualitative information about the behavior of the linewidth enhancement factor well above threshold, and under what conditions of external control (applied optical feedback) it can be reduced, the latter enables invaluable insight into effects seen in certain devices, such as spectral hole formation.

Finally, concluding remarks and possible future directions are given in Chapter 6.

1.5   References for Chapter 1

[1] Hall, R. N., Fenner, G. E., Kingsley, J. D., Soltys, T. J., & Carlson, R. O. (1962). Coherent light emission from GaAs junctions. *Physical Review Letters*, *9*(9), 366-368.

[2] Dupuis, R. D. (1987). An introduction to the development of the semiconductor laser. *Quantum Electronics, IEEE Journal of*, *23*(6), 651-657.

[3] Alferov, Z. (2000). Double heterostructure lasers: early days and future perspectives. *Selected Topics in Quantum Electronics, IEEE Journal of*, *6*(6), 832-840.

[4] Alferov, Z. I. (2001). Nobel Lecture: The double heterostructure concept and its applications in physics, electronics, and technology. *Reviews of modern physics*, *73*(3), 767-782.

[5] Rafailov, E. U., Cataluna, M. A., & Avrutin, E. A. (2011). *Ultrafast Lasers Based on Quantum Dot Structures: Physics and Devices*. Wiley. com.

 [6] Dupuis, R. D., Dapkus, P. D., Holonyak N., Jr., Rezek, E. A., & Chin, R. (1978) "Room Temperature operation of quantum-well Ga1-xAlxAs-GaAs laser diodes grown by metalorganic chemical vapor deposition," *Applied Physics Letters* 32, 295-297.

[7] Arakawa, Y., & Sakaki, H. (1982). Multidimensional quantum well laser and temperature dependence of its threshold current. *Applied Physics Letters*, *40*, 939.

[8] Kirstaedter, N., Ledentsov, N. N., Grundmann, M., Bimberg, D., Ustinov, V. M., Ruvimov, S. S., ... & Heydenreich, J. (1994). Low threshold, large To injection laser emission from (InGa) As quantum dots. *Electronics Letters*, *30*(17), 1416-1417.

[9] Eliseev, P. G., Li, H., Stintz, A., Liu, G. T., Newell, T. C., Malloy, K. J., & Lester, L. F. (2000). Transition dipole moment of InAs/InGaAs quantum dots from experiments on ultralow-threshold laser diodes. *Applied Physics Letters*, *77*(2), 262-264.

[10] Stintz, A., Liu, G. T., Li, H., Lester, L. F., & Malloy, K. J. (2000). Low-threshold current density 1.3-μm InAs quantum-dot lasers with the dots-in-a-well (DWELL) structure. *Photonics Technology Letters, IEEE*, *12*(6), 591-593.

[11] Huang, X., Stintz, A., Li, H., Lester, L. F., Cheng, J., & Malloy, K. J. (2001). Passive mode-locking in 1.3 μm two-section InAs quantum dot lasers. *Applied Physics Letters*, *78*(19), 2825-2827.

[12] Crowley, M. T., Naderi, N. A., Su, H., Grillot, F., & Lester, L. F. (2012). GaAs-based quantum dot lasers. *Advances in Semiconductor Lasers*, *86*, Chapter 10: Advances in Semiconductor Lasers (New York: Academic).

[13] Crowley, M. T., Kovanis, V., & Lester, L. F. (2012). Breakthroughs in semiconductor Lasers. *Photonics Journal, IEEE*, *4*(2), 565-569.

[14] Rafailov, E. U., Cataluna, M. A., & Sibbett, W. (2007). Mode-locked quantum-dot lasers. *Nature photonics*, *1*(7), 395-401.

[15] Thompson, M. G., Rae, A. R., Xia, M., Penty, R. V., & White, I. H. (2009). InGaAs quantum-dot mode-locked laser diodes. *Selected Topics in Quantum Electronics, IEEE Journal of*, *15*(3), 661-672.

[16] Liu, G., Stintz, A., Li, H., Malloy, K. J., & Lester, L. F. (1999). Extremely low room-temperature threshold current density diode lasers using InAs dots in $In_{0.15} Ga_{0.85}As$ quantum well. *Electronics Letters*, *35*(14), 1163-1165.

[17] Newell, T. C., Bossert, D. J., Stintz, A., Fuchs, B., Malloy, K. J., & Lester, L. F. (1999). Gain and linewidth enhancement factor in InAs quantum-dot laser diodes. *Photonics Technology Letters, IEEE*, *11*(12), 1527-1529.

[18] Lin, C. Y., Xin, Y. C., Li, Y., Chiragh, F. L., & Lester, L. F. (2009). Cavity design and characteristics of monolithic long-wavelength InAs/InP quantum dash passively mode-locked lasers. *Opt. Express*, *17*(22), 19739-19748.

[19] Crowley, M. T., Murrell, D., Patel, N., Breivik, M., Lin, C. Y., Li, Y., ... & Lester, L. F. (2011). Analytical modeling of the temperature performance of monolithic passively mode-locked quantum dot lasers. *Quantum Electronics, IEEE Journal of*, *47*(8), 1059-1068.

[20] Mee, J. K., Crowley, M. T., Patel, N., Murrell, D., Raghunathan, R., Aboketaf, A., ... & Lester, L. F. (2012). A passively mode-locked quantum-dot laser operating over a broad temperature range. *Applied Physics Letters*, *101*(7), 071112-071112.

[21] Mee, J., Crowley, M., Murrell, D., Raghunathan, R., & Lester, L. (2013). Temperature Performance of Monolithic Passively Mode-Locked Quantum Dot Lasers: Experiments and Analytical Modeling.

[22] Mee, J. K., Crowley, M. T., Patel, N., Murrell, D., Raghunathan, R., Aboketaf, A., ... & Lester, L. F. (2012, October). 110° C operation of monolithic quantum dot passively mode-locked lasers. In *Semiconductor Laser Conference (ISLC), 2012 23rd IEEE International* (pp. 68-69). IEEE.

[23] Mee, J. K., Crowley, M. T., Raghunathan, R., Murrell, D., & Lester, L. F. (2013, March). Characteristics of passively mode-locked quantum dot lasers from 20 to 120° C. In *SPIE OPTO* (pp. 86190B-86190B). International Society for Optics and Photonics.

[24] Vladimirov, A. G., Turaev, D., & Kozyreff, G. (2004). Delay differential equations for mode-locked semiconductor lasers. *Optics Letters*, *29*(11), 1221-1223.

[25] Vladimirov, A. G., & Turaev, D. (2005). Model for passive mode locking in semiconductor lasers. *Phys. Rev. A*, *72*(3), 033808.

[26] Vladimirov, A. G., & Turaev, D. (2004). A new model for a mode-locked semiconductor laser. *Radiophysics and quantum electronics*, *47*(10-11), 769-776.

[27] Usechak, N. G., Xin, Y., Lin, C. Y., Lester, L. F., Kane, D. J., & Kovanis, V. (2009). Modeling and direct electric-field measurements of passively mode-locked quantum-dot lasers. *Selected Topics in Quantum Electronics, IEEE Journal of*, *15*(3), 653-660.

[28] Rebrova, N., Huyet, G., Rachinskii, D., & Vladimirov, A. G. (2011). Optically injected mode-locked laser. *Phys. Rev. E*, *83*, 066202.

[29] Rossetti, M., Bardella, P., & Montrosset, I. (2011). Modeling passive mode-locking in quantum dot lasers: A comparison between a finite-difference traveling-wave model

and a delayed differential equation approach. *Quantum Electronics, IEEE Journal of*, *47*(5), 569-576.

[30] Xu, T., Rossetti, M., Bardella, P., & Montrosset, I. (2012). Simulation and analysis of dynamic regimes involving ground and excited state transitions in quantum dot passively mode-locked lasers. *Quantum Electronics, IEEE Journal of*, *48*(9), 1193-1202.

[31] Bakonyi, Z., Su, H., Onishchukov, G., Lester, L. F., Gray, A. L., Newell, T. C., & Tunnermann, A. (2003). High-gain quantum-dot semiconductor optical amplifier for 1300 nm. *Quantum Electronics, IEEE Journal of*, *39*(11), 1409-1414.

[32] Malins, D. B., Gomez-Iglesias, A., White, S. J., Sibbett, W., Miller, A., & Rafailov, E. U. (2006). Ultrafast electroabsorption dynamics in an InAs quantum dot saturable absorber at 1.3μm *Applied Physics Letters*, *89*(17), 171111-171111.

[33] Cataluna, M. A., Malins, D. B., Gomez-Iglesias, A., Sibbett, W., Miller, A., & Rafailov, E. U. (2010). Temperature dependence of electroabsorption dynamics in an InAs quantum-dot saturable absorber at 1.3 μm and its impact on mode-locked quantum-dot lasers. *Applied Physics Letters*, *97*(12), 121110-121110.

[34] Maiman, T. H. (1960). Stimulated optical radiation in ruby.

[35] Haken, H. (1975). Analogy between higher instabilities in fluids and lasers. *Physics Letters A*, *53*(1), 77-78.

[36] Haken, H. (1983). Synergetics. an introduction. *Springer Series in Synergetics, Berlin: Springer, 1983, 3rd ed.*, *1*.

[37] Lorenz, E. N. (1963). Deterministic nonperiodic flow. *Journal of the atmospheric sciences*, *20*(2), 130-141.

[38] Erneux, T., & Glorieux, P. (2010). *Laser dynamics*. Cambridge University Press.

[39] Erneux, T. (2009). *Applied delay differential equations* (Vol. 3). Springer.

[40] Weiss, C. O. & Vilaseca, R. (1991), *Dynamics of lasers*, VCH, Weinheim, Germany.

[41] Newell, A. C., & Moloney, J. V. (1992). *Nonlinear optics* (pp. 0-201). Redwood City: Addison-Wesley.

[42] Khanin, Y. I. (1995). *Principles of laser dynamics*. North Holland.

[43] Khanin, I. I., & Khanin, Y. I. (2006). *Fundamentals of laser dynamics*. Cambridge Int Science Publishing.

[44] Palaski, J., & Lau, K. Y. (1991). Parameter ranges for ultrahigh frequency mode locking of semiconductor lasers. *Applied physics letters*, *59*(1), 7-9.

[45] Cataluna, M. A., Rafailov, E. U., McRobbie, A. D., Sibbett, W., Livshits, D. A., & Kovsh, A. R. (2006). Stable mode-locked operation up to 80 C from an InGaAs quantum-dot laser. *Photonics Technology Letters, IEEE*, *18*(14), 1500-1502.

[46] Henry, C. (1982). Theory of the linewidth of semiconductor lasers. *Quantum Electronics, IEEE Journal of*, *18*(2), 259-264.

[47] Osinski, M., & Buus, J. (1987). Linewidth broadening factor in semiconductor lasers--An overview. *Quantum Electronics, IEEE Journal of*, *23*(1), 9-29.

Chapter 2

A Novel Delay Differential Equation (DDE) – Based Formalism

Robust modeling techniques can provide a powerful and indispensable tool to design and engineer QDMLLs to meet the ever-more stringent performance constraints of next-generation devices. While a considerable amount of effort has gone into developing detailed analytical and numerical models to describe mode-locking in semiconductor lasers (and even modified specifically for QDMLLs) [1]-[6], the information available in the literature about device parameter values unique to QD-based structures and how they can be accessed and exploited to optimize device performance is very limited. This has led to the associated theoretical and experimental work following two distinct paths, with the former focusing on developing analytical/numerical models of varying degrees of complexity to describe specific physical processes/phenomena constituting the mode-locking process, while the latter typically relies on a process of iterative design through extensive testing and characterization. On the theoretical side, as more physical effects and processes are incorporated into the analysis, the model grows in complexity and evolves to encompass a large parameter space. Although this added complexity should enable a better understanding of the underlying device physics and operation, the lack of parameters that can be easily measured, coupled with the number of required parameters often limits the practical utility of more rigorous models.

To this end, one of the primary objectives of this dissertation is to develop a powerful numerical modeling capability to simulate actual passively mode-locked QD lasers using parameters measured on the device. As will be seen in the following two chapters, the

technique needs to be versatile in order to be used across devices and over a range of operating conditions as an analytical tool, whereby observed phenomena can be interpreted using the model, but also as a predictive guideline for the design and operation of devices.

At the same time, the Delay Differential Equation-based formalism of the model ensures a robust mathematical framework at the core, lending itself extremely well to the study of the rich nonlinear laser dynamics inherent in the output of such devices. Complex mathematical ideas, such as bifurcation dynamics, can be used to predict and analyze abrupt and often unsolicited transitions in the device output [7]. In addition, the formalism can be extended in a natural way to include complex effects such as optoelectronic and optical feedback ([8], [9], [10]) and optical injection [11].

Consequently, the subject of this chapter is to develop a systematic method to model passive mode-locking [12]-[14] that enables device-specific simulation and analysis, while preserving the underlying mathematical framework. At the same time, reducing the parameter-space of the model by constraining the majority of the parameters to values measured on the device under study is also a priority.

The chapter is organized as follows. Section 2.1 starts with a brief overview of the fundamentals underlying the passive mode-locking process in section 2.1.1. A recently-developed, comprehensive model to describe passive mode-locking in QD lasers based on the Traveling Wave formalism is then discussed in section 2.1.2, followed by a simplified version in section 2.1.3. Section 2.2 then discusses the derivation of the Delay Differential Equation model from the simplified Traveling Wave model in detail. Next, in section 2.3, the extension of the model to a novel formalism to simulate QDMLLs with

parameters measured on the device is presented. Concluding remarks are presented in section 2.4.

2.1   Introduction

2.1.1   Fundamentals of Passive Mode-Locking

Figure 2-1 [15] shows the essential components required for a laser cavity to generate passively mode-locked pulses.
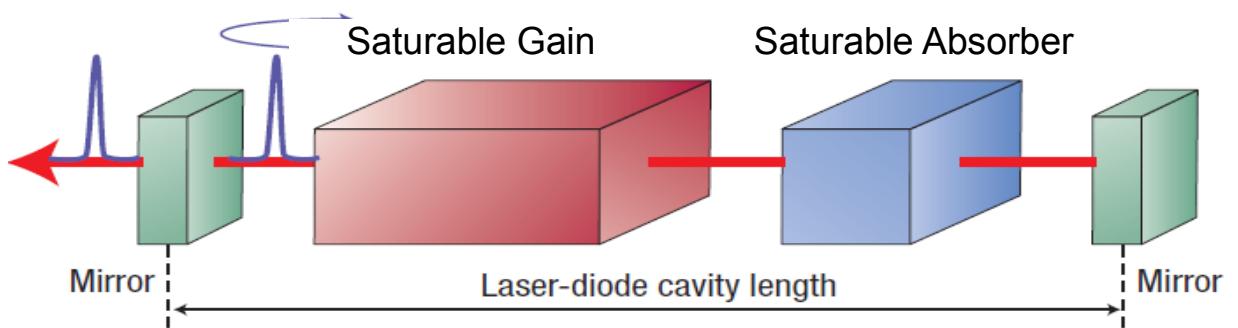
Figure 2-1: *Schematic of passive mode-locking in a 2-section laser diode [15] .*

The saturable absorber possesses the quintessential property of an intensity-dependent absorption profile, such that its absorption decreases with incident optical intensity. This feature acts as a discriminator between pulsed and continuous wave (cw) operation of the device, so that passive mode-locking necessarily requires an intracavity saturable absorber element. Unlike other methods of producing mode-locked pulses, namely, active and hybrid mode-locking, passive mode-locking does not require an external reference source for pulse formation, and is a self-starting, self-sustaining process as described next.

Laser emission is built-up from the spontaneous fluctuations of light intensity within the cavity, so that the laser modes begin to oscillate in noisy bursts, with uncorrelated phases.

If one of these bursts has sufficient fluence to match the saturation fluence of the saturable absorber medium, it will bleach the absorption. This means that around the peak of the burst, the strong intensity causes the loss to decrease sharply, whereas the wings of the burst are not quite as energetic, and are attenuated.

At steady state, the leading edge of a pulse bleaches the absorption such that the absorber saturates faster than the gain, thereby opening a brief window of time during which net gain exceeds total loss (often referred to in the literature as the "net gain window"). However, because the absorber also recovers to its initial state of high loss faster than the gain recovers, the trailing edge of the pulse is attenuated. It is during this brief "net gain window" that pulses are sustained, with peak intensity attained when the gain exceeds the total loss by the maximum amount, as shown in Fig. 2-2.
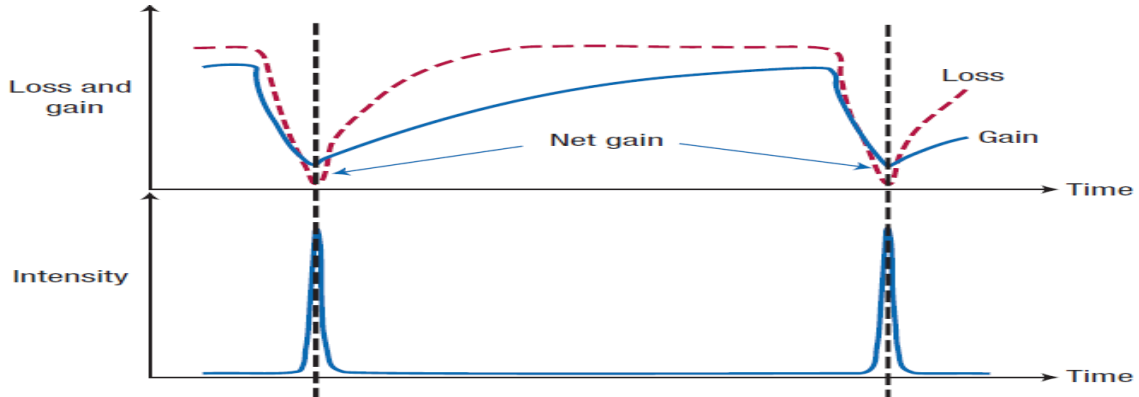
Figure 2-2: Schematic showing pulse formation determined by the dynamics of net gain and total loss [15].

Outside each net gain window, the total loss exceeds the gain, so that the intensity goes to zero between pulses. At steady state, this interplay between gain and absorber dynamics

is self-sustaining and periodic, so that pulse generation follows this same behavior [15]-[17].

2.1.2 The Traveling Wave Model

Several numerical models of varying degrees of complexity have been developed to describe passive mode-locking in semiconductor lasers using the traveling wave formalism. One of the most sophisticated and rigorous schemes to model passive mode-locking in quantum dot lasers was developed in recent works by Rosetti et al ([1]-[4], [6]), wherein, a range of complex phenomena, such as the time-varying QD optical susceptibility, the inhomogeneous broadening of the density of states of the entire QD ensemble, as well as the homogeneous linewidth associated with each QD interband transition were taken into account. The Finite Difference Traveling Wave (FDTW) model was used to express the spatiotemporal field evolution individually in the ground state (GS) and the first excited state (ES$_1$) using the following system of coupled Partial Differential Equations (PDEs) [6]:

$$\frac{1}{v_g}\frac{\partial E_{GS}^{\pm}}{\partial t} \pm \frac{\partial E_{GS}^{\pm}}{\partial z} = \Gamma_{xy} g_{GS}(t,z)\left(\gamma e^{-\gamma t} \otimes E_{GS}^{\pm}(t,z)\right) + i\beta\Gamma_{xy} g_{ES_1}(t,z)E_{GS}^{\pm}(t,z) - \frac{\alpha_i}{2}E_{GS}^{\pm}(t,z)$$

$$(2\text{-}1a)$$

$$\frac{1}{v_g}\frac{\partial E_{ES_1}^{\pm}}{\partial t} \pm \frac{\partial E_{ES_1}^{\pm}}{\partial z} = \Gamma_{xy} g_{ES_1}(t,z)\left(\gamma e^{-\gamma t} \otimes E_{ES_1}^{\pm}(t,z)\right) - i\beta\Gamma_{xy} g_{GS}(t,z)E_{ES_1}^{\pm}(t,z) - \frac{\alpha_i}{2}E_{ES_1}^{\pm}(t,z)$$

$$(2\text{-}1b)$$

where, $g_k(t,z)$ represents the QD material gain at the wavelength resonant at $k = GS, ES_1$, Γ_{xy} is the confinement factor within the QD layers and α_i are the intrinsic waveguide losses. The convolution operation performed in parentheses in the

first term on the right hand side of each equation above describes the field modified

by a Lorentzian filter of width γ in order to model the finite gain spectral bandwidth,

which is limited by the QD inhomogeneous gain broadening.

In the second term on the RHS of equations (2-1a) and (2-1b), $\beta\Gamma_{xy}g_{GS}(t,z)$ and

$\beta\Gamma_{xy}g_{ES_1}(t,z)$ represent instant changes in the real part of the propagation constant

induced by the QD ES at the GS wavelength and vice-versa, where,

$$\beta \cong \gamma\frac{\omega_{ES_1}-\omega_{GS}}{\gamma^2+\left(\omega_{ES_1}-\omega_{GS}\right)^2}$$

(2-2)

The boundary conditions for the forward and backward-propagating waves are given by:

$$E_k^+(t,0)=\sqrt{R_1}\,E_k^-(t,0)$$

(2-3a)

$$E_k^-(t,L^{FP})=\sqrt{R_2}\,E_k^+(t,L^{FP}),k=GS,ES_1$$

(2-3b)

where L^{FP} is the total Fabry-Perot cavity length, while R_1 and R_2 represent power

reflectivities at the end facets.

Further, the gain/absorber dynamics in the corresponding section of the cavity (gain or

saturable absorber) are described by a set of 3 coupled rate equations to represent level

transitions within the dot (GS, ES$_1$, ES$_2$), plus 2 additional equations to model the carrier

dynamics in the quantum well and barrier states, respectively. The carrier dynamics

specific to each section is carefully modeled by the authors by taking into account current

injection into the gain section and reverse bias voltage-induced effects (such as

thermionic escape or tunneling dynamics, depending upon the applied voltage strength). The rate equations in this case describe the time-evolution of the occupation probability of the kth QD state in the cavity section z:

$$\frac{d\rho_k(t,z)}{dt} = R_k^{in}(t,z) - R_k^{out}(t,z) - R_k^{s}(t,z) - R_k^{stim}(t,z)$$

$$(2\text{-}4)$$

In the above equation, $R_k^{in}(t,z)$ and $R_k^{out}(t,z)$ represent respectively the in and out-scattering rates, while $R_k^{s}(t,z)$ represents the radiative and non-radiative recombination rate.

While a detailed description of the three terms listed above can be found in [4], the last term on the RHS of (2-4) represents the stimulated emission rate given by:

$$R_k^{stim}(t,z) = \frac{2\Gamma_{xy}g_k(t,z)}{WN_D D_k \hbar \omega_k} \sum_{\pm} \Re e\left[\left(E_k^{\pm}(t,z)\right)^* \left(\gamma e^{-\gamma t} \otimes E_k^{\pm}(t,z)\right)\right]$$

$$(2\text{-}5)$$

where $g_k(z,t) = g_{0k}(2\rho_k(t,z) - 1)$, W is the ridge width, N_D is the QD surface density and D_k is the degeneracy of the kth QD state. Finally, g_{0k} is the material gain coefficient for the kth QD state.

As mentioned before in this section, the model discussed above is one of the most rigorous and accurate schemes available in the published literature. However, from the standpoint of using the model as a robust theoretical framework for the design and performance analysis of real devices, certain challenges arise that limit its practical utility.

Firstly, the standard approach to solving the system of equations (2-1) – (2-5) involves the use of Finite Difference Time Domain (FDTD) techniques, whereby, the spatio-temporal field can be solved for in the longitudinal direction using a two-dimensional grid. Each step of the simulation involves solving the system of equations above over a spatial grid with a step size Δz, coupled to a temporal grid with a step size Δt, using the expression $\Delta z = v_g \Delta t$.

Typical simulation time steps are chosen to be on the order of a few femtoseconds, in order to enhance resolution and improve accuracy. However, the coupled spatio-temporal formalism also means that the finer the resolution of the two-dimensional grid, the more computationally expensive the simulation.

Second, a glance at the system of equations, and in particular, the fact that each term in the rate equation (2-5) is itself described by an equation, gives a sense of the vastness of the parameter space involved. A good example of this is seen in the table of simulation parameters presented in [4], where the combination of requisite material and device parameters amounts to a total of 23.

Many of these parameters, such as interband relaxation and recombination times, require dedicated experimental arrangements (such as time-resolved pump-probe spectroscopy setups) for their individual measurement, which often translates into a tedious setup-and-measurement process for a single model parameter.

In other cases, the model parameter could be a purely theoretical construct, unattainable by measurement (for instance, the Pauli blocking factor, invoked in some models e.g. [5]). In such cases, the value used is often a standard value quoted in the literature.

Further, the specific set of parameter values will likely differ widely from one device to another, which makes modeling a range of different devices with different operating parameters, a tedious and cumbersome process.

For all these reasons, it is highly desirable to have a model with a tractable parameter space involving parameters that can be easily extracted on any given device, across a wide range of different operating conditions.

2.1.3   The Simplified Traveling Wave Model

A series of simplifying assumptions can dramatically reduce the complexity of the system of equations (2-1) – (2-5). Any concomitant reduction in accuracy is negligible for most purposes, as will be seen in numerous instances in the following chapters.

The first major simplifying assumption is the abstraction of a standard two-section linear semiconductor laser cavity to a ring cavity, as shown in Figure 2-3 [13].

In the ring cavity diagram in Figure 2-3, coordinate z is measured along the cavity axis. Interval $z_2 < z < z_3 (z_3 < z < z_4)$ corresponds to the absorbing (amplifying) section. A spectral filtering (bandwidth limiting) element is placed between $z = z_5$ and $z = z_1 + L$, where L is the total cavity length. Intervals $z_1 < z < z_2$ and $z_4 < z < z_5$ represent a passive medium.
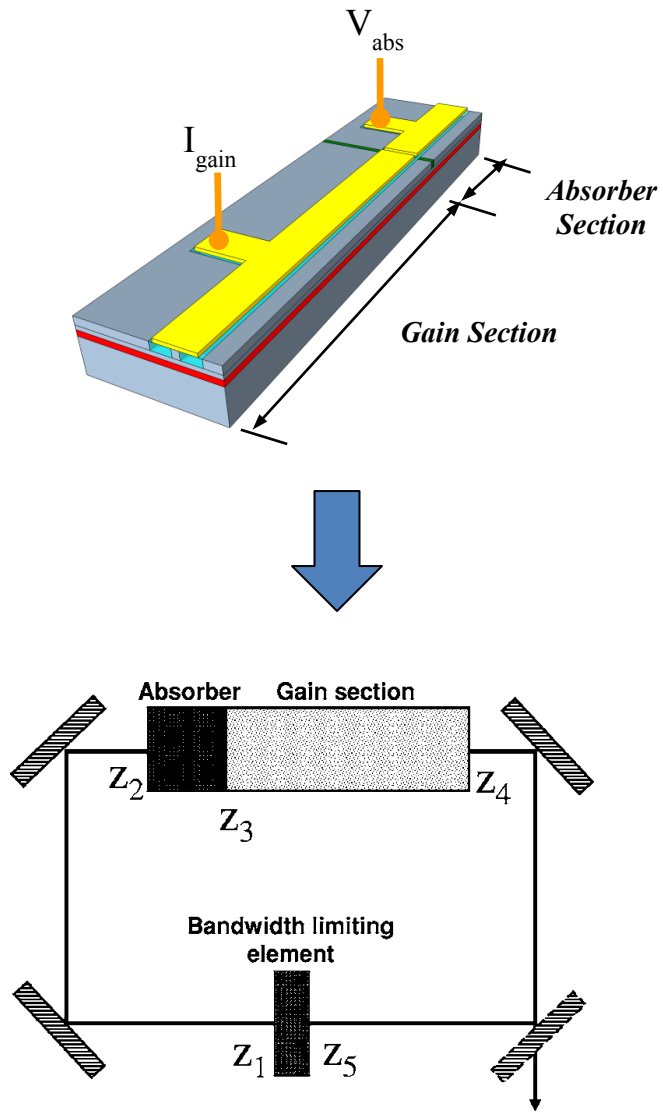
Figure 2-3: Abstraction of a two-section linear cavity to a ring cavity [13].

Next, unidirectional field propagation is assumed so that only one of the two counter-propagating waves needs to be considered.

The combination of the above two assumptions, namely, abstraction to a ring cavity geometry with unidirectional wave propagation, enables use of the lumped-element

approach, whereby the interaction of the intracavity field with the laser medium can be treated as a sequence of independent stages. Thus, even though the propagating pulse experiences the effects of distributed gain, loss and material dispersion simultaneously, the formalism above allows segregating the carrier-field interaction as a traveling wave interacting with a lumped gain element, a lumped absorber and a spectral bandwidth filter (associated with a finite gain bandwidth) in sequence.

The third major simplifying assumption is to discard the intricacies associated with modeling the device using the barrier-well-dot hierarchical formalism used in [4] and [5], and replace the considerably complex detailed-balancing scheme buried in the rate equation (2-4) (where it may be recalled that each individual term on the RHS is itself described by an equation comprised of a set of parameters) with a single and surprisingly simple equation that assumes a linear dependence on the medium carrier densities. Thus, two equations describing the temporal evolution of carrier densities in the gain and absorber sections replace the set of rate equations associated with (2-4).

Finally, only ground state lasing is considered. Under this set of simplifying assumptions, the following generic (and considerably simpler) traveling wave model is employed:

$$\frac{\partial E(t,z)}{\partial z} + \frac{1}{v}\frac{\partial E(t,z)}{\partial t} = \frac{g_k \Gamma_k}{2}(1 - i\alpha_k)\left[N_k(t,z) - N_k^{tr}\right]E(t,z)$$

(2-6)

$$\frac{\partial N_k(t,z)}{\partial t} = J_k - \frac{N_k(t,z)}{\tau_k} - vg_k\Gamma_k\left[N_k(t,z) - N_k^{tr}\right]|E(t,z)|^2$$

(2-7)

In equations (2-6) and (2-7) above, the subscript $k = g(k = q)$ corresponds to the gain (absorber) section. $E(t,z)$ describes the optical field in the two sections. The variables

34

$N_{g,q}(t,z)$ denote carrier densities in the gain/absorber sections, while the variables $N_{g,q}^{tr}$ are the carrier densities at transparency in the corresponding section. The parameter v is the light group velocity, assumed constant and equal in both sections. The parameters $\alpha_{g,q}, g_{g,q}, \Gamma_{g,q}$ and $\gamma_{g,q}$ are, respectively, the linewidth enhancement factors, differential gains, transverse modal fill factors and carrier density relaxation rates in the gain and absorber sections. The parameters J_g and $J_q (=0)$ denote the injection current densities in the gain and absorber sections, respectively.

Since the passive sections do not contain gain or absorber material, and consequently, no carrier densities, the evolution of the electric field in these sections may be written as:

$$\frac{\partial E(t,z)}{\partial z} + \frac{1}{v}\frac{\partial E(t,z)}{\partial t} = 0$$

(2-8)

Material gain dispersion (including dispersive effects due to artificial elements such as distributed Bragg reflectors), are incorporated through the lumped spectral filtering section.

If $\hat{f}(\omega)$ represents the frequency domain spectral filtering function, the transformation of the electric field envelope by this section may be expressed as:

$$\hat{E}(\omega, z_1 + L) = \hat{f}(\omega)\hat{E}(\omega, z_5)$$

(2-9)

where, $\hat{E}(\omega, z_5)$ and $\hat{E}(\omega, z_1 + L)$ are the Fourier transforms of $E(t, z_5)$ and $E(t, z_1 + L)$, respectively. Material gain dispersion, including dispersive effects due to other cavity elements such as distributed Bragg reflectors, are incorporated through the lumped

spectral filtering section. With the mathematical framework now in place for the lumped-element treatment of carrier-field interactions within the cavity, we are now ready to make the transition from the Traveling Wave formalism to an equivalent Delay Differential Equation (DDE) formalism. In the following section, we follow the treatment in [13] to summarize a series of mathematical definitions and transformations and derive the DDE model from equations (2-6) to (2-9). While the key steps outlining the transformation are shown here, detailed derivations are given in Appendix A.

2.2   The Delay Differential Equation (DDE) Model

Equations (2-6) and (2-7) may be re-cast in terms of the normalized coordinates $(t,z) \rightarrow (\tau,\zeta)$, where $\tau = \gamma_q (t - (z/v))$

$$(2\text{-}10a)$$

$$\zeta = (z\gamma_q / v),$$

$$(2\text{-}10b)$$

where the normalizing factor is the absorber recovery time $\tau_q = (1/\gamma_q)$. The absorber recovery time determines the pulse width, so that the advantage of making this parameter the characteristic timescale is to normalize all quantities in the equation to a critical timescale in the problem, which ensures that there is sufficient temporal resolution to obtain complete information for all constituent processes. With this coordinate transformation, equations (2-6) and (2-7) may be expressed as:

$$\frac{\partial E(\tau,\zeta)}{\partial \zeta} = \frac{vg_r\Gamma_r}{\gamma_q}\left(\frac{1-i\alpha_r}{2}\right)\left[N_r(\tau,\zeta) - N_r^{tr}\right]E(\tau,\zeta)$$

$$(2\text{-}11)$$

$$\frac{\partial N_g(\tau,\zeta)}{\partial \tau} = \left(\frac{J_g}{\gamma_q}\right) - \left(\frac{\gamma_g}{\gamma_q}\right)N_g(\tau,\zeta) - \frac{vg_g\Gamma_g}{\gamma_q}\left[N_g(\tau,\zeta) - N_g^{tr}\right]E(\tau,\zeta)^2$$

(2-12)

$$\frac{\partial N_q(\tau,\zeta)}{\partial \tau} = \left(\frac{J_q}{\gamma_q}\right) - N_q(\tau,\zeta) - \frac{vg_q\Gamma_q}{\gamma_q}\left[N_q(\tau,\zeta) - N_q^{tr}\right]E(\tau,\zeta)^2$$

(2-13)

The next step is to transform equations (2-11) to (2-13) to a non-dimensional form. In order to do this, the following transformation relations are defined:

$$A(\tau,\zeta) = E(\tau,\zeta)\sqrt{\left(vg_g\Gamma_g/\gamma_q\right)}$$

(2-14a)

$$n_{g,q}(\tau,\zeta) = \left(vg_{g,q}\Gamma_{g,q}/\gamma_q\right)\left[N_{g,q}(\tau,\zeta) - N_{g,q}^{tr}\right]$$

(2-14b)

$$j_g = \left(vg_g\Gamma_g\left(J_g - \gamma_g N_g^{tr}\right)/\gamma_q^2\right)$$

(2-14c)

$$j_q = \left(vg_g\Gamma_g N_q^{tr}/\gamma_q\right)$$

(2-14d)

$$\Gamma = \left(\gamma_g/\gamma_q\right)$$

(2-14e)

$$s = \left(g_q\Gamma_q/g_g\Gamma_g\right)$$

(2-14f)

Multiplying both sides of equation (2-11) by $\sqrt{vg_g\Gamma_g/\gamma_q}$, we have:

$$\sqrt{\left(\frac{vg_g\Gamma_g}{\gamma_q}\right)}\frac{\partial E(\tau,\zeta)}{\partial\zeta}=\left(\frac{1-i\alpha_r}{2}\right)\left(\frac{vg_r\Gamma_r}{\gamma_q}\right)\left[N_r(\tau,\zeta)-N_r^{tr}\right]\left\{\sqrt{\left(\frac{vg_g\Gamma_g}{\gamma_q}\right)}E(\tau,\zeta)\right\}$$

from which we obtain,

$$\frac{\partial A(\tau,\zeta)}{\partial\zeta}=\left(\frac{1-i\alpha_{g,q}}{2}\right)n_{g,q}(\tau,\zeta)A(\tau,\zeta)$$

- (using the definitions in (2-14a) and (2-14b))

(2-15)

Next, multiplying both sides of (2-12) by $(vg_g\Gamma_g/\gamma_q)$, we have:

$$\left(\frac{vg_g\Gamma_g}{\gamma_q}\right)\frac{\partial N_g(\tau,\zeta)}{\partial\tau}=\left(\frac{vg_g\Gamma_g}{\gamma_q}\right)\left(\frac{J_g}{\gamma_q}\right)-\left(\frac{vg_g\Gamma_g}{\gamma_q}\right)\left(\frac{\gamma_g}{\gamma_q}\right)N_g(\tau,\zeta)-\left(\frac{vg_g\Gamma_g}{\gamma_q}\right)\left[N_g(\tau,\zeta)-N_g^{tr}\right]\left\{\left(\frac{vg_g\Gamma_g}{\gamma_q}\right)\left|E(\tau,\zeta)\right|^2\right\}$$

which, after some manipulation, can be expressed in the form:

$$\frac{\partial n_g(\tau,\zeta)}{\partial\tau}=j_g-\Gamma n_g(\tau,\zeta)-n_g(\tau,\zeta)\left|A(\tau,\zeta)\right|^2$$

(2-16)

Similarly, equation (2-13) can be manipulated into the analogous form:

$$\frac{\partial n_q(\tau,\zeta)}{\partial\tau}=-j_q-n_q(\tau,\zeta)-sn_q(\tau,\zeta)\left|A(\tau,\zeta)\right|^2$$

(2-17)

Also, the passive sections have no gain or absorber medium, so that the evolution of the optical field in these sections may be expressed as:

$$\frac{\partial A(\tau, \zeta)}{\partial \zeta} = 0$$

(2-18)

From (2-18) and the ring cavity schematic in Figure 2-3, we find that:

$$A(\tau, \zeta_2) = A(\tau, \zeta_1), \text{ and,}$$

$$A(\tau, \zeta_5) = A(\tau, \zeta_4)$$

where, again, $\zeta_k = (z_k \gamma_q / v)$.

(2-19)

Next, the evolution of the optical field in the gain and absorber sections may be obtained

by integrating equation (2-15) section-wise as follows:

- Gain section $(\zeta_3 < \zeta < \zeta_4)$:

$$\frac{\partial A(\tau, \zeta)}{\partial \zeta} = \left(\frac{1 - i\alpha_g}{2} \right) n_g(\tau, \zeta) A(\tau, \zeta)$$

Rearranging and integrating the resulting expression over the limits of ζ, we get:

$$A(\tau, \zeta_4) = e^{\frac{1}{2}(1 - i\alpha_g)G(\tau)} A(\tau, \zeta_3)$$

(2-20)

Next, equation (2-16) needs to be integrated over ζ to find the evolution equations of the

saturable gain:

$$\partial_\tau \int_{\zeta_3}^{\zeta_4} dn_g(\tau, \zeta) = \int_{\zeta_3}^{\zeta_4} j_g d\zeta - \Gamma \int_{\zeta_3}^{\zeta_4} n_g(\tau, \zeta) d\zeta - \int_{\zeta_3}^{\zeta_4} n_g(\tau, \zeta) |A(\tau, \zeta)|^2 d\zeta$$

$$\Rightarrow \partial_\tau G(\tau) = g_0 - \Gamma G(\tau) - \int_{\zeta_3}^{\zeta_4} n_g(\tau, \zeta) |A(\tau, \zeta)|^2 d\zeta$$

(2-21)

- Absorber section $(\zeta_2 < \zeta < \zeta_3)$:

$$\frac{\partial A(\tau,\zeta)}{\partial \zeta} = \left(\frac{1-i\alpha_q}{2}\right) n_q(\tau,\zeta) A(\tau,\zeta)$$

$$\Rightarrow A(\tau,\zeta_3) = e^{-\frac{1}{2}(1-i\alpha_q)Q(\tau)} A(\tau,\zeta_2)$$

(2-22)

Again, integrating equation (2-17) over ζ to find the time evolution equation for the saturable absorption, we get:

$$\partial_\tau \int_{\zeta_2}^{\zeta_3} dn_q(\tau,\zeta) = \int_{\zeta_2}^{\zeta_3} j_q d\zeta - \int_{\zeta_2}^{\zeta_3} n_q(\tau,\zeta) d\zeta - \int_{\zeta_2}^{\zeta_3} n_q(\tau,\zeta) |A(\tau,\zeta)|^2 d\zeta$$

$$\Rightarrow \partial_\tau Q(\tau) = q_0 - Q(\tau) - s \int_{\zeta_2}^{\zeta_3} n_q(\tau,\zeta) |A(\tau,\zeta)|^2 d\zeta$$

(2-23)

The integrals on the RHS of equations (2-21) and (2-23) may be evaluated to yield:

$$\partial_\tau G(\tau) = g_0 - \Gamma G(\tau) - |A(\tau,\zeta_4)|^2 + |A(\tau,\zeta_3)|^2$$

(2-24)

$$\partial_\tau Q(\tau) = q_0 - Q(\tau) + s |A(\tau,\zeta_3)|^2 - s |A(\tau,\zeta_2)|^2$$

(2-25)

Now, equation (2-9) for the spectral filtering element may be expressed in time as:

$$A(\tau,\zeta_1 + T) = \int_{-\infty}^{\tau} f(\tau - \theta) A(\tau,\zeta_5) d\theta$$

(2-26)

40

where, $T = \left(\gamma_q L / v \right)$ is the normalized cold cavity round trip time.

Substituting equations (2-20) and (2-22) into (2-26) and re-expressing the field transformation condition in the form $A(\tau, \zeta + T) = A(\tau + T, \zeta)$, we have:

$$A(\tau + T) = \int_{-\infty}^{\tau} f(\tau - \theta) R(\theta) A(\theta) d\theta$$

(2-27)

$$\text{with, } R(\tau) = \sqrt{\kappa} e^{\left[\left\{ (1 - i\alpha_g) \frac{G(\tau)}{2} \right\} - \left\{ (1 - i\alpha_q) \frac{Q(\tau)}{2} \right\} \right]}.$$

(2-28)

Using a Lorentzian line shape function for the spectral filtering element,

$$f(\tau) = \gamma \exp\left[(-\gamma + i\Omega)\tau \right]$$

(2-29)

Substituting (2-28) and (2-29) into (2-27), we get:

$$A(\tau + T) = \int_{-\infty}^{\tau} \gamma \exp\left[(-\gamma + i\Omega)(\tau - \theta) \right] \sqrt{\kappa} \exp\left[\frac{1}{2} \left\{ (1 - i\alpha_g) G(\theta) - (1 - i\alpha_q) Q(\theta) \right\} \right] A(\theta) d\theta$$

(2-30)

Finally, differentiating equation (2-30) w.r.t dimensionless time τ, the two-dimensional (spatio-temporal) system of PDEs is simplified to a one-dimensional (temporal) system of DDEs [13, 14]:

$$\frac{dA(\tau)}{d\tau} = \gamma \sqrt{\kappa} e^{\left\{ \frac{1}{2}(1 - i\alpha_g) G(\tau - T) - \frac{1}{2}(1 - i\alpha_q) Q(\tau - T) \right\}} A(\tau - T) - \gamma A(\tau)$$

(2-31)

$$\frac{dG(\tau)}{d\tau} = g_0 - \Gamma G(\tau) - e^{-Q(\tau)}\left(e^{G(\tau)} - 1\right)|A(\tau)|^2$$

<div align="right">(2-32)</div>

$$\frac{dQ(\tau)}{d\tau} = q_0 - Q(\tau) - s\left(1 - e^{-Q(\tau)}\right)|A(\tau)|^2$$

<div align="right">(2-33)</div>

In the following section, a novel and powerful formalism to transform the system of equations derived above in [13] and make them device-specific for a given two-section passively mode-locked quantum dot laser with parameters measured on the device, is presented.

The next two chapters then proceed to show instances of how this novel formalism can dramatically enhance the model's analytical and predictive capabilities, providing a simple and elegant, yet remarkably powerful tool to model real devices that circumvents many of the issues inherent to more sophisticated models, outlined earlier in this chapter.

2.3 A Novel Formalism for a DDE Model Seeded with Device-Specific Measurables [18]

A recent experiment performed by our group [19] made use of the Segmented Contact Method [20, 21] to obtain modal gain and total loss spectra as a function of current density, over absorber bias voltage and temperature for the QD material comprising the device. These curves were used to extract the modal gain $\left(g_{\text{mod}}\right)$ and unsaturated absorption $\left(a_0\right)$ as a function of current density at each bias condition.

Now, from equation (2) in [19], we have the following threshold condition for lasing:

$$\left(g_{\mathrm{mod}}(J)-\alpha_i\right)L_g-\left(a_0+\alpha_i\right)L_a=\alpha_m\left(L_a+L_g\right)$$

$$(2\text{-}34)$$

where, α_m and α_i represent, respectively, mirror losses and internal losses, and L_g and L_a represent, respectively, the gain and absorber section lengths, with:

$$\alpha_m=\left(\frac{1}{L}\right)\ln\left(\frac{1}{\sqrt{R_1 R_2}}\right)$$

$$(2\text{-}35)$$

where, $\left(L_g+L_a\right)=L$ and R_1, R_2 denote mirror reflectivities.

Substituting (2-35) into (2-34), we get:

$$\left(g_{\mathrm{mod}}(J)-\alpha_i\right)L_g=\left(a_0+\alpha_i\right)L_a-\left(\frac{1}{2}\right)\ln\left(R_1 R_2\right)$$

$$(2\text{-}36)$$

In the DDE model, G and Q describe the saturable gain and loss introduced by the gain and absorber sections, respectively, and $\kappa<1$ describes the total roundtrip non-resonant linear intensity losses. Thus, the threshold condition for lasing is given by:

$$\kappa e^{(G-Q)}=1$$

$$(2\text{-}37)$$

From (2-36) and (2-37), we find:

43

$$G = \left(g_{\text{mod}}(J) - \alpha_i\right)L_g$$

<div align="right">(2-38)</div>

$$Q = \left(a_0 + \alpha_i\right)L_a$$

<div align="right">(2-39)</div>

$$\kappa = \sqrt{R_1 R_2}$$

<div align="right">(2-40)</div>

Next, we derive expressions relating the saturable gain and loss (G and Q, respectively) to the unsaturated gain and absorption parameters (g_0 and q_0, respectively).

From the definitions given in [13], we have (ζ and τ represent, respectively, spatial and temporal coordinates in the frame of reference of the pulse):

$$G(\tau) = \int_{\zeta_3}^{\zeta_4} n_g(\tau,\zeta)\,d\zeta = \int_{\zeta_3}^{\zeta_4} \frac{v g_g \Gamma_g}{\gamma_q}\left[N_g(\tau,\zeta) - N_g^{tr}\right]d\zeta$$

<div align="right">(2-41)</div>

$$g_0 = \int_{\zeta_3}^{\zeta_4} j_g\,d\zeta = \int_{\zeta_3}^{\zeta_4} \frac{v g_g \Gamma_g}{\gamma_q^2}\left(J_g - \gamma_g N_g^{tr}\right)d\zeta$$

<div align="right">(2-42)</div>

substituting for $J_g = \gamma_g N_g$, we obtain:

$$g_0 = \int_{\zeta_3}^{\zeta_4} \frac{v g_g \Gamma_g}{\gamma_q^2}\left[\gamma_g N_g(\tau,\zeta) - \gamma_g N_g^{tr}\right]d\zeta$$

$$\Rightarrow g_0 = \int_{\zeta_3}^{\zeta_4} \left(\frac{v g_g \Gamma_g}{\gamma_q} \right) \left(\frac{\gamma_g}{\gamma_q} \right) \left[N_g(\tau,\zeta) - N_g^{tr} \right] d\zeta$$

$$= \Gamma \int_{\zeta_3}^{\zeta_4} \left(\frac{v g_g \Gamma_g}{\gamma_q} \right) \left[N_g(\tau,\zeta) - N_g^{tr} \right] d\zeta$$

(2-43)

where, $\Gamma \equiv \left(\tau_q / \tau_g \right)$.

Comparing (2-41) and (2-43), we get:

$$g_0 = \Gamma G$$

(2-44)

Similarly,

$$Q(\tau) = -\int_{\zeta_2}^{\zeta_3} n_q(\tau,\zeta) d\zeta = -\int_{\zeta_2}^{\zeta_3} \frac{v g_q \Gamma_q}{\gamma_q} \left[N_q(\tau,\zeta) - N_q^{tr} \right] d\zeta$$

$$Q(\tau) = -\int_{\zeta_2}^{\zeta_3} \frac{v g_q \Gamma_q}{\gamma_q^2} \left[\gamma_q N_q(\tau,\zeta) - \gamma_q N_q^{tr} \right] d\zeta$$

substituting for $\gamma_q N_q = J_q$, we obtain:

$$= -\int_{\zeta_2}^{\zeta_3} \frac{v g_q \Gamma_q}{\gamma_q^2} \left[J_q(\tau,\zeta) - \gamma_q N_q^{tr} \right] d\zeta$$

$$Q(\tau) = \int_{\zeta_2}^{\zeta_3} \frac{v g_q \Gamma_q}{\gamma_q} N_q^{tr} d\zeta \text{ , since } J_q(\tau,\zeta) = 0$$

$$Q(\tau) = \int_{\zeta_2}^{\zeta_3} \left(\frac{v}{\gamma_q} \right) \left(\frac{g_q \Gamma_q}{g_g \Gamma_g} \right) g_g \Gamma_g N_q^{tr} d\zeta$$

45

$$= s \int_{\zeta_2}^{\zeta_3} \frac{v g_g \Gamma_g}{\gamma_q} N_q^{tr} d\zeta$$

$$(2\text{-}45)$$

$$\text{where,} \quad s \equiv \frac{g_q \Gamma_q}{g_g \Gamma_g} = \frac{\left[\partial g_{\text{mod}}(J)/\partial J\right]_{g_{\text{mod}}(J)=0}}{\left[\partial g_{\text{mod}}(J)/\partial J\right]}$$

$$(2\text{-}46)$$

Also,

$$q_0 = \int_{\zeta_2}^{\zeta_3} j_q d\zeta = \int_{\zeta_2}^{\zeta_3} \frac{v g_g \Gamma_g}{\gamma_q} N_q^{tr} d\zeta$$

$$(2\text{-}47)$$

Comparing (2-45) and (2-47), we get

$$q_0 = (Q/s)$$

$$(2\text{-}48)$$

Finally, we constrain the regime of operation to stable, fundamental mode-locking using a dynamical stability analysis similar to that presented in Fig. 5 of [13].

A suitable constraint to achieve stable, fundamental mode-locking in terms of g_0 and q_0, is given by the locus of points lying on the line

$$q_0 = m g_0$$

$$(2\text{-}49)$$

where m represents the slope of a line in the g_0-q_0 plane, chosen to lie entirely within the region corresponding to the fundamental mode-locking regime.

Thus, we have, $\left(\dfrac{q_0}{g_0}\right) = m \Rightarrow \left(\dfrac{Q/s}{\Gamma G}\right) = m$. Therefore using equations (2-38), (2-39) and

(2-40):

$$\Gamma = \left(\frac{Q}{mGs}\right) = \frac{(a_0 + \alpha_i)L_a}{m(g_{mod}(J) - \alpha_i)L_g s}$$

(2-50)

Equations (2-38) – (2-40), (2-44), (2-46), (2-48) and (2-50) together provide a set of transformation relations that can be used to seed the DDE model given above in equations (2-31) – (2-33) with parameters extracted from values measured on the device under study.

2.4   Chapter Summary

In this chapter, a Delay Differential Equation (DDE) model for passive mode-locking in two section semiconductor lasers was introduced as a powerful and versatile, yet computationally less demanding alternative to conventional Traveling Wave models. The following were the key simplifying assumptions made:

i.   The linear cavity was modeled as a ring cavity with unidirectional wave propagation. This allowed for a sequential, lumped-element treatment of the light-matter interaction in each section, thereby simplifying the mathematical complications associated with simultaneous, distributed interactions in all sections.

ii. The barrier-well-dot formalism of the model, which necessitated a comprehensive consideration of dot-to-dot, dot-to-well and other transitions was replaced with a simple rate equation formalism involving a linear dependence on macroscopic carrier concentrations in the gain and the absorber sections. This led to a dramatic simplification in the number of equations and the associated parameter space of the model.

iii. Only ground state lasing was considered.

As a result of the simplifying assumptions in i. – iii. above, the original DDE model developed in [13] comprises a set of three coupled differential equations in the time domain, where the evolution of the intracavity field is described by a delay equation. Not only does this lead to a considerable reduction in the number of model equations, but the simplification of the spatio-temporal evolution of the field to pure temporal evolution enables a substantial reduction of computational cost. In addition, the parameter space of the model is now reduced to a mere 9 parameters.

New equations were then derived in order to provide a generalized framework for the transformation of experimentally measured quantities – specifically, gain and absorption measurements on the device under study using the Segmented Contact method [20, 21] – into dimensionless model parameters to seed the DDE model. This novel scheme greatly enhances the practical utility of the model as an elegant and powerful theoretical guide to next generation device design and analysis.

As will be seen in the next two chapters, aside from dramatically reducing the parameter space of the original DDE model (comprising a total of 9 parameters) to an absolute minimum of free parameters by a systematic process of constraining to values extracted

from measured quantities, many of the properties unique to QD systems are found to be actually embedded in the measurement-extracted model parameters, so that the model, with the inclusion of the newly-derived equations, provides invaluable insight into trends specific to an individual device by virtue of the fact that the parameters seeding the model were measured on the device.

In chapter 3, the analytical capabilities of the extended model are explored for a specific device. The first part of the chapter is devoted to an illustration of the process of transforming actual measurements into model parameters over a range of operating conditions along with an analysis of basic trends, while the remainder of the chapter presents specific instances of how the model can offer invaluable insight into experimentally-observed phenomena, particularly in the sudden and often unprecedented fluctuations of device output. Chapter 4 then explores some of the powerful capabilities of the extended model as a predictive guideline to device design/operation.

2.5   References for Chapter 2

[1] Rossetti, M., Bardella, P., Gioannini, M., & Montrosset, I. (2009, June). Time domain travelling wave model for simulation of passive mode locking in semiconductor quantum dot lasers. In *Lasers and Electro-Optics 2009 and the European Quantum Electronics Conference. CLEO Europe-EQEC 2009. European Conference on* (pp. 1-1). IEEE.

[2] Rossetti, M., Bardella, P., and Montrosset, I. (2009). "A time-domain travelling-wave model including multipopulation rate-equations for passively mode-locked quantum-dot lasers," in *1st EOS Topical Meeting on Laser*s, Capri, Italy.

[3] Rossetti, M., Bardella, P., Montrosset, I., Breuer, S., and Elsässer, W. (2010). "Simulation and design of quantum dot lasers operating in dual-wavelength passive mode-locking regime," in *15th European Conference on Integrated Optics* (ECIO2010).

[4] Rossetti, M., Bardella, P., & Montrosset, I. (2011). Time-domain travelling-wave model for quantum dot passively mode-locked lasers. *Quantum Electronics, IEEE Journal of*, *47*(2), 139-150.

[5] Viktorov, E. A., Mandel, P., Vladimirov, A. G., & Bandelow, U. (2006). Model for mode locking in quantum dot lasers. *Applied physics letters*, *88*(20), 201102-201102.

[6] Rossetti, M., Bardella, P., & Montrosset, I. (2011). Modeling passive mode-locking in quantum dot lasers: A comparison between a finite-difference traveling-wave model and a delayed differential equation approach. *Quantum Electronics, IEEE Journal of*, *47*(5), 569-576.

[7] Erneux, T., & Glorieux, P. (2010). *Laser dynamics*. Cambridge University Press.

[8] Erneux, T. (2009). *Applied delay differential equations* (Vol. 3). Springer.

[9] Otto, C., Lüdge, K., & Schöll, E. (2010). Modeling quantum dot lasers with optical feedback: sensitivity of bifurcation scenarios. *physica status solidi (b)*, *247*(4), 829-845.

[10] Otto, C., Globisch, B., Lüdge, K., Schöll, E., & Erneux, T. (2012). Complex dynamics of semiconductor quantum dot lasers subject to delayed optical feedback. *International Journal of Bifurcation and Chaos*, *22*(10).

[11] Rebrova, N., Huyet, G., Rachinskii, D., & Vladimirov, A. G. (2011). Optically injected mode-locked laser. *Phys. Rev. E*, *83*, 066202.

[12] Vladimirov, A. G., Turaev, D. and Kozyreff, G. (2004). Delay differential equations for mode – locked semiconductor lasers. *Opt. Lett.* ***29***, 1221 – 1223.

[13] Vladimirov, A. G., & Turaev, D. (2005). Model for passive mode locking in semiconductor lasers. *Phys. Rev. A*, *72*(3), 033808.

[14] Vladimirov, A. G., & Turaev, D. V. (2004). A new model for a mode-locked semiconductor laser. *Radiophysics and quantum electronics*, *47*(10-11), 769-776.

[15] Rafailov, E. U., M. A. Cataluna, and Wilson Sibbett (2007). "Mode-locked quantum-dot lasers." *Nature photonics* 1, no. 7: 395-401.

[16] Rafailov, E. U., Cataluna, M. A., & Avrutin, E. A. (2011). *Ultrafast Lasers Based on Quantum Dot Structures: Physics and Devices*. Wiley-VCH.

[17] Vasil'ev, P. (1995). *Ultrafast diode lasers: fundamentals and applications*. Norwood, MA: Artech house.

[18] Raghunathan, R., Crowley, M., Grillot, F., Li, Y., Mee, J. K., Kovanis, V., & Lester, L. F. (2013). Pulse Characterization of Passively Mode-locked Quantum Dot Lasers Using a Delay Differential Equation Model Seeded with Measured Parameters.

[19] Crowley, M. T., Murrell, D., Patel, N., Breivik, M., Lin, C. Y., Li, Y. & Lester, L. F. (2011). Analytical modeling of the temperature performance of monolithic passively mode-locked quantum dot lasers. *Quantum Electronics, IEEE Journal of*, *47*(8), 1059-1068.

[20] Blood, P., Lewis, G. M., Smowton, P. M., Summers, H., Thomson, J., & Lutti, J. (2003). Characterization of semiconductor laser gain media by the segmented contact method. *Selected Topics in Quantum Electronics, IEEE Journal of*, *9*(5), 1275-1282.

[21] Xin, Y. C., Li, Y., Martinez, A., Rotter, T. J., Su, H., Zhang, L., ... & Lester, L. F. (2006). Optical gain and absorption of quantum dots measured using an alternative segmented contact method. *Quantum Electronics, IEEE Journal of*, *42*(7), 725-732.

Chapter 3

Analytical Capabilities of the DDE Model

In this chapter, we use the novel formalism developed in Chapter 2 to transform experimental data measured on an actual device into dimensionless model parameters. The data was acquired over a range of different operating conditions, so that the accuracy of the model is validated over a range of operating conditions.

After a brief description of the layer structure and geometry of the device and a review of the new transformation relations derived in Chapter 2 in section 3.1, section 3.2 discusses a novel approach toward determining the carrier relaxation ratio of a device from gain and loss measurements, specific to its operating conditions. Not only is the method a potentially viable alternative to conventional pump-probe techniques, but the value extracted using this approach yields the carrier relaxation ratio for the entire device, as opposed to the pump-probe method, where the approach is to perform measurements individually on the gain and absorber sections.

Section 3.3 demonstrates the use of the model as an analytical tool with measurement-extracted parameters. After a basic demonstration of pulse-trimming with parameters corresponding to increasing absorber bias voltage in subsection 3.3.1, subsections 3.3.2 and 3.3.3 are devoted to parameter sensitivity-analysis studies devoted, respectively, to the linewidth enhancement parameter and to the unsaturated gain and absorption parameters.

Finally, section 3.4 explores the analytical capabilities of the model in relation to output pulse dynamics. The results of simulation are shown to provide invaluable insight into

experimental observations acquired using standard pulse characterization techniques such as Frequency Resolved Optical Gating (FROG) and Autocorrelation. Conclusions are given in section 3.5.

3.1 Description of Simulated Device

The device studied in this work is an 8-stack, dots-in-a-well (DWELL) laser structure grown by elemental source molecular beam epitaxy (MBE), with a 7-mm gain section and a 1-mm absorber section generating a 4.96 GHz pulse repetition rate under fundamental mode-locking. A schematic of the device with important details of the epitaxial layer structure is shown below in Fig. 3-1.
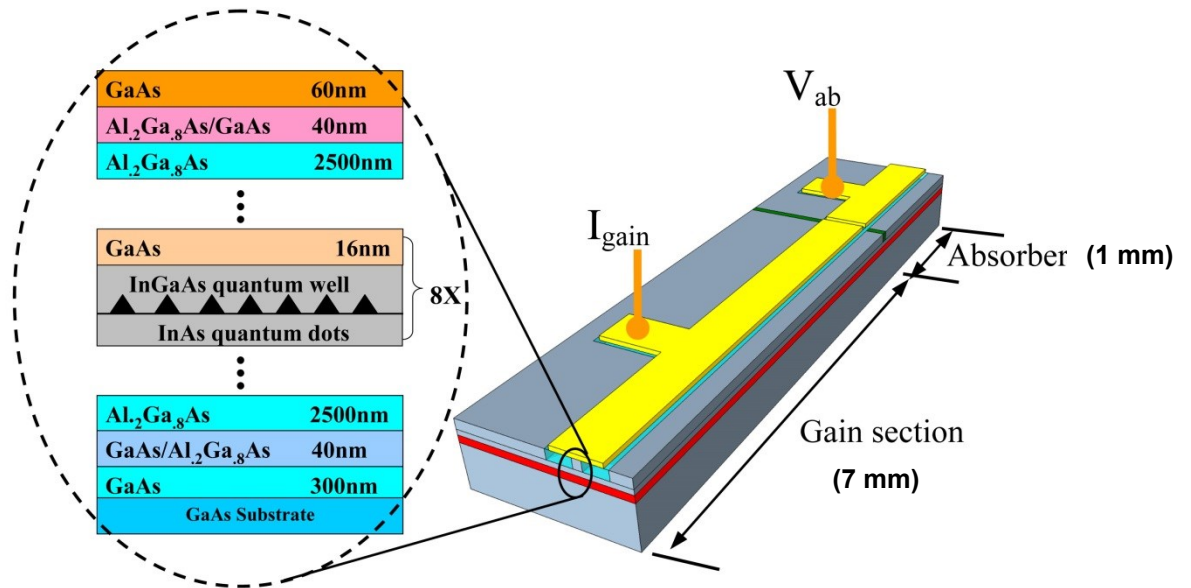
Figure 3-1: Device schematic including details of epitaxial structure.

From Chapter 2, we recall the following set of transformation relations [1] that can be used to seed the DDE model given in equations (2-31) – (2-33) with parameters extracted from values measured on the device under study:

$$G = \left(g_{\text{mod}}(J) - \alpha_i\right)L_g$$

(2-38)

$$Q = \left(a_0 + \alpha_i\right)L_a$$

(2-39)

$$\kappa = \sqrt{R_1 R_2}$$

(2-40)

$$g_0 = \Gamma G$$

(2-44)

$$s \equiv \frac{g_q \Gamma_q}{g_g \Gamma_g} = \frac{\left[\partial g_{\text{mod}}(J)/\partial J\right]_{g_{\text{mod}}(J)=0}}{\left[\partial g_{\text{mod}}(J)/\partial J\right]}$$

(2-46)

$$q_0 = \left(Q/s\right)$$

(2-48)

$$\Gamma = \left(\frac{Q}{mGs}\right) = \frac{\left(a_0 + \alpha_i\right)L_a}{m\left(g_{\text{mod}}(J) - \alpha_i\right)L_g s}$$

(2-50)

The parameters appearing on the right-hand side of equations (2-38)-(2-40), (2-44), (2-46), (2-48) and (2-50) can be readily measured as a function of gain-section current

55

density, wavelength, absorber reverse bias and temperature using the segmented contact method [2, 3].

3.2   Novel Approach to Estimate the Carrier Relaxation Ratio of the QDMLL [4]

One of the novel findings of this dissertation lies in the newly derived expression (2-50) [4]. The parameter Γ is known as the Carrier Relaxation Ratio of a QDMLL, and is defined as the ratio of the absorber recovery time $\left(\tau_{abs}\right)$ to the gain recovery time $\left(\tau_{gain}\right)$, as might be recalled from Chapter 2. Because of the fact that the interplay between gain and absorber dynamics is critical to the mode-locking process, this parameter is critically important to pulse quality in the mode-locking process.

The standard technique to determine this parameter involves measuring gain and absorber recovery times using pump–probe techniques, individually for the semiconductor optical amplifier [5] corresponding to the gain section, and for the saturable absorber [6, 7] corresponding to the absorber section of the two-section laser. The approach discussed in this work provides an analytical expression for the carrier relaxation ratio as a function of static parameters that can be easily measured on a multi-section QD laser test structure over temperature, current density, bias voltage and wavelength. This allows mapping-out the carrier relaxation ratio of the QDMLL over a range of operating conditions, each of which can be used as an input parameter in the DDE model in order to simulate device performance at that condition, while circumventing the need to perform pump-probe measurements.

The model parameter values used in determining Γ are summarized in Table 3-1 (-3V absorber bias and device temperatures of 20 ^{o}C, 30 ^{o}C, 40 ^{o}C, 50 ^{o}C & 60 ^{o}C), and represent values at the onset of mode-locking, i.e., the point at which a pulse was observed on an autocorrelator [8]. The data from which model parameters were extracted was measured on Zia Laser Wafer 967.

Table 3-1: *Measured/extracted temperature-dependent parameter values (dimensionless) at the onset of mode-locking for a -3V absorber bias (Wafer ZLG967).*

T(°C)	G	Q	G-Q	Q/G	s	Γ
20	4.22	3.20	1.02	0.76	4.65	0.08
30	4.18	3.33	0.85	0.79	5.89	0.07
40	3.95	3.43	0.52	0.87	8.47	0.05
50	3.33	3.03	0.30	0.91	10.68	0.04
60	2.89	2.43	0.46	0.84	12.20	0.03

This data is plotted in Fig. 3-2 (solid squares), along with the values of absorption recovery times reported in [7] (solid circles) as a function of temperature. The similarity of the two plots suggests that the trend exhibited by equation (2-50) for Γ over temperature follows the trend exhibited by the absorption recovery time τ_a.
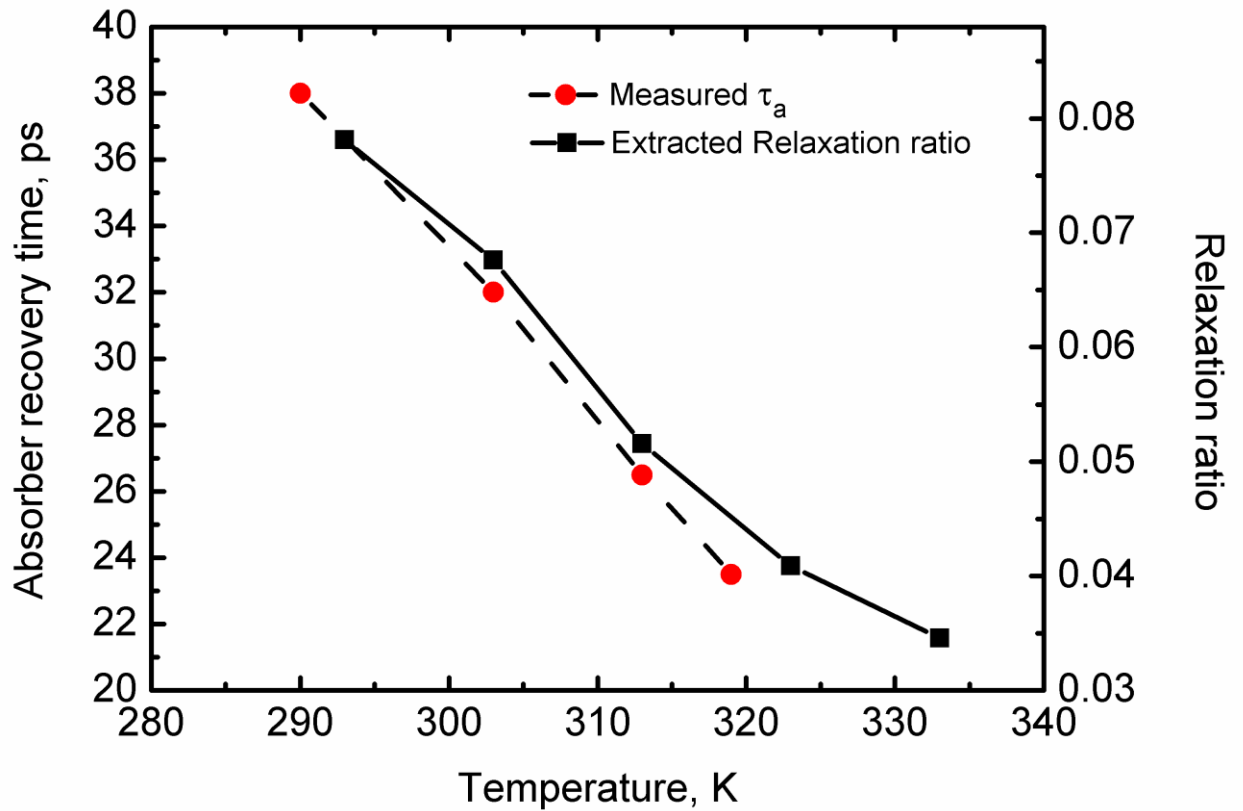
Figure 3-2: *Comparative plots of experimentally measured* τ_a *(solid circles) [7] and extracted relaxation ratio (solid squares) v/s temperature.*

As a comparison, the pump-probe characterization of the absorber recovery times reported in [7] measured a decrease in the absorption recovery time with increasing temperature for a constant reverse bias of 2 V (the device studied in that work comprised a 190 nm active region, which corresponds to an electric field of 105 kV/cm). For a similar temperature range, with a 3V reverse bias (288 nm active region, yielding an electric-field of 104 kV/cm) and a similar QD epitaxial-structure, we extract a comparable decrease in Γ as seen from Fig. 3-2. While it is known that both gain and

absorption recovery times decrease with temperature ([7], [9]), the similarity in the trends discussed above, together with the decreasing value of Γ in Table 3-1 is strongly suggestive that τ_a is the dominant factor in determining the behavior of Γ. Thus, it may be inferred that a decreasing value of Γ with increasing temperature suggests that the absorber recovery time decreases by a significantly larger factor than the corresponding reduction in the gain recovery time.

Table 3-2 shows the variation of the extracted relaxation ratio using parameters from Wafer ZLG967 at a fixed temperature of 20 $^{\circ}$C, for absorber bias voltages of 0V, -3V and -5V, wherein, a trend similar to that seen with increasing temperature is observed for Γ.

Table 3-2: *Measured/extracted absorber bias voltage-dependent parameter values*

(dimensionless) at the onset of mode-locking at 20 $^{\circ}$C (Wafer ZLG967)

V	G	Q	G-Q	Q/G	s	Γ
0	3.36	2.33	1.03	0.69	2.70	0.13
-3	4.22	3.20	1.02	0.76	4.65	0.08
-5	4.6	3.62	0.98	0.79	7.40	0.05

Again, the carrier relaxation ratio shows a decrease with increasing reverse bias. This trend agrees with the results obtained in [6] using pump-probe techniques, and supports the experimentally observed phenomenon that stronger bias voltages produce narrower pulses, given that pulse trimming is achieved primarily with faster absorption recovery rates, which shortens the net gain window during which pulses are generated.

In view of the discussion above, it can be seen that the trends exhibited by the carrier

relaxation ratio Γ extracted from gain $-$ loss data acquired by the segmented contact method using the expression derived in equation (2-50) closely mirrors the trends that can be expected by individually measuring τ_g and τ_a using pump-probe techniques, for a range of operating temperatures and bias voltages. Thus, it is reasonable to expect that this method of extracting Γ from gain and loss data provides a viable alternative to pump-probe measurements.

3.3   Transformation of Measured Values to Model Parameters [1]

The expressions (2-38) $-$ (2-40), (2-44), (2-46), (2-48) and (2-50) derived in Chapter 2, particularly for the carrier relaxation ratio Γ, provide an elegant and convenient technique to accurately determine device-specific dimensionless parameters for input into the DDE model. Such a situation may be envisioned for a case where device performance needs to be simulated over a range of operating conditions.

A close examination of the system of DDEs given in equations (2-31) $-$ (2-33) reveals the parameter space involved. Thus, in order to model a QDMLL realistically, it is imperative to constrain as many of the parameters as possible to values obtained from measurements on an actual QD device. The simulation results, obtained by seeding the model with these parameters (transformed to dimensionless form, using the relations derived in Chapter 2), can then be used to interpret and characterize the mode-locking performance of the same device.

Since the onset of mode-locking occurs at or beyond threshold, threshold values provide a convenient set of initial conditions for equations (2-31) $-$ (2-33). The first step, then, is

to use values measured at threshold in equations (2-38) and (2-39) to calculate $G(0)$ and $Q(0)$, and then use the values of $G(0)$ and $Q(0)$ in equations (2-44) and (2-48) to calculate the corresponding unsaturated parameters, g_0 and q_0, at threshold. Further, parameters κ and s can be directly found from equations (2-40) and (2-46), respectively, while the carrier relaxation ratio (Γ) is extracted from equation (2-50). Next, the absorber relaxation time is used to infer the delay parameter (T) and the spectral filtering coefficient (γ) for each operating condition as follows. The delay parameter (T) is calculated for each case by simply scaling the cavity round trip time to the absorber relaxation time for that case. In all cases, the absorber relaxation time was estimated from the experimental results in [6] and [7] for a saturable absorber with an epitaxial layer structure similar to the device simulated in this work, following from the discussion in the previous section. For instance, at an operating temperature of 20 °C, the bias voltage applied on the absorber section was expressed as an electric field strength across the active region. This value was then converted back to a bias voltage for the saturable absorber structure studied in [6], and the corresponding value of absorber relaxation time was found from Fig. 2b of [6]. For higher temperatures, the exponential expression for thermionic emission given in equation (2) of [7] was used to estimate the same. Also, the spectral filtering coefficient (γ) was estimated from the measured optical spectrum of the device as the product of the number of cavity modes taking part in the mode-locking process and the cavity inter-mode frequency spacing (T^{-1}). Finally, the linewidth enhancement parameters in the gain and absorber sections were chosen such that the steady state pulse width obtained from simulation was consistent with the typical pulse width measured on an autocorrelator for the actual device.

Now, having reduced the number of free parameters to two (namely, the linewidth enhancement factors in the gain and absorber sections), we set the two to be equal in order to simplify the analysis. Previous work [10, 11] has shown that this case corresponds to the most stable operating point, according to the DDE model. While this assumption could result in some departure from the actual values that the linewidth enhancement factors in the gain and absorber sections might take, the primary objective here is to study the broad trends, and how they might affect device performance. Further, it is reasonable to expect that any such departure may be marginal close to threshold, considering that the device under study in this work has a significantly longer gain section, so that the device behavior can be expected to be dominated by the gain section component. This value is then fit to the deconvolved autocorrelator pulse width measurement.

The results shown in the following were obtained as follows. The parameter values measured/extracted as discussed above were used as initial conditions for the simulations. The system of equations defining the model (equations (2-31), (2-32) and (2-33)) was then integrated over two thousand round trip times to allow transients to settle.

Table 3-3 lists a set of sample parameter values used to seed the simulations with parameters measured/extracted at saturable absorber bias conditions of 0V, -3V and -5V, at a temperature of 20 $^{\circ}$C. As mentioned at the beginning of this section, the parameter values were obtained from the experimental data presented in [8], and made dimensionless for input into the model.

Table 3-3: *Simulation parameters over bias voltage at 20 °C (Wafer ZLG967)*

Parameter	0 V	-3 V	-5V
T	3.23	5.00	6.67
G(0)	3.33	4.18	4.18
Q(0)	2.33	3.20	4.55
α_g	0.1	0.2	0.5
α_q	0.1	0.2	0.5
s	2.68	4.65	6.90
Γ	0.13	0.08	0.08
γ	29.14	39.15	41.10
κ	0.55	0.55	0.55

The parameter values presented in Table 3-3 correspond to threshold conditions, i.e., current density values of 357 A/cm^2 at 0V, 462 A/cm^2 at -3V and 537 A/cm^2 at -5V (ref: Tables I and II of [8]). It may be noted that while the table lists a particular sample pair of values for α_g and α_q for each absorber bias voltage, these were typically chosen in each case to simulate the experimentally-observed pulse structure or duration. As a first step, it is fairly straightforward to check if the extended formalism of the DDE model, using model parameters extracted from measured data, can capture well-known trends in QDMLLs, such as the effect of an increased absorber bias in trimming the pulses.

3.3.1   Pulse-Trimming with Stronger Absorber Bias Voltage [12]

Fig. 3-3a shows the steady state output of the system of equations in (2-31) – (2-33), for the case $\alpha_g = \alpha_q = 2.5$. The delay parameter T has been scaled using a characteristic timescale of 62 ps, which was inferred from measurements performed on a QD saturable absorber with a similar epitaxial structure [6], using an equivalent value of active region field strength.

In the absence of an applied bias on the absorber section, there is no sweep-out mechanism as a result of the associated electric field to expedite the carrier relaxation rate in the absorber section. Thus, the absorber takes a longer time to recover, resulting in sub-optimal pulse trimming. Thus, the simulation results predict broad pulses, with a width ~ 23 ps (Fig. 3-3b).

a.)

STEADY STATE FIELD INTENSITY
(T = 20 C, J = Jth = 357 A/cm^2, Vabs = 0 V, alpha$_g$ = alpha$_q$ = 2.5)

~ 23 ps

INTENSITY $|A|^2$ (a. u.)

ROUNDTRIP NUMBER
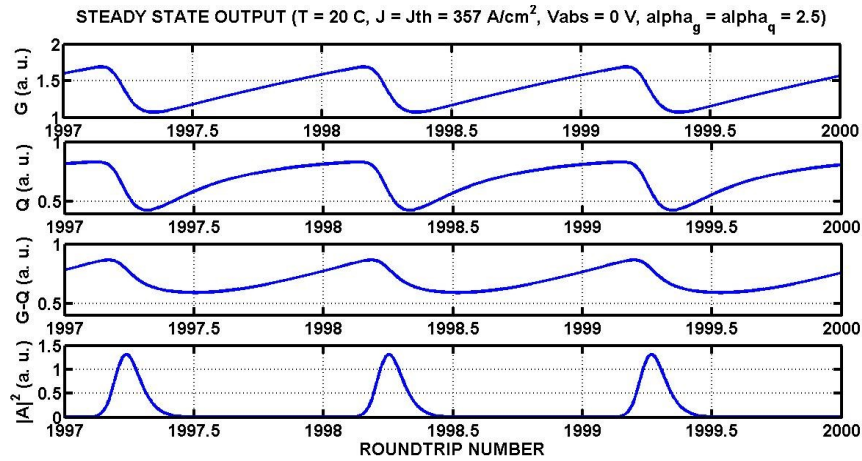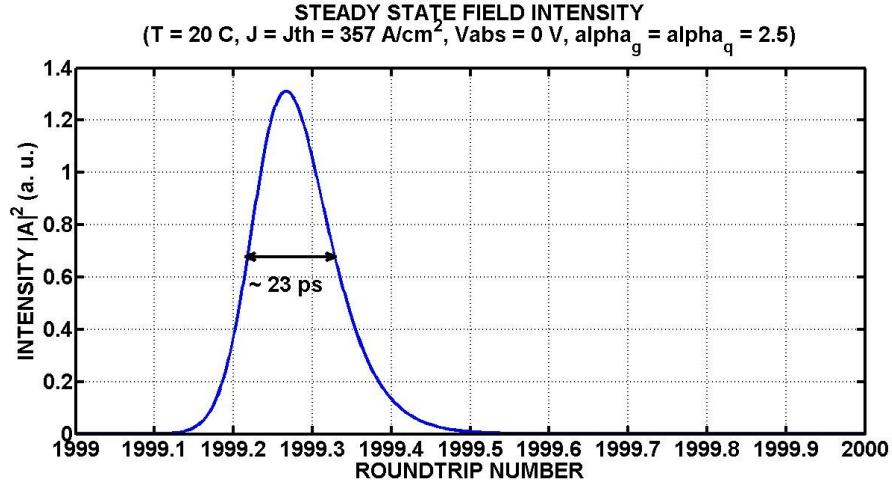
b.)

Figure 3-3a.): *Steady state simulation result for 0 V absorber bias, $\alpha_g = \alpha_q = 2.5$: G(τ), Q(τ),*

*(G(τ)-Q(τ)) and $|A(\tau)|^2$ **b.)** Steady state pulse intensity profile for 0 V absorber bias,*

$$\alpha_g = \alpha_q = 2.5.$$

Next, the effect of an applied (moderate) bias voltage is considered, with V_{abs} = -3V. Again, in this case, all other parameters are constrained to extracted values, and the effect of the linewidth enhancement factor is analyzed by simulation. The second column of Table 3-3 lists a sample set of parameter values, extracted from gain and loss spectra at 20 C and an applied absorber bias of -3V at threshold (current density = 462 A/cm^2). Again, using the measurements reported in [6], the delay parameter *T* was scaled to a characteristic timescale of 40 ps. Fig. 3-4a.) shows the simulation output for the case $\alpha_g = \alpha_q = 1.8$. Compared to the previous case with no applied bias, the net gain profile in the third panel shows a sharper profile, suggesting a shorter interval of high net gain – this is seen as considerably better trimmed pulses in the fourth panel, with a pulse width ~ 10 ps (Fig. 3-4b.)).

STEADY STATE OUTPUT
(T = 20 C, J = Jth = 462 A/cm², Vabs = -3 V, alpha$_g$ = alpha$_q$ = 1.8)
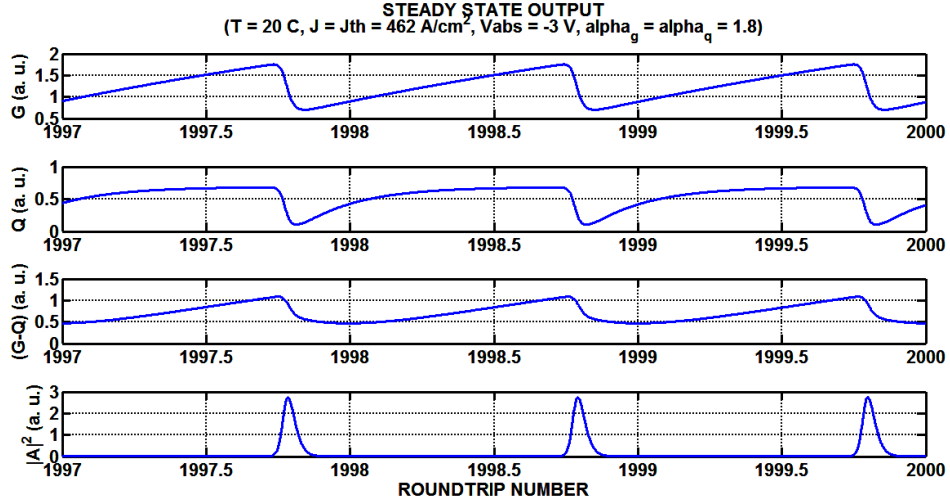
Figure 3-4a.): *Steady state output for -3 V absorber bias,* $\alpha_g = \alpha_q = 1.8$*: G(τ), Q(τ), (G(τ)-Q(τ))*

and $|A(\tau)|^2$*.*

STEADY STATE FIELD INTENSITY
(T = 20 C, J = Jth = 462 A/cm², Vabs = -3V, alpha$_g$ = alpha$_q$ = 1.8)
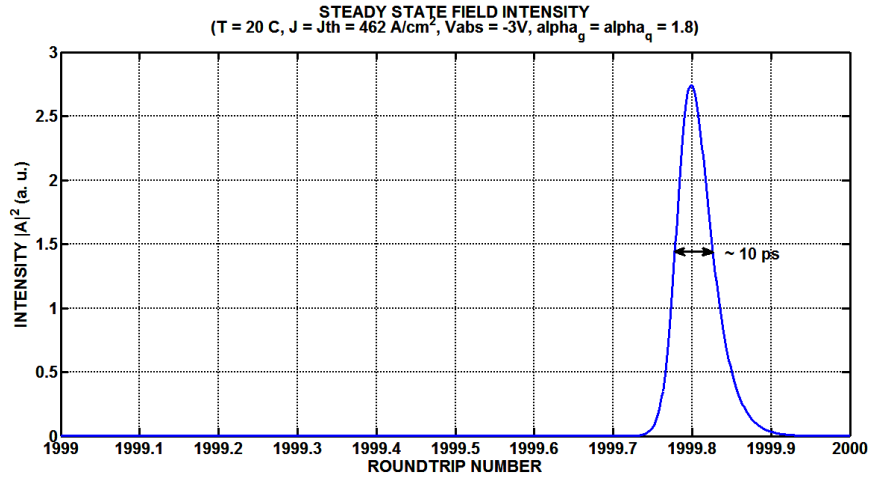
Figure 3-4b.): *Steady state pulse intensity profile for -3 V absorber bias,* $\alpha_g = \alpha_q = 1.8$*.*

Finally, we consider the effect of a strong applied bias of -5 V on the absorber section.

The third column of Table 3-3 lists a sample set of parameter values, extracted from gain

and loss spectra at 20 C and an applied absorber bias of -5V at threshold (current density

= 537 A/cm²). Again, using the measurements reported in [6], the delay parameter *T* was

scaled to the characteristic timescale, chosen to correspond to an absorber recovery time

66

of 30 ps. Fig. 3-5a.) shows the simulation output for the case $\alpha_g = \alpha_q = 0.8$.
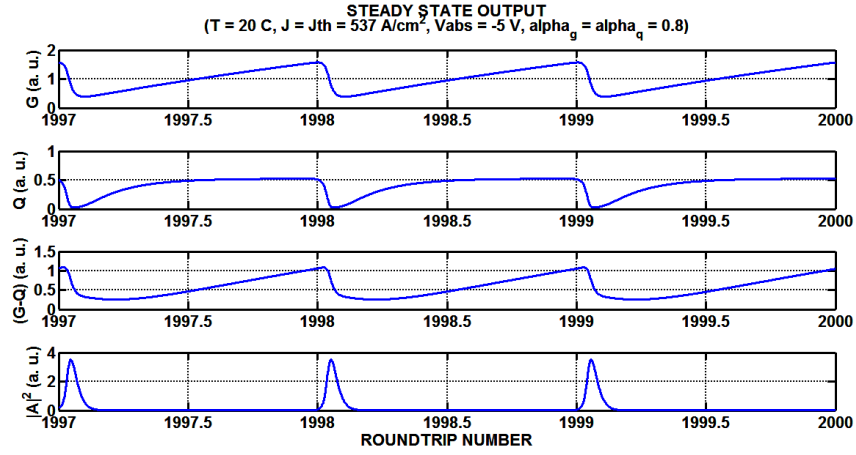
Figure 3-5a.): *Steady state output for -5 V absorber bias, $\alpha_g = \alpha_q = 0.8$: G($\tau$), Q($\tau$), (G($\tau$)-*

Q(τ)) and $|A(\tau)|^2$.

In this case, we find, comparing the first and second panels in Fig. 3-5a.) to the corresponding panels in Fig. 3-4a.), that while the saturable gain profile in both cases follows a similar trend, the saturable loss saturates at a lower value for a higher bias. The lower losses lead to a slightly higher net gain window than the -3 V case, so that pulses are trimmed to ~ 8.75 ps (Fig. 3-5b.)).
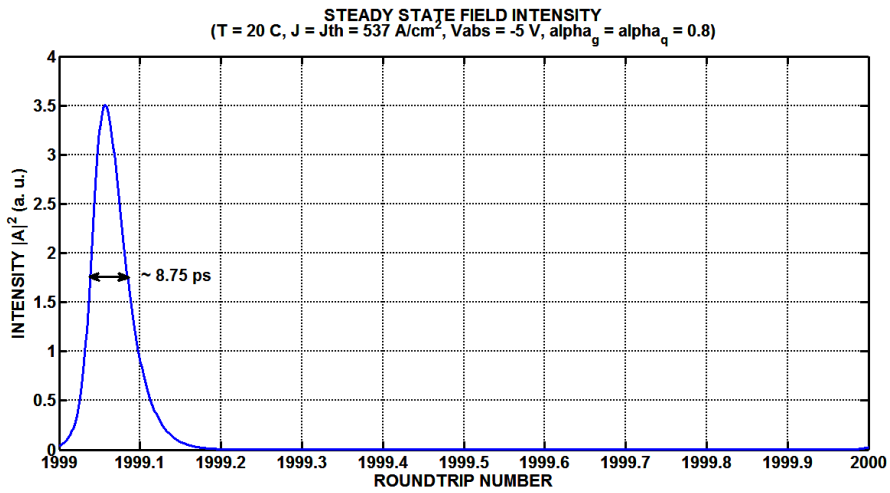
Figure 3-5b.): *Steady state pulse intensity profile for -5 V absorber bias, $\alpha_g = \alpha_q = 0.8$.*

The set of trends discussed in this subsection have also been simulated with parameters extracted on other two-section QDMLLs. On the one hand, this can be used to get a sense of the set of parameter values under which a given device will generate a certain output. In a broader context, however, it is essential to recognize the power of being able to constrain most of a small parameter space to values measured on a device, operated under a certain set of conditions. First, this provides a natural scheme for a sensitivity analysis on a given parameter that can be varied over a range, while all other parameters are held fixed. Such an analysis can then be used to infer parameter ranges over which device operation can be expected to be stable. In the remainder of this chapter, the analytical capabilities of the model are demonstrated, first in the context of parameter sensitivity-analysis, and later, to study sudden dynamical transitions in pulse shape.

3.3.2   Impact of the Linewidth Enhancement Factor (α – parameter)

One of the important analytical capabilities of our extended model is the ability to gain insight into the range of values of the linewidth enhancement factor for stable, fundamental mode-locking to be likely. It is seen that the linewidth enhancement factors in the gain and absorber sections have a profound influence on pulse structure, so that past a certain value of the linewidth enhancement factor, instabilities emerge in the structure. Typical examples of instabilities of this type include pulse splitting and satellite pulses, detailed analyses of which will be performed in Chapter 4.

Consequently, sudden changes in pulse structure were used to determine mathematical ranges for the linewidth enhancement factor for stable, fundamental mode-locking to be likely. Table 3-4 summarizes the mathematically likely ranges for α_g and α_q discussed

above, and the values used in each case to obtain a pulse width closest to what was

obtained experimentally from autocorrelator (AC) measurements.

Table 3-4: *Likely α - parameter ranges for stable, fundamental ML over bias voltage at 20 °C*

(Wafer ZLG 967).

V_{abs}	Range of α	$\alpha_g = \alpha_q$
0	$0 < \alpha_g = \alpha_q < 2.6$	0.1
-3	$0 < \alpha_g = \alpha_q < 2.1$	0.2
-5	$0 < \alpha_g = \alpha_q < 1.2$	0.5

For instance, for the 5V reverse bias case, the mathematically permissible range of α_g

and α_q extends to 1.1, past which the structure of individual pulses exhibits instabilities

such as splitting, as shown in Fig. 3-6 for $\alpha_{g,q} = 1.2$ (black pulse train), in sharp contrast

to the stable pulses obtained with $\alpha_{g,q} = 0.5$ (green pulse train).
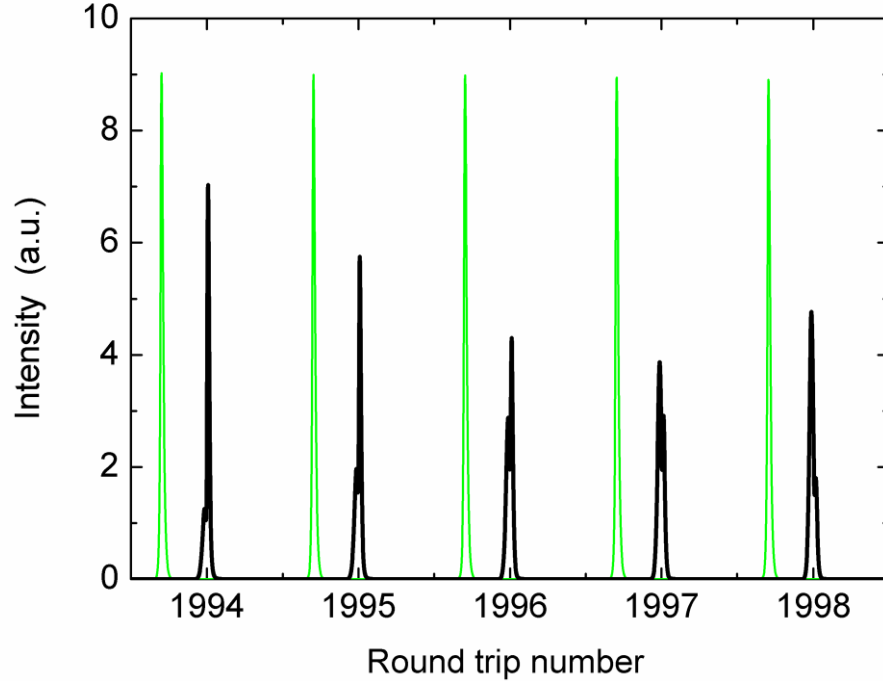
Figure 3-6: *Simulation results at 20 C and 5V absorber reverse bias. Green pulse train is for*

$\alpha_{g,q}$ *= 0.5 and the black pulse train is for* $\alpha_{g,q}$ *= 1.2, refer to Table 3-4.*

As presented in Table 3-4, the general trend with increasing reverse bias is to reduce the range of acceptable linewidth enhancement factors for stable locking, although the device itself operates at a larger value with increasing reverse bias because of the consequent increase in threshold. Although a larger linewidth enhancement factor results in pulse broadening due to self-phase modulation, the improved pulse trimming at higher reverse bias in the absorber can help counteract this effect. The physics of these processes are all accounted for in the model.

3.3.3. DDE Simulations as an indicator of lower unsaturated gain and absorption in QD devices

Since the unsaturated gain and loss parameters are expected to be lower for QD structures in comparison to QW structures, the effect of varying this pair of parameters was important to this study.

For an operating temperature of 20 $^{\circ}$C and no applied reverse bias, the values of g_0 and q_0 can be extracted from the parameter values listed in the first column of Table 3-3 using equations (2-44) and (2-48). Next, keeping all other parameters unchanged from Table 3-3, g_0 and q_0 are each scaled-up by a factor of 10. As seen clearly from Fig. 3-7a.), this leads to significant instabilities in the steady-state output.
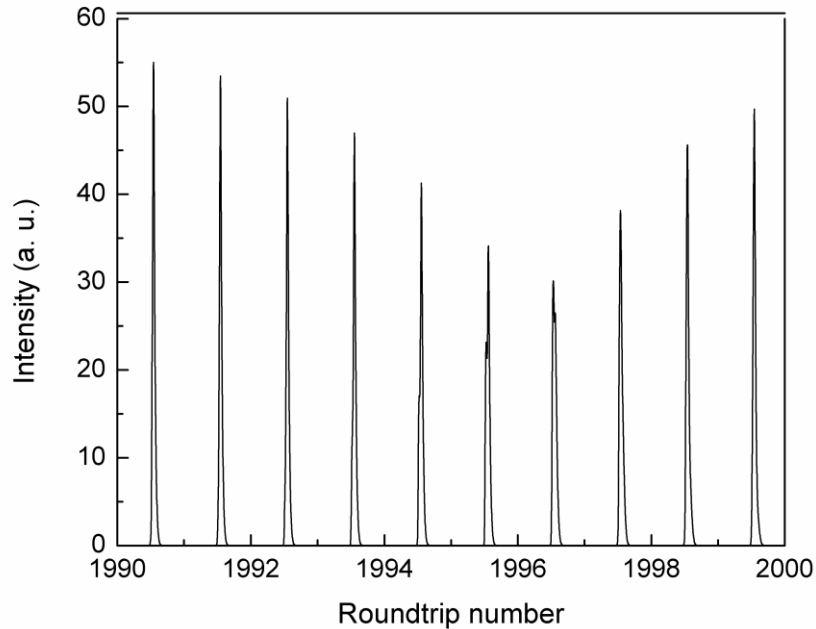
Figure 3-7a.): *Simulation results at 20 C, 0V absorber bias obtained with g_0 and q_0 increased 10-fold (all other parameters as in Table 3-3) show fluctuating intensities.*

Moreover, under the influence of an applied reverse bias on the absorber section or an elevated temperature, the simulation results are stable for an even smaller range of unsaturated gain and absorption. For instance, for the cases T = 20 $^{\circ}$C, -3 V bias (Fig. 3-7b.)) and T = 60 $^{\circ}$C, 0 V bias (Fig. 3-7c.)), keeping all other parameter values unchanged, g_0 and q_0 were each scaled-up by a factor of 5, whereby, the output is seen to have switched to higher-order mode-locking.
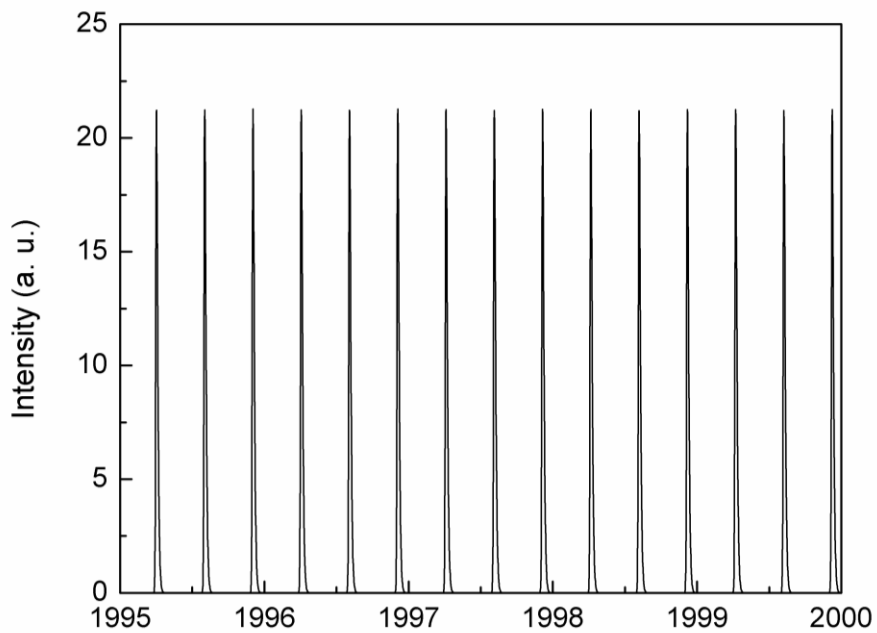
Figure 3-7b.): Simulation results at 20 C, -3V absorber bias obtained with g_0 and q_0 increased 5-fold (all other parameters as in Table 3-3) show a transition to higher-order mode-locking.
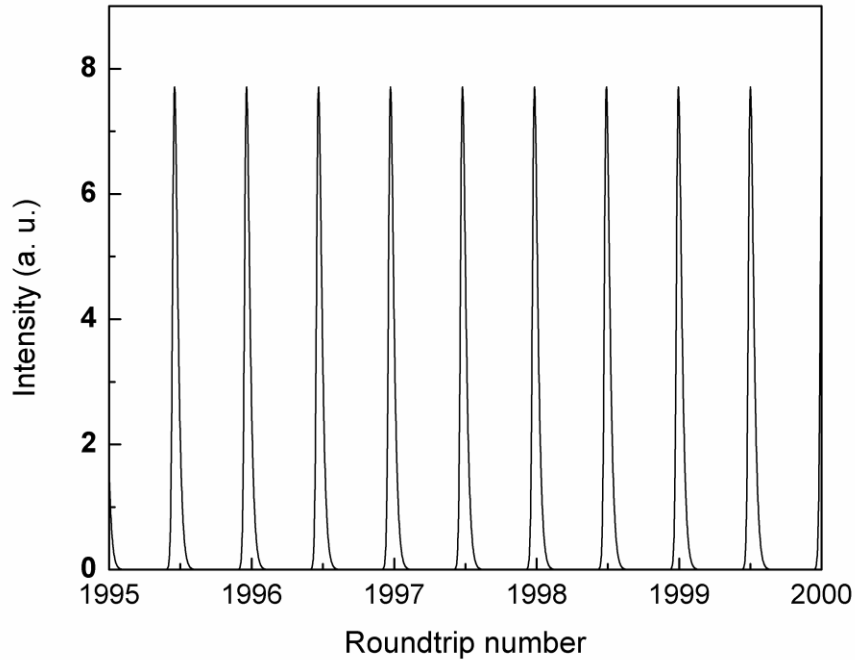
Figure 3-7c.): *Simulation results at 60 C, 0V absorber bias obtained with g_0 and q_0 increased*

5-fold show a transition to higher-order mode-locking.

This suggests that even a five-fold increase in the values of g_0 and q_0 (which represents values typical of QW devices), is impractical for stable, fundamental mode-locking for the QD device under study. This is strongly suggestive that in order for QD systems to achieve stable pulsation at elevated temperatures or under reverse bias, the values of unsaturated gain and absorption must be on the order of the values extracted in Table 3-3. Higher values tend to push the system out of the stable, fundamental mode-locking regime. In other words, the simulations show that lower values of unsaturated gain and absorption in the QD device under study compared to a QW version are necessary to achieve stable, fundamental mode-locking. These simulation results broadly support the extensive experimental findings in [13]-[16], especially at higher temperatures.

3.4 Pulse Shape Analysis with the DDE Model

3.4.1 Shortcomings of Autocorrelator Data

Table 3-5 gives a comparison between typical pulse widths obtained experimentally from autocorrelator measurements (assuming a sech^2-intensity profile [17]), and the corresponding values obtained by simulation using the DDE model. Comparing the last two columns shows very good agreement between the two.

Table 3-5: *A comparison of pulse widths obtained experimentally and from simulation results over bias voltage at 20 ^oC*

Absorber BiasVoltage (V)	Measured Autocorrelator Pulse Width (ps)	Deconvolved Pulse Width (ps)	DDE Model Simulated Pulse Width (ps)
0	25	16	16.25
-3	8	5.12	5
-5	5	3.2	3.75

However, as seen from the pulse profiles in Fig. 3-8 a.), b.) and c.), autocorrelation measurements yield just a single pulse. But a look at pulse trains over extended periods of time (obtained by simulation) reveals a rather startling possibility.

STEADY STATE FIELD INTENSITY
(T = 20C, V_{abs} = 0V)

a.)

STEADY STATE FIELD INTENSITY
(T = 20C, V_{abs} = -3V)

b.)

STEADY STATE FIELD INTENSITY
$(T = 20C, V_{abs} = -5V)$

(inset: Steady State Pulse Intensity — PROFILE (a. u.) vs ROUNDTRIP NUMBER)

c.)
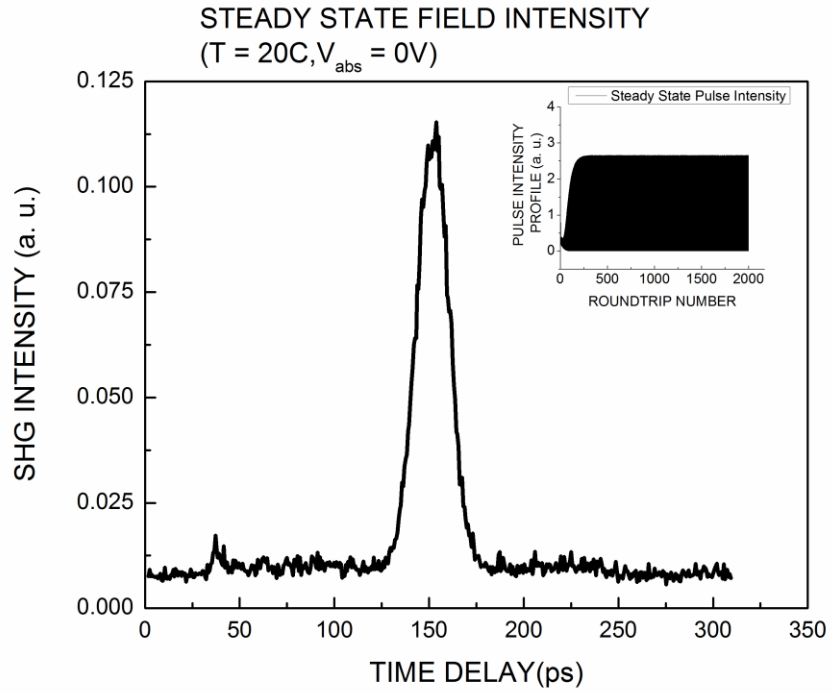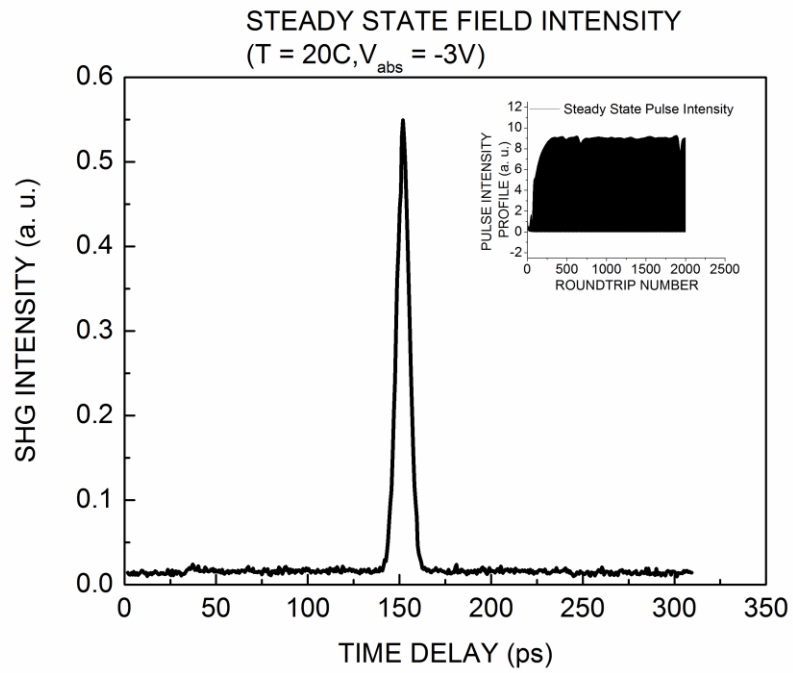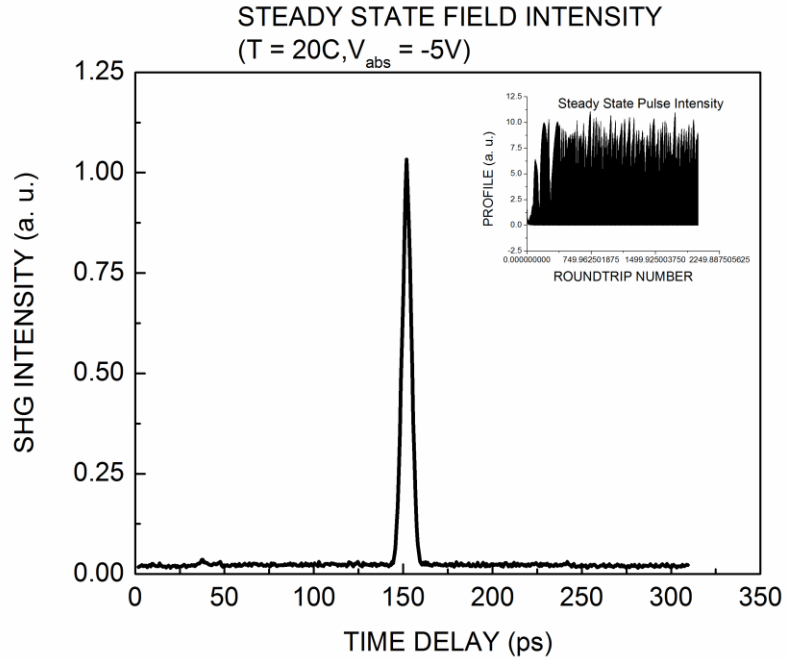
*Figure 3-8: Autocorrelator pulse measurements at 20 ℃, **a.)** 0V bias (inset shows DDE simulations predict stable, fundamental mode locking for this case) **b.)** -3V bias (inset shows DDE simulations predict fundamental mode-locking on the verge of instability for this case), and **c.)** -5V bias (inset shows DDE simulations predict highly unstable mode-locking for this case).*

As seen from the simulation results in the insets in Fig. 3-8 a.), b.) and c.), fundamental mode-locking is predicted to be very stable for a 0V absorber bias, on the verge of instability for a -3V absorber bias, and highly unstable for a -5V absorber bias, suggesting the possibility that the device may be Q-switched/pulsing in the last case, but not stably mode-locked. This information is obscured by autocorrelation measurements, where the formation of a single pulse with a reasonable pulse width may be taken as evidence of stable mode-locking. Thus, to address subtleties in the DDE model regarding pulse shape, and not just width, a more complete characterization of the pulse is required.

In the next section, FROG is used to measure the evolution of the pulse shape with increasing absorber bias and compared to the DDE model.

3.4.2. Correlation with Frequency Resolved Optical Gating (FROG) Measurements

The schematic diagram of the collinear second harmonic generation (SHG) FROG system is shown in Fig. 3-9 [18, 19]. The optical output of the laser is collected with an optical head, which integrates a lens, an isolator and a short 1-m single-mode polarization-maintaining (PM) fiber pigtail, and then is coupled into the FROG system through a PM fiber. The pulse train is sent into a free-space Michelson interferometer (MI) to produce pulse pairs with variable delay that are coupled into an aperiodically poled lithium niobate (A-PPLN) waveguide with a 6-cm long poling region to produce a SHG signal. The variable delay was produced by a voice coil-actuated servo having a delay resolution of 3.5 fs. The servo can be controlled either digitally via computer or by an analog waveform. The two delay pulses were sent collinearly into an A-PPLN waveguide.

The A-PPLN chip improves SHG conversion efficiency of the mode-locked diode lasers to a level that allows real-time data acquisition. By comparing the original QDMLL wavelength spectrum with the value computed from the FROG measurement, the bandwidth of the A-PPLN is verified to be sufficiently wide. At each relative time delay between the two pulse replicas, the SHG spectrum is recorded using an Ocean Optics QE65000 spectrometer. Because of the collinear geometry, interference fringes are produced. By applying an AC modulation to the servo position, the delay is modulated, and the fringes are averaged out if a sufficiently long integration time is used. The DC background from the low pass filtered FROG trace is removed using background

subtraction [20, 21]. The data acquisition, preprocessing and processing were done using commercial FROG software that was developed by Mesa Photonics.
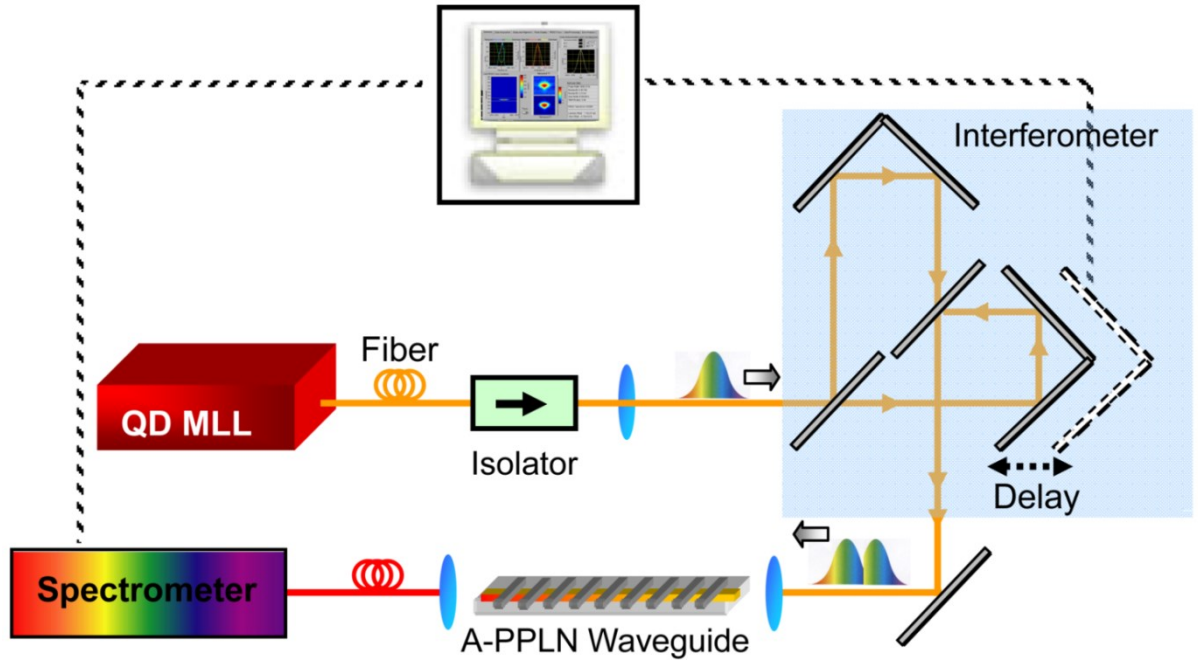
Figure 3-9: Experimental setup of the collinear SHG FROG system.

FROG measurements on the device under study in this work revealed a curious trend. As seen from Fig. 3-10 a.), a bias condition of a 95 mA gain current and a -3 V bias on the absorber section yielded a temporal pulse shape which is typical for such devices, with a steep rising edge, and a slower falling edge.
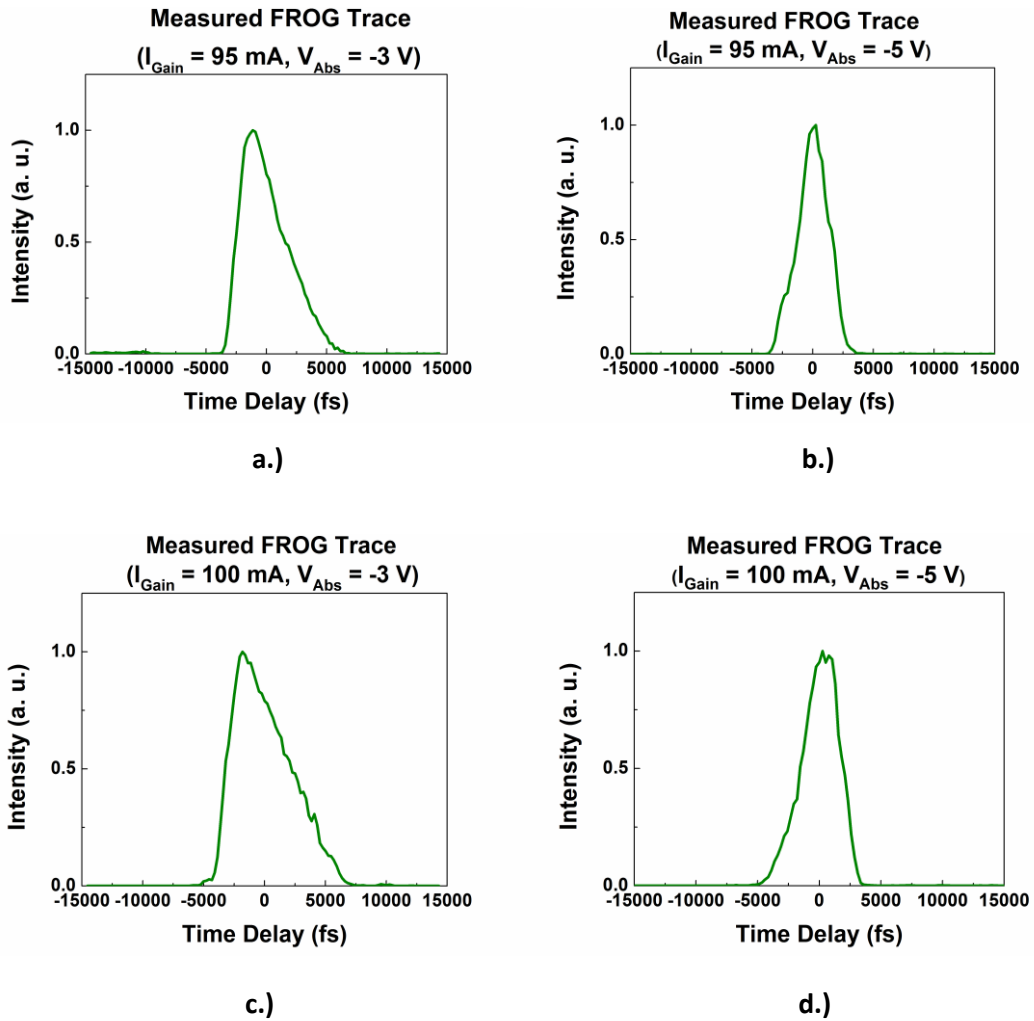
Figure 3-10: *Experimentally measured FROG traces showing the normalized temporal pulse intensity (clockwise from top left):* **a.)** *95 mA gain current, -3V absorber bias* **b.)** *95 mA gain current, -5V absorber bias* **c.)** *100 mA gain current, -3V absorber bias, and* **d.)** *100 mA gain current, -5V absorber bias.*

However, keeping the gain current fixed, when the absorber bias was increased to -5V, the asymmetry of the pulse was observed to flip as seen in Fig. 3-10 b.) Specifically, the trailing edge of the pulse is seen to show a faster decay than the rise time of the leading edge. An identical trend was seen at higher currents, such as the case shown in Figs. 3-10

c.) and d.), where the pulse asymmetry reversal in going from an absorber bias of -3 V to -5 V was observed for a gain current of 100 mA.

Simulation results of the DDE model seeded with physically measured parameters provide an invaluable tool to help understand this trend. Fig. 3-11 shows simulation results for the -5 V absorber bias condition near threshold at 20 °C, with $\alpha_g = \alpha_q = 1.1$ (solid green plots), and $\alpha_g = \alpha_q = 1.6$ (dashed red plots). The switching of pulse asymmetry can be clearly seen in Fig. 3-11 a.), from the green, solid pulse, to the red, dashed pulse.

The reversal in asymmetry may be interpreted as follows. At higher bias voltage, the gain section requires a higher threshold current, so that the higher concentration of injected carriers induces an increase in the linewidth enhancement factor. Combined with the length of the gain section, this results in significant pulse broadening due to dispersion and self-phase modulation as the pulse propagates through the gain section.

Simultaneously, the applied bias on the absorber section has the effect of expediting the sweep-out rate of the photo-generated carriers, leading to a faster recovery time.

A careful comparison of the plots in Fig. 3-11 b.) and c.) reveals the subtle distinguishing features between the two cases.
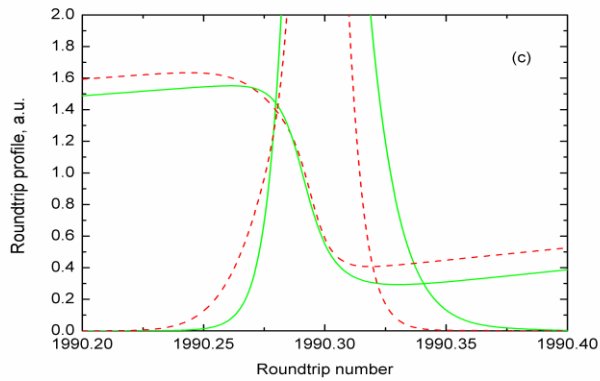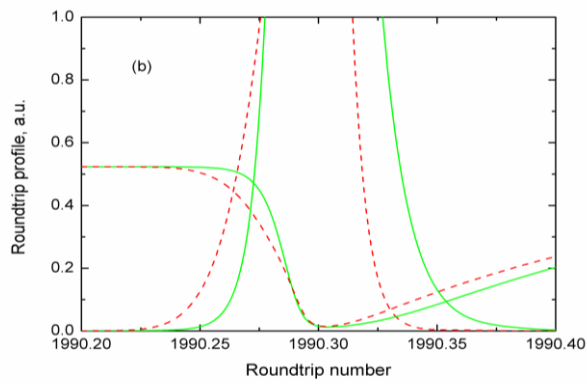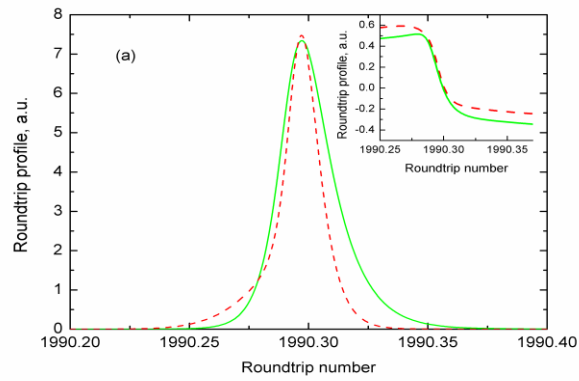
Figure 3-11: *Simulation results for the $T = 20\,^{o}C$, $V_{abs} = -5\ V$ $\alpha_{g,q} = 1.1$ (solid green curves) , $\alpha_{g,q} = 1.6$ (dashed red curves). (a) Temporal pulse profiles (inset shows corresponding net gain profiles), (b) shows the saturable loss profiles and (c) shows the saturable gain profiles, superimposed on the temporal pulse profiles.*

In the first case ($\alpha_g = \alpha_q = 1.1$, solid green curve), the pulse is, relatively speaking, "less broadened" in the gain section, owing to less self-phase modulation due to the relatively lower linewidth enhancement factor. Thus, the pulses exiting the gain section are expected to be narrower in the former case. The steeper leading (rising) edge associated with a narrower pulse causes the absorber to saturate rapidly, as seen from the green curves in Fig. 3-11 b.).

By contrast, in the second case ($\alpha_g = \alpha_q = 1.6$, dashed red curve), a "more broadened" pulse exiting the gain section with a less steep leading edge profile is not able to saturate the absorber quite as fast, so that the absorber saturation is noticeably more gradual than in the former case, as seen from the dashed red curves in Fig. 3-11 b.).

The trailing (falling) edge profile is governed by the absorber dynamics. On inspection of the saturable loss profiles shown in Fig. 3-11 b.), one can observe that the absorber recovery is slightly more rapid for the dashed red plot ($\alpha_g = \alpha_q = 1.6$). Thus, due to the fact that the trailing edge experiences more loss at its tail, it is "better trimmed", so that the pulse has a steeper trailing (falling) edge. The combined effect of the gain and absorber sections is that in the former case ($\alpha_g = \alpha_q = 1.1$), the leading edge of the pulse is steeper, while the trailing edge shows a relatively gradual decay, whereas in the latter case ($\alpha_g = \alpha_q = 1.6$), the leading edge is less steep, the trailing edge is better trimmed, and the asymmetry is reversed.

Pulse asymmetry is a characteristic feature of mode-locked two-section quantum dot lasers [22]. The variation of pulse asymmetry has been studied before in dye lasers [23], and simulated for a microchip laser system [24], and holds promise for solitonic applications such as chirp compensation and pulse compression. It is in such instances

that simulation results of the DDE model seeded with measured parameters can provide an invaluable aid to complement the diagnostic techniques mentioned above.

3.5   Chapter Summary

This chapter served as the first demonstration of how measurements performed on an actual device over a range of operating conditions can be transformed into dimensionless inputs for the DDE model, which can then be used as an extremely powerful tool to gain insight into numerous aspects of the output dynamics of the device.

As an added benefit of deriving equations to transform measured quantities into dimensionless model parameters, a novel and innovative technique to estimate the carrier relaxation ratio of the device from basic gain and loss measurements was shown to provide a viable alternative to conventional pump-probe methods. This is an especially useful method of estimating the carrier relaxation ratio of the device at each operating point, where the objective might be to simulate device output over a wide range of operating conditions.

Results of simulation with measurement-extracted parameters indicated the following for stable, fundamental mode-locking for quantum dot devices:

- Low values of linewidth enhancement factor in the gain and absorber sections at or near threshold.

- Low values of unsaturated gain and absorption (which would suggest operation at higher temperatures).

Simulation results also enabled invaluable insight into sudden and unexpected trends in the output dynamics, such as a sudden flipping of the pulse asymmetry, which are typically obscured by autocorrelation measurements. This nonlinear dynamical trend was

83

confirmed for the first time with FROG measurements on the device, while the model was used to acquire insight into the underlying physical mechanism governing the trend.

In conclusion, this chapter showed numerous instances of how several of the properties unique to QD systems are, in fact, embedded in the parameters extracted from the device, so that the model, in its original form, with no additional equations or parameters, can itself act as a robust and powerful theoretical framework to analyze device dynamics.

In the next chapter, we look at some of the predictive capabilities of the model.

3.6   References for Chapter 3

[1] Raghunathan, R., Crowley, M., Grillot, F., Li, Y., Mee, J. K., Kovanis, V., & Lester, L. F. (2013). Pulse Characterization of Passively Mode-locked Quantum Dot Lasers Using a Delay Differential Equation Model Seeded with Measured Parameters.

[2] Blood, P., Lewis, G. M., Smowton, P. M., Summers, H., Thomson, J., & Lutti, J. (2003). Characterization of semiconductor laser gain media by the segmented contact method. *Selected Topics in Quantum Electronics, IEEE Journal of*, *9*(5), 1275-1282.

[3] Xin, Y. C., Li, Y., Martinez, A., Rotter, T. J., Su, H., Zhang, L., ... & Lester, L. F. (2006). Optical gain and absorption of quantum dots measured using an alternative segmented contact method. *Quantum Electronics, IEEE Journal of*, *42*(7), 725-732.

[4] Raghunathan, R., Crowley, M. T., Grillot, F., Kovanis, V., & Lester, L. F. (2011, October). Direct characterization of carrier relaxation in a passively mode-locked quantum dot laser. In *Photonics Conference (PHO), 2011 IEEE* (pp. 109-110). IEEE.

[5] Bakonyi, Z., Su, H., Onishchukov, G., Lester, L. F., Gray, A. L., Newell, T. C., & Tunnermann, A. (2003). High-gain quantum-dot semiconductor optical amplifier for 1300 nm. *Quantum Electronics, IEEE Journal of*, *39*(11), 1409-1414.

[6] Malins, D. B., Gomez-Iglesias, A., White, S. J., Sibbett, W., Miller, A., & Rafailov, E. U. (2006). Ultrafast electroabsorption dynamics in an InAs quantum dot saturable absorber at 1.3μm *Applied Physics Letters*, *89*(17), 171111-171111.

[7] Cataluna, M. A., Malins, D. B., Gomez-Iglesias, A., Sibbett, W., Miller, A., & Rafailov, E. U. (2010). Temperature dependence of electroabsorption dynamics in an InAs quantum-dot saturable absorber at 1.3 μm and its impact on mode-locked quantum-dot lasers. *Applied Physics Letters*, *97*(12), 121110-121110.

[8] Crowley, M. T., Murrell, D., Patel, N., Breivik, M., Lin, C. Y., Li, Y. & Lester, L. F. (2011). Analytical modeling of the temperature performance of monolithic passively mode-locked quantum dot lasers. *Quantum Electronics, IEEE Journal of*, *47*(8), 1059-1068.

[9] Borri, P., Schneider, S., Langbein, W., & Bimberg, D. (2006). Ultrafast carrier dynamics in InGaAs quantum dot materials and devices. *Journal of Optics A: Pure and Applied Optics*, *8*(4), S33.

[10] Vladimirov, A. G., & Turaev, D. (2005). Model for passive mode locking in semiconductor lasers. *Phys. Rev. A*, *72*(3), 033808.

[11] Vladimirov, A. G., Pimenov, A. S., & Rachinskii, D. (2009). Numerical study of dynamical regimes in a monolithic passively mode-locked semiconductor laser. *Quantum Electronics, IEEE Journal of*, *45*(5), 462-468.

[12] Raghunathan, R., Crowley, M. T., Grillot, F., Mukherjee, S. D., Usechak, N. G., Kovanis, V., & Lester, L. F. (2012, February). Delay differential equation-based modeling of passively mode-locked quantum dot lasers using measured gain and loss spectra. In *SPIE OPTO* (pp. 82551K-82551K). International Society for Optics and Photonics.

[13] Mee, J. K., Crowley, M. T., Patel, N., Murrell, D., Raghunathan, R., Aboketaf, A., ... & Lester, L. F. (2012). A passively mode-locked quantum-dot laser operating over a broad temperature range. *Applied Physics Letters*, *101*(7), 071112-071112.

[14] Mee, J., Crowley, M., Murrell, D., Raghunathan, R., & Lester, L. (2013). Temperature Performance of Monolithic Passively Mode-Locked Quantum Dot Lasers: Experiments and Analytical Modeling.

[15] Mee, J. K., Crowley, M. T., Patel, N., Murrell, D., Raghunathan, R., Aboketaf, A., ... & Lester, L. F. (2012, October). 110° C operation of monolithic quantum dot passively mode-locked lasers. In *Semiconductor Laser Conference (ISLC), 2012 23rd IEEE International* (pp. 68-69). IEEE.

[16] Mee, J. K., Crowley, M. T., Raghunathan, R., Murrell, D., & Lester, L. F. (2013, March). Characteristics of passively mode-locked quantum dot lasers from 20 to 120° C. In *SPIE OPTO* (pp. 86190B-86190B). International Society for Optics and Photonics.

[17] Usechak, N. G., Xin, Y., Lin, C. Y., Lester, L. F., Kane, D. J., & Kovanis, V. (2009). Modeling and direct electric-field measurements of passively mode-locked quantum-dot lasers. *Selected Topics in Quantum Electronics, IEEE Journal of*, *15*(3), 653-660.

[18] Li, Y., Lin, C. Y., Chang, D., Langrock, C., Fejer, M. M., Kane, D. J., & Lester, L. F. (2011, May). Pulse characterization of a passively mode-locked quantum dot

semiconductor laser using FROG and autocorrelation. In *Lasers and Electro-Optics (CLEO), 2011 Conference on* (pp. 1-2). IEEE.

[19] Li, Y., Lester, L. F., Chang, D., Langrock, C., Fejer, M. M., & Kane, D. J. (2013). Characteristics and instabilities of mode-locked quantum-dot diode lasers. *Optics express*, *21*(7), 8007-8017.

[20] Amat-Roldán, I., Cormack, I. G., Loza-Alvarez, P., Gualda, E. J., & Artigas, D. (2004). Ultrashort pulse characterisation with SHG collinear-FROG. *Opt. Express*, *12*(6), 1169-1178.

[21] Yang, S. D., Weiner, A. M., Parameswaran, K. R., & Fejer, M. M. (2005). Ultrasensitive second-harmonic generation frequency-resolved optical gating by aperiodically poled LiNbO3 waveguides at 1.5 μm. *Optics letters*, *30*(16), 2164-2166.

[22] Radziunas, M., Vladimirov, A. G., Viktorov, E. A., Fiol, G., Schmeckebier, H., & Bimberg, D. (2011). Strong pulse asymmetry in quantum-dot mode-locked semiconductor lasers. *Applied Physics Letters*, *98*(3), 031104-031104.

[23] Finch, A., Chen, G., Sleat, W., & Sibbett, W. (1988). Pulse asymmetry in the colliding-pulse mode-locked dye laser. *Journal of Modern Optics*, *35*(3), 345-354.

[24] Kozyreff, G., & Mandel, P. (2001). *Nonlinear aspects of the dynamics induced by dissipative light-matter interaction* (Doctoral dissertation, Doctoral thesis, Université Libre de Bruxelles, 2001. http://www. ulb. ac. be/sciences/ont/theses/Gregory Kozyreff Thesis. pdf).

Chapter 4

Predictive Capabilities of the DDE Model

Chapter 3 explored the analytical capabilities of the extended DDE formalism [1, 2], demonstrating its ability to provide vital insight into certain dynamical trends, typically observed during experimentation as irregular intensity fluctuations, coupled with sudden transitions in the output pulse dynamics. A parameter sensitivity analysis showed the linewidth enhancement factor to have a profound influence on pulse structure (§3.3.2). This was later corroborated in §3.4.2, where the choice of linewidth enhancement factor was seen to determine pulse asymmetry. The ability to be able to understand and control the nonlinear dynamical regimes of operation of a device can be readily seen to be critically important for at least a couple of reasons:

   i.   Dynamical instabilities in semiconductor lasers, arising from device operation in unstable regimes, can be severely detrimental to device performance and in certain cases, even lead to device failure. Thus, the ability to be able to predict (and potentially avoid) unstable regimes in advance is highly desirable.

   ii.   Controllability over the regimes of operation is essential to being able to "steer" a device out of a particular dynamical state of operation, and into another, desired state. This is often the case, for instance, when the device is sought for a bistable operation (such as wavelength-switching) or to switch the output from fundamental to higher –order mode-locking dynamically, while the device is in operation.

The nonlinear delay-formalism of the DDE model provides a natural framework to predict such regimes mathematically, and enables a promising approach for dynamical controllability. To this end, the powerful predictive capabilities of the DDE model are explored in the context of each of the above instances in the present chapter (Chapter 4). Section 4.1 presents commonly-encountered unstable dynamical trends predicted by the model, such as pulse breakup into side lobes and satellite pulses (§4.1.1), and the closely-related dynamics of split-pulsing (§ 4.1.2). Section 4.2 then explores the predictive capabilities of the model for harmonic mode-locking. Conclusions are given in section 4.3.

4.1   Dynamical Instabilities

Dynamical instabilities in semiconductor lasers arising from device operation in unstable regimes can be severely detrimental to device performance [3]. High performance applications such as high bit rate communications systems and optical clocking, rely on the quality and stability of both the output pulse trains, as well as individual pulse structures [4]. Output pulse structure is a signature of whether the regime of operation of a mode-locked laser is stable or unstable [5]. Understanding such parasitic effects is critical to being able to minimize their occurrence. On the other hand, certain applications such as chaos synchronization look to exploit the chaotic dynamics of device output as a way of making data transmission secure [6].

In this section, we study two commonly-encountered dynamical instabilities – pulse break-up leading to the formation of side lobes and satellite pulses, and split-pulsing, observed experimentally in passively mode-locked two section quantum dot lasers –

using the DDE model. It may be recalled from Chapter 2, that in constraining the parameter space of the model to measured values, we were left with the linewidth enhancement factors in the gain and absorber sections, as the two free parameters. The DDE model predicts that the most stable operating condition for pulse formation is when the gain section linewidth enhancement factor (α_g) is set equal to the absorber section linewidth enhancement factor (α_q). In [7] and [8], detailed analyses of dynamical regimes using bifurcation diagrams showed that the shortest mode-locked pulses with the highest peak power are achieved for $\alpha_g = \alpha_q$. Furthermore, the effect of increasing α_g above α_q is seen to have a severely detrimental influence on pulse structure, causing a rapid degradation of the output to chaotic fluctuations.

The aforementioned scenario is of great practical interest, as it enables a study of dynamical instabilities in the device output. Consequently, the approach in the following section follows the approach of Chapter 3, with the notable exception of $\alpha_g \neq \alpha_q$.

4.1.1 Side Lobes and Satellite Pulses

Side lobes and satellite pulses are both observed fairly routinely in experiment, as shown in Fig. 4-1 a.) and b.). The data was acquired experimentally using a high speed oscilloscope (140 GHz Tektronix DSA 8200 Digital Serial Analyzer).
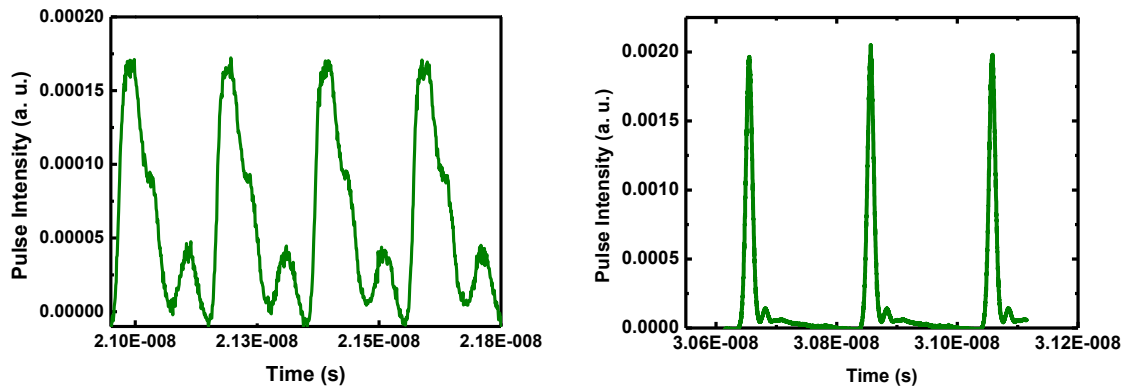
Figure 4-1: *High Speed Oscilloscope output for **a.)** 0 V absorber bias, 100 mA gain section pump current, and b.) - 4.5 V absorber bias, 135 mA pump current – the second pulse is much weaker compared to the first, and appears as a satellite pulse on the trailing edge.*

As seen from Fig. 4-1a.), at a 0 V absorber bias, the satellite pulse following the main pulse is much stronger than for the - 4.5 V absorber bias condition shown in Fig. 4-1b.), where the satellite pulse is suppressed and appears as a slight trailing edge instability. Table 4-1 shows simulation parameters extracted from measured values at different operating conditions.

Table 4-1a: *Simulation parameters over bias voltage at 20 °C and 60 °C*

Parameter	T = 20 °C 0V	T = 60 °C 0V	T = 60 °C -3V
T	3.23	4.17	7.10
G(0)	3.33	2.89	3.27
Q(0)	2.33	2.20	2.43
α_g	2.0	2.0	2.0
α_q	0.5	0.5	0.5
s	2.68	4.83	9.75
Γ	0.13	0.08	0.04
γ	29.14	18.0	13.24
κ	0.304	0.304	0.304

The device simulated here is the same as the device simulated in Chapter 3 (ZLG967E, parameters extracted on Wafer 967). It may be noted form the values of γ in each case, that the device simulated in this case has a relatively narrow gain-bandwidth. Fig. 4-2a shows the results of simulation for the parameter set in the first column of Table 4-1a.
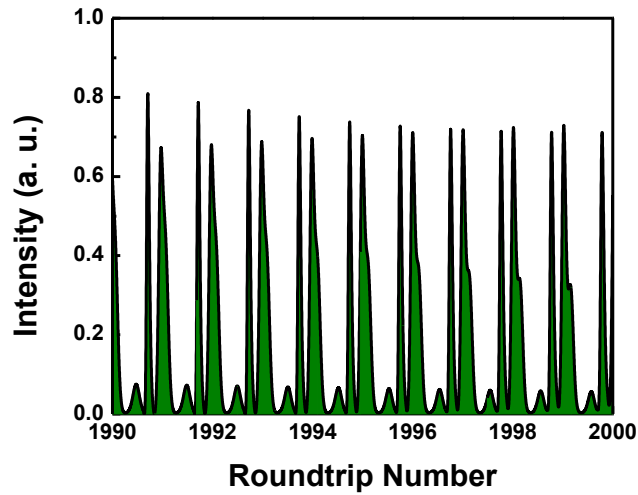
Figure 4-2a: *Highly unstable regime predicted for the T = 20 ℃, V_{abs} = 0V, α_g = 2.0, α_q = 0.5 case. Model predicts a combination of pulse-breakup and side lobes.*

A highly unstable regime of operation is predicted in this case, involving a combination of pulse- breakup seen from the two higher intensity lobes, and a smaller side lobe on the leading edge.
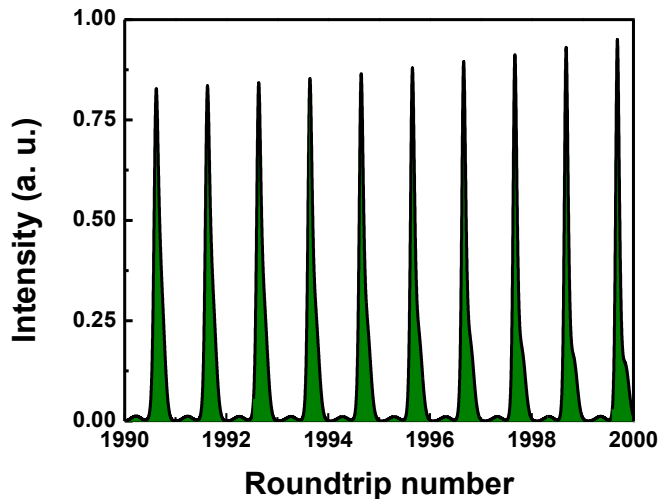
Figure 4-2b: *Simulation result for the T = 60 ℃, V_{abs} = 0V, α_g = 2.0, α_q = 0.5 case. Model predicts a small side lobe on the leading edge.*

Mode-locking instabilities are predicted to be somewhat more "tempered" at an elevated temperature for the same absorber bias condition of 0V, as seen from Fig. 4-2b. In this case, a very small side lobe is seen to appear on the leading edge.

Finally, the application of a moderate bias at elevated temperature is predicted to generate satellite pulses on the trailing edge, with energy exchange-coupling between the main pulse and the satellite pulse as seen from Fig. 4-2c.
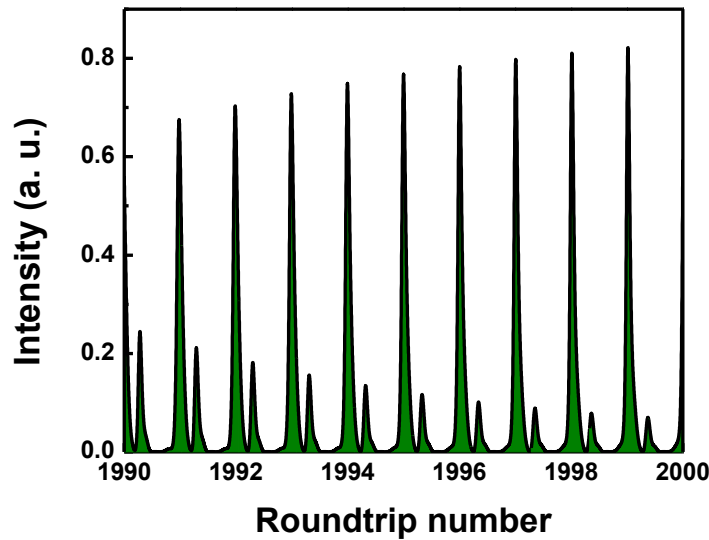
Figure 4-2c: Simulation result for the $T = 60\,°C$, $V_{abs} = -3V$, $\alpha_g = 2.0$, $\alpha_q = 0.5$ case. Model

predicts a satellite pulse on the trailing edge, with energy-exchange with the main pulse.

Thus, for low values of the spectral filtering coefficient representative of devices with a narrow gain-bandwidth, the model predicts that the output pulses are prone to pulse breakup and leading or trailing edge satellite pulses for a difference in the linewidth enhancement parameters between the gain and absorber sections.

4.1.2   Split-Pulsing Dynamics [9]

This dynamical trend was observed on the output of a two-section, passively mode locked quantum dot laser with an optimized six-stack InAs Dots-in-a-Well (DWELL) active region similar to the device simulated in §4.1.1, but with a wider gain-bandwidth. Output pulses were observed on a high speed sampling oscilloscope (140 GHz Tektronix DSA 8200 Digital Serial Analyzer). The critical advantage of using this oscilloscope is the ability to capture pulse train dynamics over timescales on the order of nanoseconds, as well as individual pulse structures.

For an absorber bias of -3V and for gain currents in the range 90 mA $\leq I_{gain} \leq$ 115 mA, a split-pulsing output as shown in Fig. 4-3 was observed, wherein the individual pulse structures are characterized by two split lobes, varying in relative intensity over each round trip.
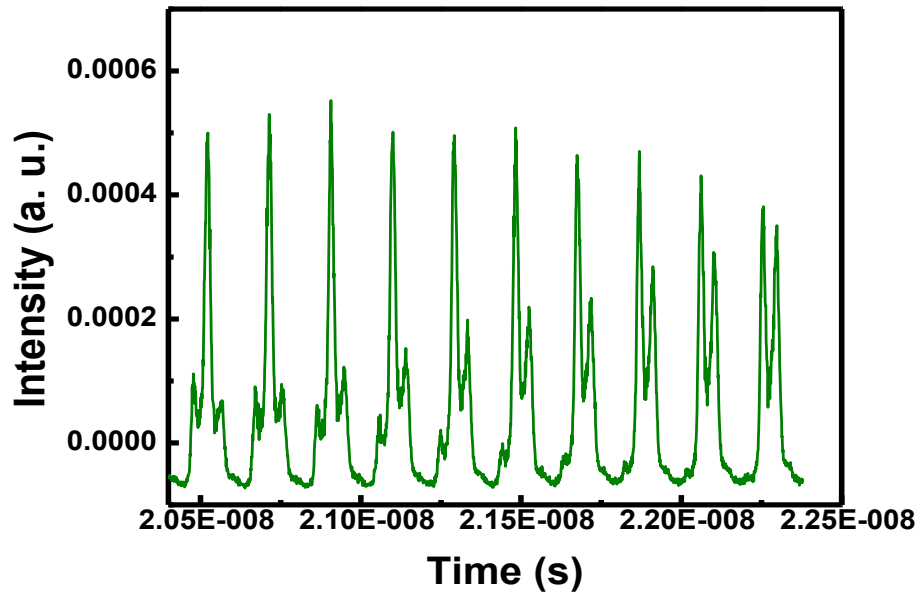
Figure 4-3: *The split-pulsing dynamic, experimentally measured on a device similar to the one simulated in the previous section, but with a larger gain-bandwidth.*

Since the device used in the experiment had a similar layer structure as the device used previously (the only differences being the 6-stack layer structure and a wider gain-bandwidth), the split-pulsing dynamic was simulated with a nearly identical parameter set to the values shown in the first column of Table 4-1a, shown below in Table 4-1b.

Table 4-1b: *Simulation parameters for the split-pulsing dynamic*

Parameter	0 V
T	3.226
g_0	0.4329
q_0	0.871
α_g	2.0
α_q	0.5
s	2.676
Γ	0.13
γ	53.3
κ	0.304

The wider gain dispersion was modeled with a larger value of the spectral filtering coefficient, representative of a larger number of modes participating in the mode-locking process, as seen from Table 4-1b.

Fig. 4-4 shows the simulation results obtained using the parameters listed in Table 4-1b.
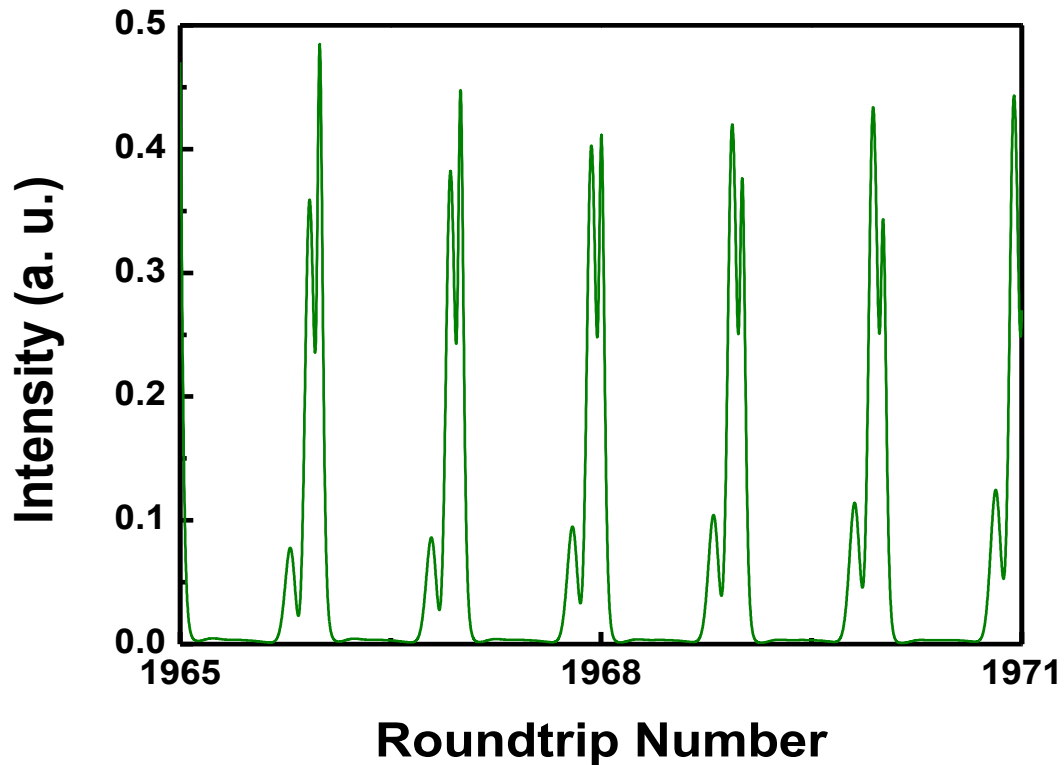
Figure 4-4: *Simulation results of the split-pulsing dynamic using the DDE Model.*

Pulse-splitting in a passively mode-locked laser has been previously attributed to phase modulation-instability arising from the effective feedback of the medium on the circulating pulse [10], as a result of the response of the medium to the incident pulse, which perturbs the latter. In the DDE model derived in [7], it is evident that the effect of feedback due to the gain and absorber media is embedded in the first equation of the system, wherein the evolution of optical field at the present time τ is governed by the optical field, saturable gain and saturable absorption a time $(\tau - T)$, where T represents a delay parameter.

A sensitivity-analysis of the simulation result shown in Fig. 4-4 revealed a key finding –

the split-pulsing effect is extremely sensitive to the difference in the linewidth

enhancement factors (LEFs) of the gain and absorber media. Considering that the LEFs

appear only in the complex exponential phase term in the first equation of the DDE

model, it is reasonable to expect phase modulation instabilities when they are subjected to

a perturbation. The effect of feedback of the medium on pulse structure can be clearly

seen in Fig. 4-5a and b.
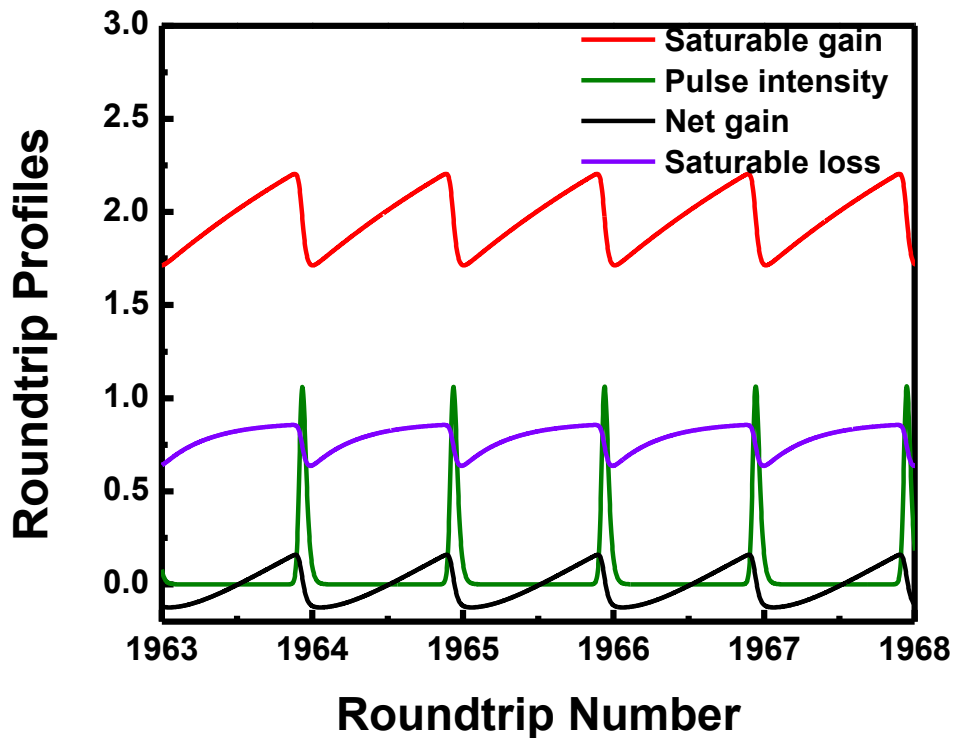
Figure 4-5a: *Roundtrip pulse dynamics for $\alpha_g = \alpha_q = 0.5$.*

In Fig. 4-5a, for the case of equal LEFs in the gain and absorber media, pulse formation

follows the usual dynamics, whereby a strong single pulse saturates the gain and absorber

media such that a brief window of net gain allows for the pulse to be sustained. However,

in the case of the unequal LEFs, the initial split lobe appears as a weak instability on the

leading edge, caused by the fact that as the leading edge of the pulse enters the absorber medium, it sees a considerably lower LEF compared to the part of the pulse still in the gain medium. The response of the gain and the absorber media to this weak pulse is a slowing down of the gain and absorber saturation times, as seen from the increasingly gradual dip in the saturable gain and absorber profiles in Fig. 4-5b.
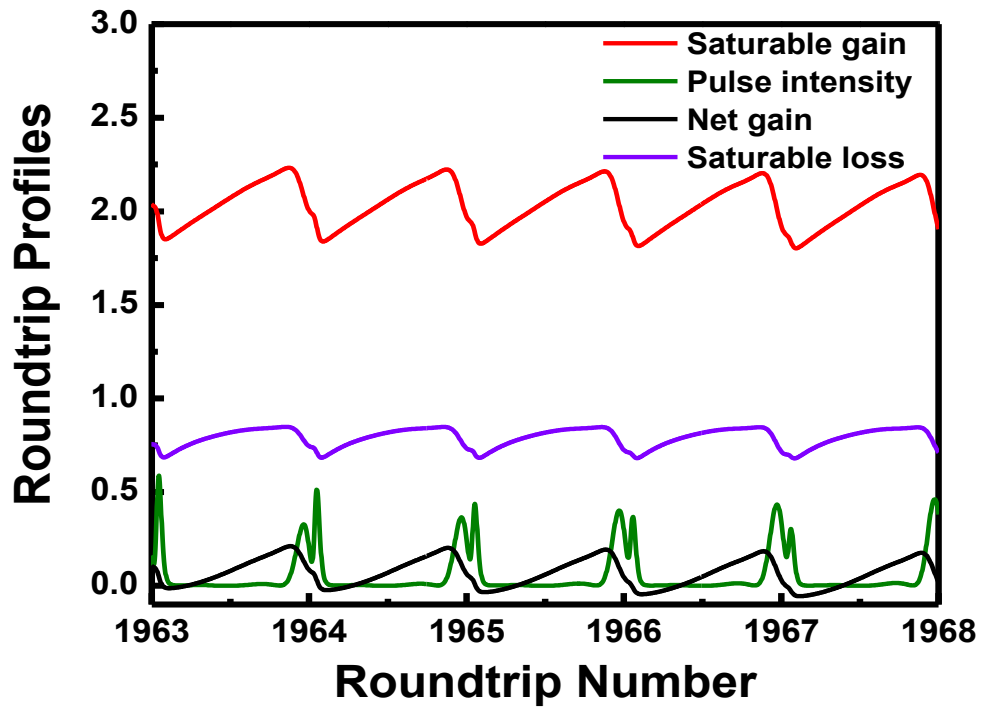
Figure 4-5b: *Roundtrip pulse dynamics for $\alpha_g = 2$, $\alpha_q = 0.5$.*

The part of the pulse following this initial lobe is narrower and more intense, so that it hastens the saturation and recovery profiles of the saturable gain and absorption. Over several round trips, the weak, initial lobe sees gain for a longer time than the main lobe following it, and is amplified more with each round trip. Conversely, the initially dominant main lobe sees less gain and more loss with each round trip, and is progressively attenuated. The end result is that the feedback of the medium amplifies the

weaker lobe and attenuates the initially stronger lobe to the point where the initially dominant lobe is completely suppressed, by which time a new leading edge instability (weak lobe) is seen to form, and the process repeats.

A similar analysis can be applied to each of the dynamical instabilities seen in § 4.1.1, where in each case, the degradation in pulse structure can be interpreted from a careful inspection of the round trip gain and loss profiles, directly obtained from DDE simulations for that case. From the results obtained in § 4.1.1 and § 4.1.2, it may be inferred that the DDE model predicts the following:

i. A difference in α - parameter values in the gain and absorber sections will quickly lead to degradation in the output pulse structure.

ii. This degradation is especially pronounced for pulses emitted by devices with a narrow gain-bandwidth operating at lower temperatures, where the output can be prone to a combination of effects such as pulse breakup and side-lobe formation. And while such instabilities are predicted to be less drastic at elevated temperatures, they are still significant.

iii. For devices with a wide gain dispersion profile, the model predicts the closely-related dynamic of split-pulsing, where the split lobes of each output pulse exhibit energy exchange-coupling. This prediction was confirmed with high speed oscilloscope measurements of a device fabricated with a wide gain-dispersion profile.

4.2   Toward Higher Repetition Rates – Dynamical Transitions to Harmonic Mode-Locked (HML) Regimes

The focus of the last section was the dynamical instabilities arising from a difference of linewidth enhancement factors seen by the pulse as it propagates through the gain and absorber media. In the remainder of this chapter, the powerful predictive capabilities of the model are shown to offer a promising pathway toward the generation of higher repetition rates by leveraging the dynamics of pulse-splitting and eventual breakup into satellite pulses, under the right conditions, to enable a dynamical switching to stable higher-order mode-locking regimes.

4.2.1   Achieving Higher Repetition Rates with Harmonic Mode-Locking

Quantum dot mode-locked lasers have generated considerable interest in recent years as promising sources of low energy, low jitter, stable pulse trains ([11], [12]) for precision applications such as high bit rate optical communications ([4],[13], [14]) and clocking ([15], [16]) where identical pulses with a regular shape are sought at a desired repetition rate. The typically stringent (and often competing) performance requirements for such applications include high repetition rates on the order of tens of GHz, peak powers on the order of a few Watts and sub-10 ps pulse widths, all while maintaining stable pulse quality over variable operating conditions. To this end, recent work in our group and others has shown that higher repetition rates can be achieved without compromising on the other performance metrics aforementioned by implementing techniques such as making the device reconfigurable [17] (wherein, the position of the saturable absorber is varied within the cavity) and harmonic mode-locking using the double-interval technique

[18] (wherein two saturable absorber sections positioned at specific locations in a multi-section device are used to stimulate a specific higher order repetition rate).

A key motivating factor in the quest for such techniques are the limitations inherent to simple, two-section QDMLL devices, such as the highest fundamental repetition rate achievable being limited by the cavity length (which, in turn, is limited by the relatively low maximum attainable optical gain that is characteristic of QD structures). The standard approach toward the design, fabrication and characterization of such devices involves an extensive cycle of iterative design and testing, where the objective is to find a configuration(s) that is acceptable for the target application. In order to make this procedure more streamlined and efficient, a robust predictive modeling capability is highly desirable, since such a tool will firstly enable experimentation guided by theoretical predictions, as opposed to a trial-and-error approach. Secondly, as mentioned at the beginning of this chapter, numerical simulations allow a detailed study of how the nonlinear dynamics of the output are impacted by a variation of the input parameters, information that is critical to achieving controllability over device performance.

The objective of this section is to build on previous efforts to better understand the pulse characteristics and mode locking stability of passively mode-locked QDMLLs ([19],[20]), with the objective of going a step further in providing a predictive guideline toward achieving higher pulse repetition rates. As in previous sections, the DDE model seeded with parameters measured on an actual device is used to simulate the output mode locking regimes as input parameters are varied. The model parameters corresponding to each regime are then mapped to externally controllable parameters, so that the regions of fundamental and harmonic mode locking can be represented as a function of parameters

that can be varied instantaneously, while the device is in operation. In so doing, we develop a scheme to interactively switch the device to a higher or lower output pulse repetition rate, using just the external (electrical) bias controls [21]. The approach offers a viable technique to achieving variable pulse repetition rates, without the need to re-engineer the device with additional sections.

Owing to the consideration that the most stable pulses are predicted by the DDE model to occur when $\alpha_g = \alpha_q$, the approach in this section is to work under this assumption. The objective then is to find a control parameter that can be varied externally, using the electrical bias and temperature controls. This would then enable the experimenter to dynamically switch the device from one regime of operation to another. This criterion is fulfilled by the parameter m in equations (2-49) and (2-50), from where we recall, $m = (q_0/g_0)$. Thus, with m as the control parameter, the DDE model is employed to simulate and study the dynamical regimes of mode-locked operation of the device. The mathematical ranges of the parameter m corresponding to these regimes are then mapped to externally-controllable parameters such as gain current and absorber bias voltage. Using this approach, a map indicating the approximate regions corresponding to fundamental and harmonically mode locked operation is constructed as a function of gain current and absorber bias voltage. This is shown to be a highly useful method of getting a sense of the highest repetition rates achievable in principle with a simple, two-section device, and provides a guideline toward achieving higher repetition rates by simply adjusting external biasing conditions instantaneously while the device is in operation, as opposed to re-engineering the device with additional passive or saturable absorber sections. The general approach could potentially aid the development of numerical

modeling techniques aimed at providing a systematic guideline geared toward developing

microwave and RF photonic sources for THz applications.

Since the device simulated in this study is the same as the one used in Chapter 3

(ZLG967E), the simulation parameters are drawn from Table 3-3, which is given below

for easy reference.

Table 4-2: *Simulation Parameters over bias voltage for device under study at 20 C (Wafer*

ZLG967).

Parameter	0 V	-3 V	-5V
T	3.23	5.00	6.67
G(0)	3.33	4.18	4.18
Q(0)	2.33	3.20	4.55
α_g	0.1	0.2	0.5
α_q	0.1	0.2	0.5
s	2.68	4.65	6.90
Γ	0.13	0.08	0.08
γ	29.14	39.15	41.10
κ	0.55	0.55	0.55

Again, the parameter values measured/extracted as discussed above were used as initial conditions for the simulations. Steady state solutions to the system of equations defining the model (equations (2-31) - (2-33)) were then found by direct numerical integration over two thousand round trip times to allow transients to settle. By varying the pre-factor *m* in equation (2-50), different regimes of mode locked operation were predicted, as seen in the following.

Fig. 4-6a shows the steady state output of the system of equations in (2-31)-(2-33), for the operating condition of T = 20°C and a 0V absorber bias voltage (simulation parameters listed in the first column of Table 4-2), for various values of the ratio $(1/m)$ of unsaturated gain to unsaturated absorption.

As seen from Fig. 4-6a, simulations predict the onset of pulse formation for $(g_0/q_0) \approx (1/8)$. Then, as the ratio of (g_0/q_0) is increased, stable, fundamental mode locking is maintained and the pulses are predicted to become more intense. Next, following a very brief interval of instability in the fundamental mode-locking regime immediately after $(g_0/q_0) = (7/8)$ (characterized by pulses of variable intensity and pulse width), the device switches to stable, second harmonic mode-locking, whereby two pulses are predicted per round trip.

As the ratio (g_0/q_0) is increased past 1, the mode-locking is predicted to degrade, so that the device shows unstable mode-locking initially (with pulses of variable intensity and pulse width), and eventually transitions to chaotic behavior.
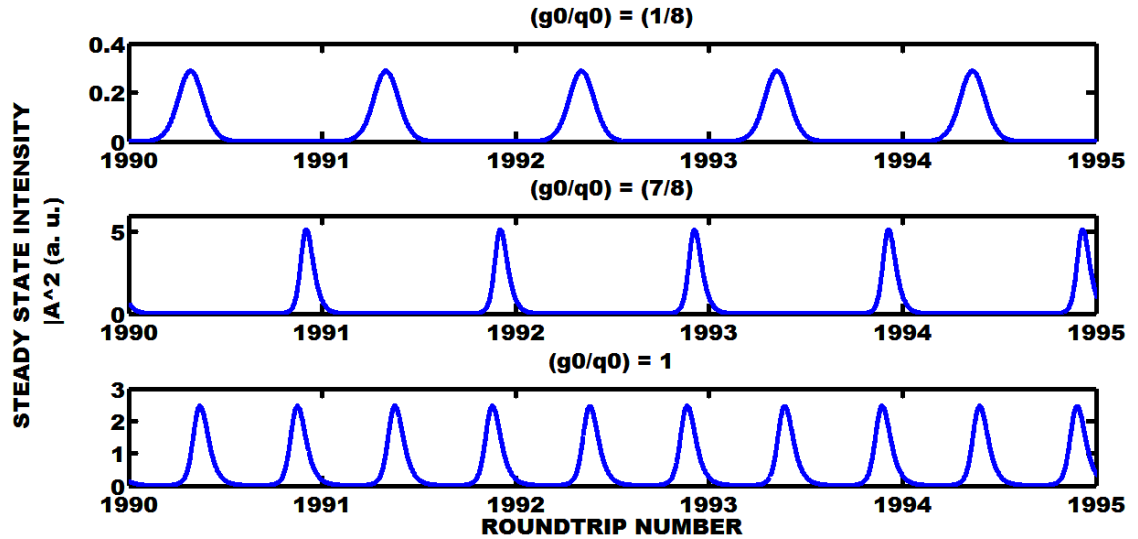
Figure 4-6a: *Steady state mode locking regimes simulated at 20 ˚C for 0V absorber bias, i.)*
fundamental ML for (g_0/q_0) = (1/8), ii.) fundamental ML for (g_0/q_0) = (7/8) and, iii.) 2ⁿᵈ order ML
for (g_0/q_0) = 1.

Thus, the simulation results showed that the device exhibits stable, fundamental mode-
locking in the range $(1/8) \leq (g_0/q_0) \leq (7/8)$, past which the device transitions to a pulse-
doubling regime. No further higher-order mode-locking regimes were found.

Fig. 4-6b shows simulation results for an absorber bias voltage of -3V (simulation
parameters listed in the second column of Table 4-2). In this case, not only does the
model predict a fundamental mode locking regime for $(1/8) \leq (g_0/q_0) \leq (1/2)$, a two-pulse
regime for $(1/2) < (g_0/q_0) \leq (7/8)$, but in addition, a three-pulse mode-locked regime of
operation for $(7/8) < (g_0/q_0) \leq 1$. Similar to the case for a 0V absorber bias, the mode-
locking was predicted to degrade as the ratio (g_0/q_0) was increased past 1, giving way to a
chaotic output.
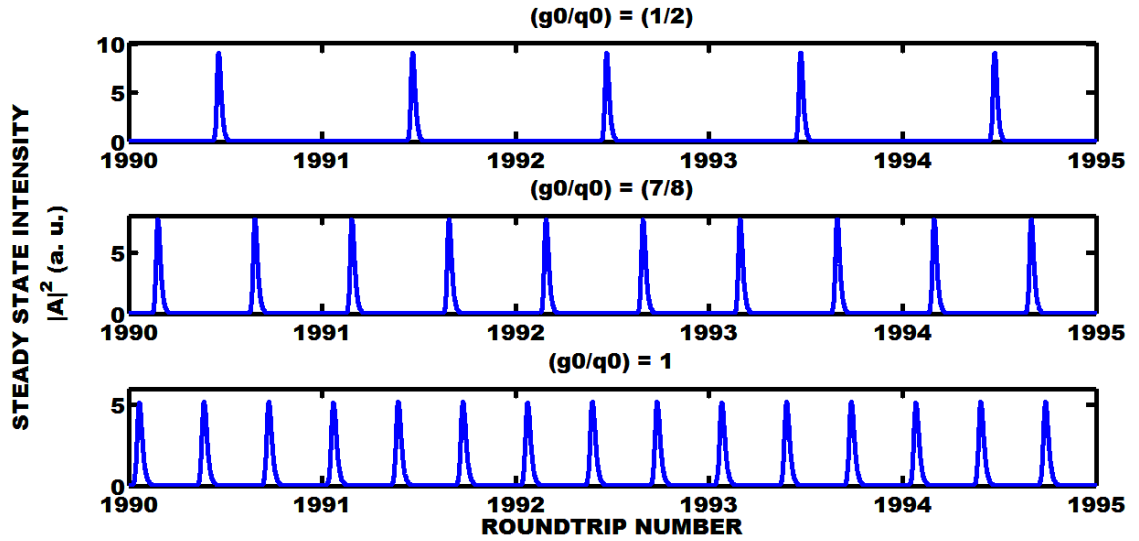
Figure 4-6b: *Steady state mode locking regimes simulated at 20 ˚C for -3V absorber bias, i.) fundamental ML for (g_0/q_0) = (1/2), ii.) 2nd order ML for (g_0/q_0) = (7/8) and, iii.) 3rd order ML for (g_0/q_0) = 1.*

Finally, as seen from Fig. 4-6c, the nonlinear dynamics of the device output shows an even greater range of operational regimes in its progression from fundamental mode-locking ($(1/8) \leq (g_0/q_0) < (5/8)$) to pulse-doubling ($(5/8) \leq (g_0/q_0) < (3/4)$) to pulse-tripling ($(3/4) \leq (g_0/q_0) < (15/16)$) to pulse-quadrupling ($(15/16) \leq (g_0/q_0) \leq 1$), for an applied absorber bias of -5V (simulation parameters listed in the third column of Table 4-2).
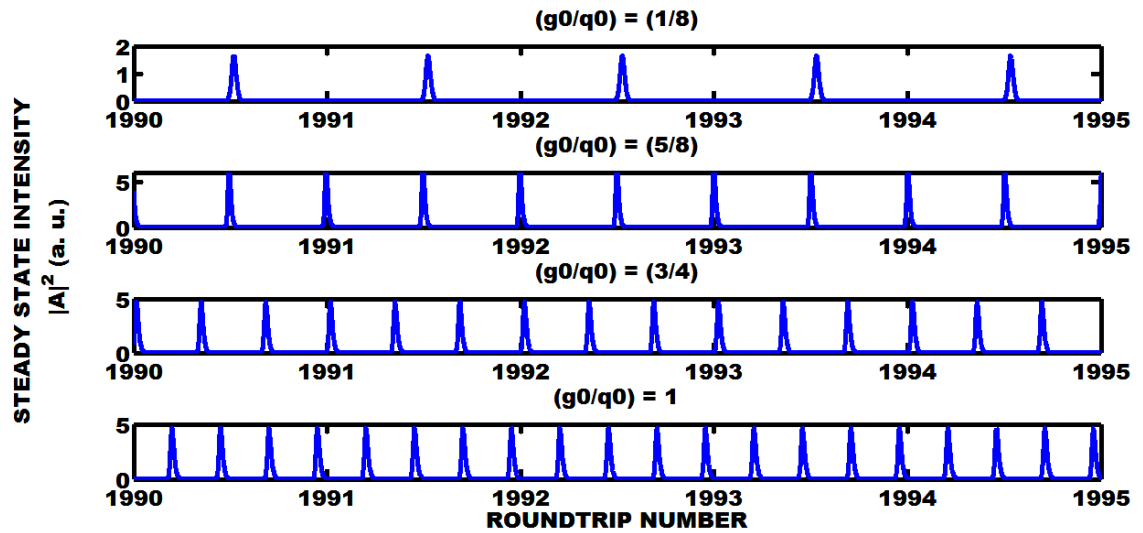
Figure 4-6c: *Steady state mode locking regimes simulated at 20 ˚C for -5V absorber bias, i.)*

fundamental ML for (g_0/q_0) = (1/8), ii.) 2nd order ML for (g_0/q_0) = (5/8), iii.) 3rd order ML for

(g_0/q_0) = (3/4), and iv.) 4th order ML for (g_0/q_0) = 1.

In this case, as the ratio (g_0/q_0) was increased past 1, an unstable 5-pulse per round trip state was predicted in the range $1 < (g_0/q_0) < 1.3$. For $(g_0/q_0) \geq 1.3$, the output was predicted to be chaotic.

Table 4-3 summarizes the results obtained in Fig. 4-6a-c.

Table 4-3: *Predicted ranges of (g_0/q_0) for various mode locking regimes*

Absorber Bias (V)	Range of (g_0/q_0)			
	Fundamental Mode-Locking Regime	Pulse-Doubling Regime	Pulse-Tripling Regime	Pulse-Quadrupling Regime
0	$(1/8) \leq (g_0/q_0) \leq (7/8)$	$(7/8) \leq (g_0/q_0) < 1$	*Not Predicted*	*Not Predicted*
-3	$(1/8) \leq (g_0/q_0) \leq (1/2)$	$(1/2) < (g_0/q_0) \leq (7/8)$	$(7/8) < (g_0/q_0) \leq 1$	*Not Predicted*
-5	$(1/8) \leq (g_0/q_0) < (5/8)$	$(5/8) \leq (g_0/q_0) < (3/4)$	$(3/4) \leq (g_0/q_0) < (15/16)$	$(15/16) \leq (g_0/q_0) \leq 1$

The ranges predicted above in Table 4-3 for the ratio of dimensionless unsaturated gain (g_0) to dimensionless unsaturated absorption (q_0) can be mapped to externally-controllable biasing parameters (gain section pump current and absorber bias voltage) as follows.

From equation (2-50) in Chapter 2,

$$\Gamma = \left(\frac{Q}{mGs} \right) \Rightarrow \left(\frac{1}{m} \right) = \left(\frac{\Gamma Gs}{Q} \right) = \left(\frac{\Gamma G}{Q/s} \right) = \left(\frac{g_0}{q_0} \right)$$

$$(2\text{-}50)$$

Consider any specific range for the ratio (g_0/q_0), for instance, the range for which pulse-quadrupling is predicted for the -5V bias condition in Table 4-3, so that $(15/16) \leq (g_0/q_0) \leq 1$.

Using equation (2-50), this range can be expressed as follows:

$$\left(15/16\right) \leq \left(g_0/q_0\right) \leq 1 \Rightarrow \left(\frac{15}{16}\right) \leq \left(\frac{\Gamma Gs}{Q}\right) \leq 1$$

$$\left(\frac{15Q}{16\Gamma}\right) \leq Gs \leq \left(\frac{Q}{\Gamma}\right)$$

(4-1)

Re-expressing the inequality as shown in (4-1) yields the range of pump currents at a given absorber bias condition and temperature for which a particular mode locking regime is predicted, given that the saturable gain G and saturation parameter s are both functions of pump current density, extracted directly from modal gain characteristics such as those presented in [19]. Using this approach, the following ranges of pump current are calculated corresponding to the ranges obtained in Table 4-3:

Table 4-4: *Predicted ranges of pump current (I_{gain}) for various mode locking regimes*

Absorber Bias (V)	Range of I_{gain}			
	Fundamental Mode-Locking Regime	Pulse-Doubling Regime	Pulse-Tripling Regime	Pulse-Quadrupling Regime
0	$58mA \leq I_{gain} \leq 105mA$	$105mA < I_{gain} \leq 110mA$	*Not Predicted*	*Not Predicted*
-3	$72mA \leq I_{gain} \leq 113mA$	$113mA < I_{gain} \leq 136mA$	$136mA < I_{gain} \leq 140mA$	*Not Predicted*
-5	$84mA \leq I_{gain} \leq 140mA$	$140mA < I_{gain} \leq 148mA$	$148mA < I_{gain} \leq 157mA$	$157mA < I_{gain} \leq 160mA$

The ranges shown in Table 4-4 can be represented as a map showing the approximate regions predicted for each mode-locking regime, as a function of absorber bias vs gain current:
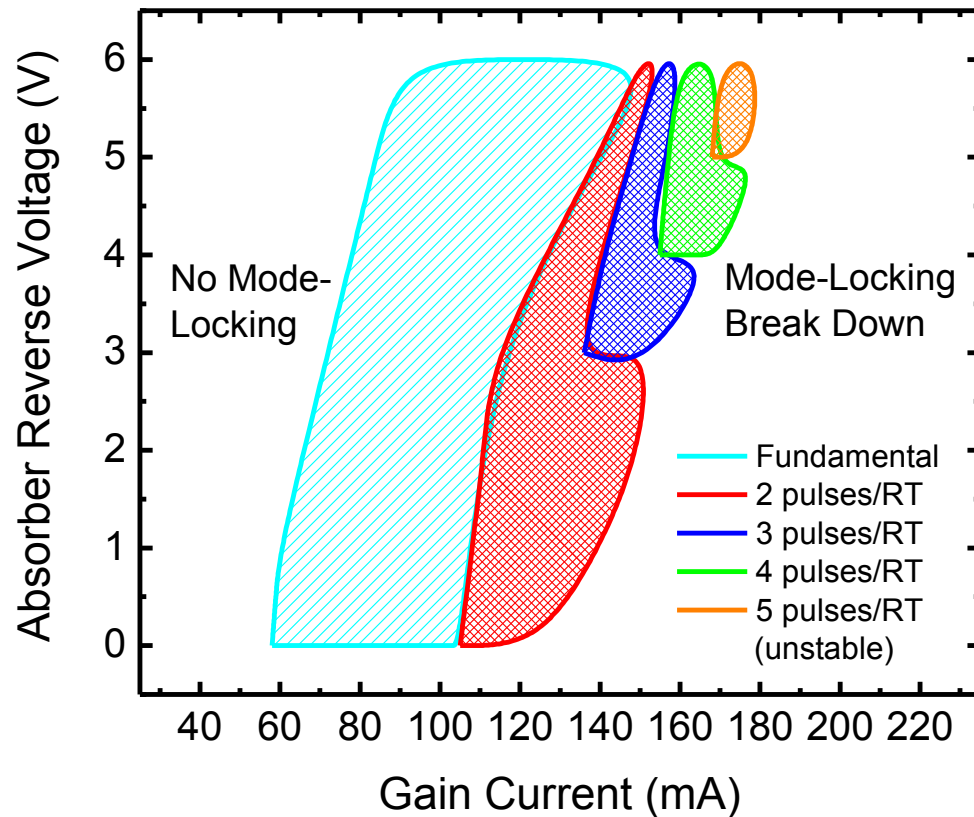
Figure 4-7: *Predicted regions of fundamental and harmonic mode locking regimes as a function*

of electrical biasing parameters.

The practical utility of such a map is evident – the experimenter could simply pick an operating point on the map, lying within a desired regime of operation and bias the device accordingly to achieve a target pulse repetition rate. Following this objective, the device was biased to experimentally achieve the harmonic mode-locking (HML) regimes predicted in Fig. 4-7. As can be seen clearly from the map, the model predicts a pulse-doubling regime for all bias voltages, and a pulse-tripling regime between an absorber bias of -3 V and -5 V. Several instances of two pulses per round trip were observed experimentally for an applied absorber bias with pump currents above 100 mA, although

the second pulse typically appeared as a much weaker "satellite" pulse following the tail of the first (strong) pulse, such as the example seen in the high speed oscilloscope measurement for this device earlier in this chapter in Fig. 4-1b, recorded for a gain current of 135 mA and absorber bias of - 4.5 V.

Three and four pulses per round trip regimes were not observed for this device. Instead, as the bias voltage was increased for above threshold pump currents, the output pulse shape was observed to exhibit unexpected dynamical trends, such as a reversal of the pulse asymmetry, whereby, the leading edge of the pulse displayed a slower rise time compared to the trailing edge of the pulse, which showed a considerably faster decay. This dynamical trend was discussed earlier in Chapter 3 (§ 3.4.2).

However, the broad trends predicted by the map generated from simulation results in Fig. 4-7 served as a useful guide for other devices with a similar epitaxial structure. Consider, for instance, the following results, obtained with a 6-stack device with a similar epitaxial-structure, 5 μm ridge waveguide and 7 mm gain/1 mm absorber section. The output pulse dynamics were captured using high speed oscilloscope measurements.

The map in Fig. 4-7 predicts that at low absorber bias voltages, increasing the pump current past 100 mA should result in a transition from fundamental to second harmonic mode locking. For the device under study (ZLG788AH05), this trend is experimentally confirmed in the high speed oscilloscope traces shown in Fig. 4-8 a.)-c.), where for a constant absorber bias voltage of 0 V, increasing the pump current from 75 mA (Fig. 4-8a.)) to 100 mA (Fig. 4-8b.)) shows the appearance of a second, weaker pulse following the main pulse in each round trip. A further increase of pump current to 125 mA causes the appearance of a two-pulse state, where alternate pulses are identical (Fig. 4-8c.)).
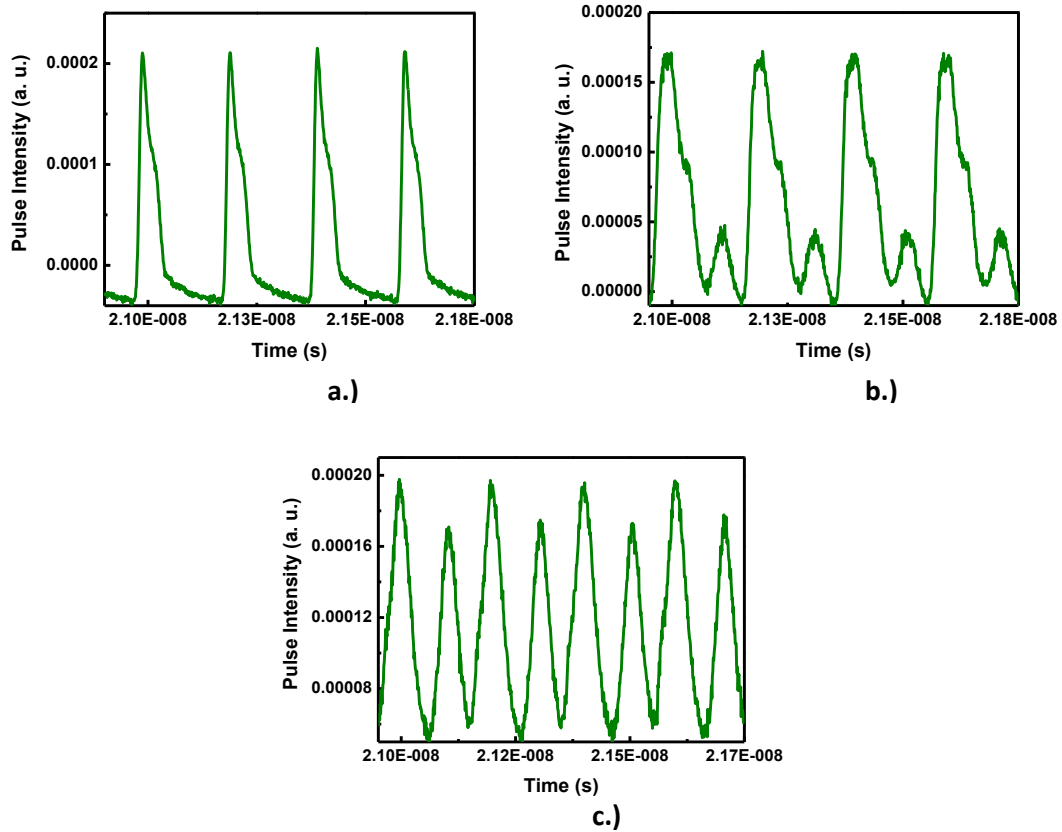
Figure 4-8: *Output pulse dynamics for Device ZLG788AH05 (L_{abs} = 1 mm) constant absorber*

*bias of 0 V for **a.)** I_{gain} = 75 mA **b.)** I_{gain} = 100 mA, and **c.)** I_{gain} = 125 mA.*

As is evident from the measured output data, the critical advantage of using this high speed sampling oscilloscope is the ability to capture output pulse train dynamics on the order of nanosecond timescales, as well as the individual pulse shapes comprising the pulse trains.

Further, the map predicts that for currents above 105 mA, if the absorber bias voltage is increased for a fixed value of pump current, the device should produce two pulses per round trip for low and moderate bias voltages ranging from 0 to -3 V, and switch to fundamental mode-locked operation for stronger bias voltages ranging from -4 to -6 V.

In this case, the device tested experimentally was identical to the previous device, except for a slightly higher gain-to-absorber length ratio (Device ZLG788AH03, L_g = 7.2 mm, L_a = 0.8 mm).
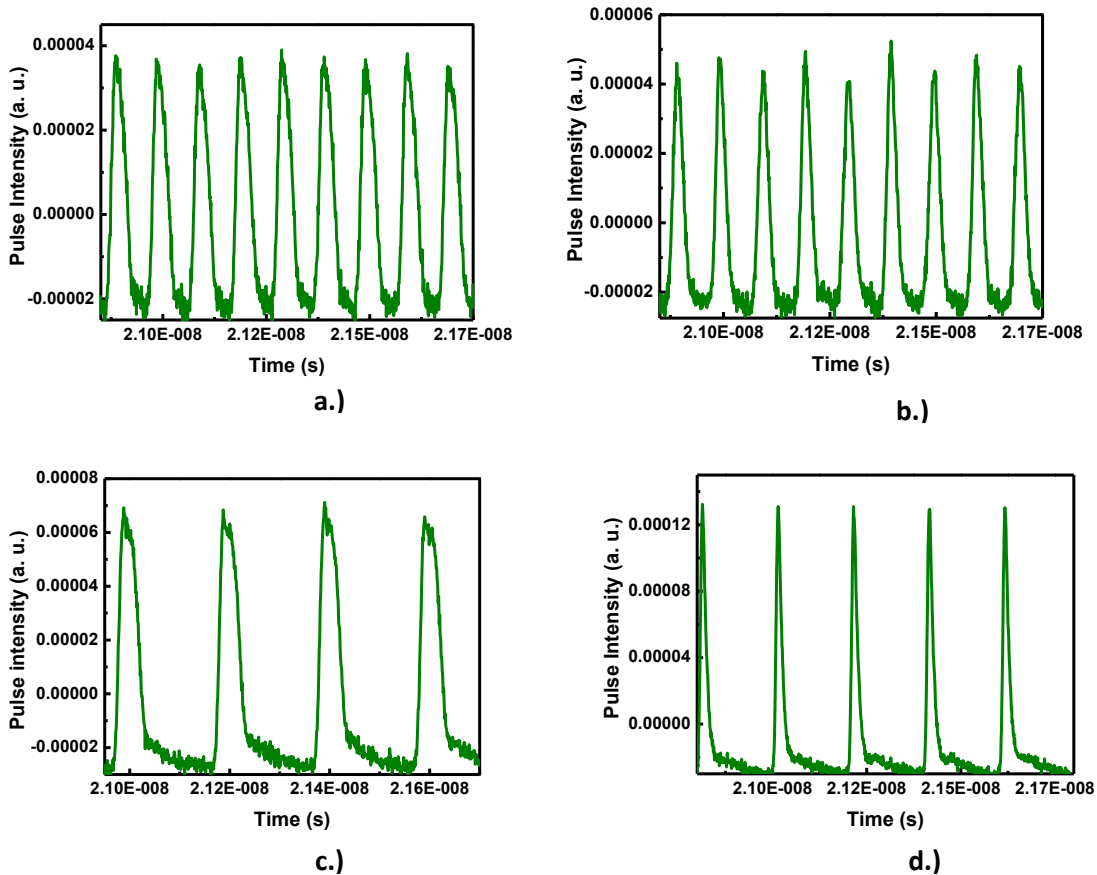
Figure 4-9: *Output pulse dynamics for Device ZLG788AH03 (L_{abs} = 0.8 mm) a constant gain current of 100 mA, with,* **a.)** V_{abs} = 0 V **b.)** V_{abs} = -2 V, *and* **c.)** V_{abs} = -3 V, *and* **d.)** V_{abs} = -6 V.

Again, as seen from Fig. 4-9 a.)-d.), excellent agreement is seen between the predictions of the map in Fig. 4-7 and experimental observations for this device. For a pump current of 100 mA and an absorber bias of 0 V, the device is observed to be stably mode-locked, producing two pulses per round trip (Fig. 4-9a.)), and this state of second-harmonic mode-locking is maintained as the absorber bias is increased to -1V and -2V (Fig. 4-9b.)).

However, keeping the current fixed at 100 mA, when the absorber bias is increased to -3V, the device switches to a state of stable, fundamental mode-locked operation (Fig. 4-9c.)). This state of stable, fundamental mode-locking is maintained as the bias voltage on the absorber section is increased, with the best pulse quality achieved at a -6 V absorber bias (Fig. 4-9d.)).

And again, despite the numerous experimental observations of dynamical switching from fundamental to second-harmonic mode-locking and vice-versa, higher-order mode-locked states were extremely difficult to observe in most cases.

However, for one particular device (ZLG788A-AV06), under a gain section pump current of 166 mA and a very high absorber bias voltage of -7 V, a noisy, but stationary state of pulse-tripling was observed, seen in the high speed oscilloscope trace shown in Fig. 4-10.
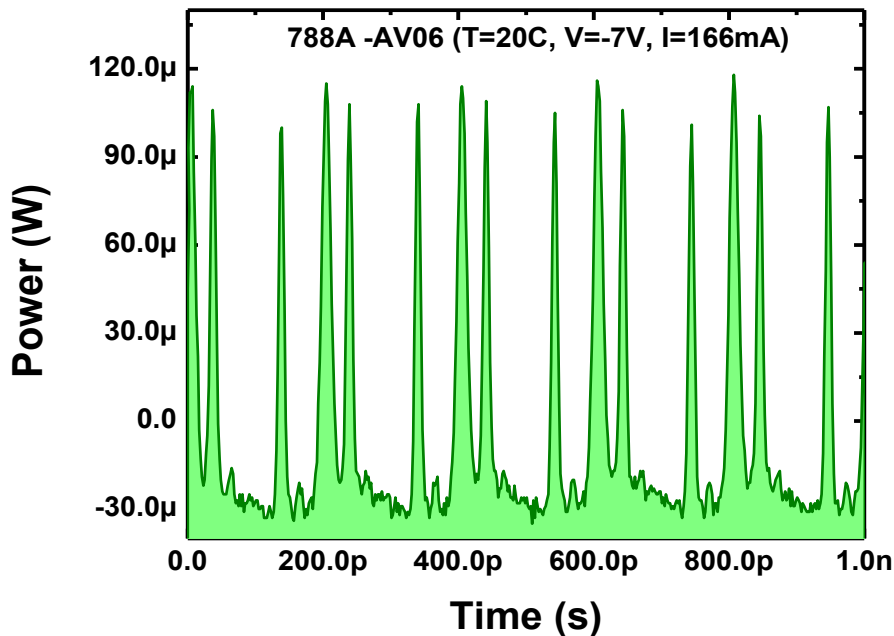
Figure 4-10: *High speed oscilloscope (140 GHz Tektronix DSA 8200 Digital Serial Analyzer) data for a noisy, but stationary 3-pulse state(Device ZLG788A-AV06).*

Although the harmonic mode-locking map in Fig. 4-7 extends only to an absorber bias of -6 V, extrapolation to a bias voltage of -7 V at a pump current of 166 mA predicts a three- or four- pulse state. More generally speaking, harmonic locking regimes with more than two pulses per round trip are predicted to be in the upper right corner of the map, so that the model predicts that for mode-locking regimes higher than second-order, high bias conditions (high pump current and strong absorber bias voltage) are necessary. Experimental observations show that while it is extremely difficult to achieve mode-locking regimes higher than second-order, it is possible, likely with careful device design and engineering, to achieve at least a pulse-tripling state, predicted by the model.

4.3   Chapter Summary

In this chapter, the predictive capabilities of the DDE model were explored in a couple of different contexts of practical importance. With a parameter space of just nine parameters, seven of which can be experimentally-extracted from measurements on the specific device under study, the model offers a powerful theoretical tool to study the nonlinear dynamics unique to that device.

First, the model was constrained as usual with measurement-extracted parameters, and the impact of unequal values of the linewidth enhancement factor in the gain and absorber sections on pulse structure was studied. While the results showed a degraded pulse structure for all cases with a significant difference of linewidth enhancement factors in the gain and absorber sections, the instabilities were predicted to be particularly severe for devices with a low gain-bandwidth profile (characterized by lower values of the spectral filtering coefficient γ) operated at lower temperatures, which included a

combination of pulse-splitting and satellite lobes. For such devices, operation at higher temperatures was predicted to temper the instabilities to some extent, but they were still found to be significant. Next, for devices with a wide gain-dispersion profile (characterized by higher values of the spectral filtering coefficient γ), a difference of the linewidth enhancement factors in the two sections predicted a closely-related dynamical instability, split-pulsing, wherein the individual pulse structures are characterized by two split lobes, varying in relative intensity over each round trip. The dynamic was interpreted as the synergistic interaction between the lobes of each pulse with the medium, following which the response of the medium was to apply feedback to perturb the gain and absorber dynamics of the device and thereby condition the pulse shape, resulting in one or the other of the two split lobes growing at the expense of the other. This prediction was confirmed with high speed oscilloscope measurements of a device fabricated with a wide gain-dispersion profile.

In the second part of the chapter, the DDE model was shown to offer a robust predictive modeling capability toward achieving higher pulse repetition rates for two-section, passively mode-locked quantum dot lasers. Consequently, the model was used to first find the regimes of mode-locked operation of a given device wherein the device was predicted to exhibit fundamental or harmonic mode locking, as a function of the dimensionless model parameters. The model parameters were then mapped to externally-controllable parameters (gain section pump current and absorber bias voltage), and the regimes of mode-locked operation were represented on a map, as a function of the said parameters that can be interactively controlled while the device is in operation. Excellent agreement was observed between the predictions of the model and high speed

oscilloscope measurements of the output pulse dynamics of fundamental and second-harmonic mode-locking for two devices with a similar epitaxial-layer structure, the first consisting of a 7 mm gain/1 mm absorber section, and the second with a 7.2 mm gain/0.8 mm absorber section (both with a 5 μm ridge waveguide design). A noisy, but stationary pulse-tripling regime was experimentally observed at a bias condition predicted by the model for one particular device. The approach not only presents an invaluable guideline toward achieving higher repetition rates without the need to re-engineer the device, but also points toward the highest repetition rates achievable in principle for a given two-section device.

Based on the predictions of the model in this chapter, we note that a critical requirement for both, the avoidance of unstable dynamical effects, as well as the generation of higher repetition rates by dynamically switching the device to stable, harmonically mode-locked regimes requires some method of direct control over the linewidth enhancement parameter seen by the pulse, such that not only is this value minimized to the maximum extent possible, but the difference in the value seen by the propagating pulse in the gain and the absorber sections needs to be as small as possible.

One technique that has been established recently as a promising method of manipulating the linewidth enhancement factor of a mode-locked quantum dot laser is externally applied optical feedback. In the next chapter, we present recent experimental results analyzing device performance under the influence of external optical feedback with regard to standard performance metrics such as RF linewidth and phase noise, which act as qualitative indicators of the linewidth enhancement parameter seen by the propagating pulse.

4.4   References for Chapter 4

[1] Raghunathan, R., Crowley, M., Grillot, F., Li, Y., Mee, J. K., Kovanis, V., & Lester, L. F. (2013). Pulse Characterization of Passively Mode-locked Quantum Dot Lasers Using a Delay Differential Equation Model Seeded with Measured Parameters.

[2] Raghunathan, R., Crowley, M. T., Grillot, F., Mukherjee, S. D., Usechak, N. G., Kovanis, V., & Lester, L. F. (2012, February). Delay differential equation-based modeling of passively mode-locked quantum dot lasers using measured gain and loss spectra. In *SPIE OPTO* (pp. 82551K-82551K). International Society for Optics and Photonics.

[3] Ohtsubo, J. (2013). Stabilization of Semiconductor Lasers. In *Semiconductor Lasers* (pp. 353-384). Springer Berlin Heidelberg.

[4] Keeler, G. A., Nelson, B. E., Agarwal, D., Debaes, C., Helman, N. C., Bhatnagar, A., & Miller, D. A. (2003). The benefits of ultrashort optical pulses in optically interconnected systems. *Selected Topics in Quantum Electronics, IEEE Journal of*, *9*(2), 477-485.

[5] Viktorov, E. A., Mandel, P., Kuntz, M., Fiol, G., Bimberg, D., Vladimirov, A. G., & Wolfrum, M. (2007). Stability of the mode-locked regime in quantum dot lasers. *Applied physics letters*, *91*(23), 231116-231116.

[6] Kane, D. M., & Shore, K. A. (Eds.)., Chap. 6 (2005). *Unlocking dynamical diversity: optical feedback effects on semiconductor lasers*. Wiley. com.

[7] Vladimirov, A. G., & Turaev, D. (2005). Model for passive mode locking in semiconductor lasers. *Phys. Rev. A*, *72*(3), 033808.

[8] Vladimirov, A. G., Pimenov, A. S., & Rachinskii, D. (2009). Numerical study of dynamical regimes in a monolithic passively mode-locked semiconductor laser. *Quantum Electronics, IEEE Journal of*, *45*(5), 462-468.

[9] Raghunathan, R., Braga, A., Crowley, M., Mee, J., & Lester, L. (2013, June). Dynamics of Split-Pulsing in a Two-Section Passively Mode Locked Quantum Dot Laser. In *CLEO: QELS_Fundamental Science*. Optical Society of America.

[10] Komarov, A. K., & Komarov, K. P. (2000). Pulse splitting in a passive mode-locked laser. *Optics communications*, *183*(1), 265-270.

[11] Kuntz, M., Fiol, G., Laemmlin, M., Meuer, C., & Bimberg, D. (2007). High-speed mode-locked quantum-dot lasers and optical amplifiers. *Proceedings of the IEEE*, *95*(9), 1767-1778.

[12] Carpintero, G., Thompson, M. G., Penty, R. V., & White, I. H. (2009). Low noise performance of passively mode-locked 10-GHz quantum-dot laser diode. *Photonics Technology Letters, IEEE*, *21*(6), 389-391.

[13] Schmeckebier, H., Fiol, G., Meuer, C., Arsenijević, D., & Bimberg, D. (2010). Complete pulse characterization of quantum dot mode-locked lasers suitable for optical communication up to 160 Gbit/s. *Optics express*, *18*(4), 3415-3425.

[14] Bimberg, D., Fiol, G., Kuntz, M., Meuer, C., Laemmlin, M., Ledentsov, N. N., & Kovsh, A. R. (2006). High speed nanophotonic devices based on quantum dots. *physica status solidi (a)*, *203*(14), 3523-3532.

[15] Delfyett, P. J., Hartman, D. H. and Ahmad, S. Z., "Optical clock distribution using a mode-locked semiconductor laser diode system", J. Lightwave Technol. vol. 9(12), 1646-1649 (1991).

[16] Vehovc, S. (2000). Clock recovery at gigabit-per-second data rates. *MICROWAVE JOURNAL-EUROGLOBAL EDITION-, 43*(7), 22-63.

[17] Xin, Y.-C., Li, Y., Kovanis, V., Gray, A. L., Zhang, L. and Lester, L. F. , "Reconfigurable Quantum dot Monolithic Multi-Section Passive Mode-Locked lasers", Opt. Express, vol. 15(12), 7623-7633 (2007).

[18] Li, Y., Chiragh, F. L., Xin, Y.-C., Lin, C.-Y., Kim, J., Christodoulou, C. G. and Lester, L. F., "Harmonic mode-locking using the double interval technique in quantum dot lasers," Opt. Express, 18(14), pp. 14637-14643, (2010).

[19] Crowley, M. T., Murrell, D., Patel, N., Breivik, M., Lin, C. -Y., Li, Y., Fimland, B. O. and Lester, L. F., "Analytical modeling of the temperature performance of monolithic passively mode-locked quantum dot lasers", IEEE J. Quantum Electron. 47(8), 1059-1068 (2011).

[20] Usechak, N. G., Xin, Y. -C., Lin, C. -Y., Lester, L. F., Kane, D. J. and Kovanis, V., "Modeling and direct electric field measurements of passively mode-locked quantum-dot lasers," IEEE J. Sel. Top. Quantum Electron. 15, 653–660 (2009).

[21] Raghunathan, R., Mee, J. K., Crowley, M. T., Grillot, F., Kovanis, V., & Lester, L. F. (2013, March). Modeling and characterization of pulse shape and pulse train dynamics in two-section passively mode-locked quantum dot lasers. In *SPIE OPTO* (pp. 86190C-86190C). International Society for Optics and Photonics.

Chapter 5

Experimental Study of Device Dynamics under External Optical

Feedback at Elevated Temperature

In chapters 2, 3 and 4, the nonlinear dynamical trends of a passively mode-locked quantum dot laser were studied numerically using a Delay Differential Equation model with operating temperature, gain section current, and absorber bias voltage as the external control parameters. Based on the results of simulation in Chapter 4, the linewidth enhancement factor (LEF) seen by the pulse in the gain and absorber sections of the device was predicted to be critical to determining the output dynamics of the device, so that any variation in the values of the LEF in the two sections was seen to quickly introduce instabilities into the output. While the electrical bias controls influence the values of the LEF in the individual sections by virtue of influencing the respective carrier concentrations, a more direct form of external control is highly desirable. One such mechanism of external control is afforded by external optical feedback, which has, in recent works, been shown to dramatically improve RF performance metrics such as RF linewidth, phase noise and pulse-to-pulse timing jitter [1-5]. In an effort to gain insight into the same, one of the studies undertaken as part of this dissertation was to experimentally investigate the RF and optical performance of a passively mode-locked two section device operating at elevated temperature, with and without the influence of optical feedback from an external reflector.

This chapter is organized as follows. After a brief overview of the setup used for the free-running device characterization in section 5.1, section 5.2 starts with basic device

characterization using L-I curves and mode-locking stability maps over temperature. A more detailed characterization using RF and optical spectra is then presented. Section 5.3 presents similar characterization results for the device operating under externally applied optical feedback, first as a function of variable optical delay (section 5.3.1), and subsequently, as a function of feedback strength (section 5.3.2). Concluding remarks are presented in section 5.4.

5.1 Experimental Setup to Characterize the Solitary Device

As in the previous cases, the epitaxial structure of the laser was comprised of a multi-stack "Dots-in-a-Well" (DWELL) structure, fabricated as an optimized 6-stack active region, with InAs QDs embedded in an InGaAs QW, epitaxially grown by solid source Molecular Beam Epitaxy (MBE) on a GaAs substrate. The total laser cavity length was 7.8 mm, with a 6.7 mm gain section and a 1.1 mm saturable absorber section (as shown in the schematic in Figure 5-1). A highly reflective coating (R ≈ 95%) was applied to the facet adjacent to the SA section, while the facet adjacent to the gain section was left as-cleaved (R ≈ 32%). The entire 2-section device was packaged in an encapsulating module to minimize the effects of external noise.The packaged module is affixed onto an industry-standard 14-pin "butterfly" mount, which enables temperature control with an in-built thermo-electric controller, as well as electrical biasing for the absorber and gain sections. Figure 5-1 shows a schematic of the experimental setup.
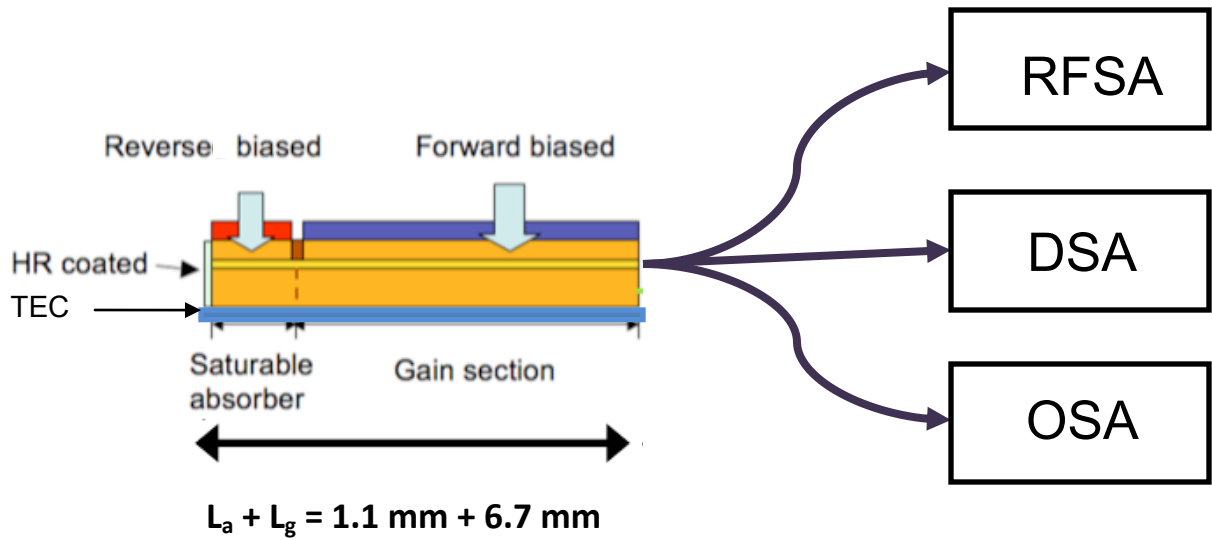
Figure 5-1: *Schematic of a 2-section device in the free-running configuration (RFSA: RF Spectrum Analyzer, DSA: Digital Serial Analyzer, OSA: Optical Spectrum Analyzer, TEC: Thermoelectric Control module).*

5.2 Free-Running Characterization of the Device

The light-current (L-I) characteristics for the device are shown in Figure 5-2.
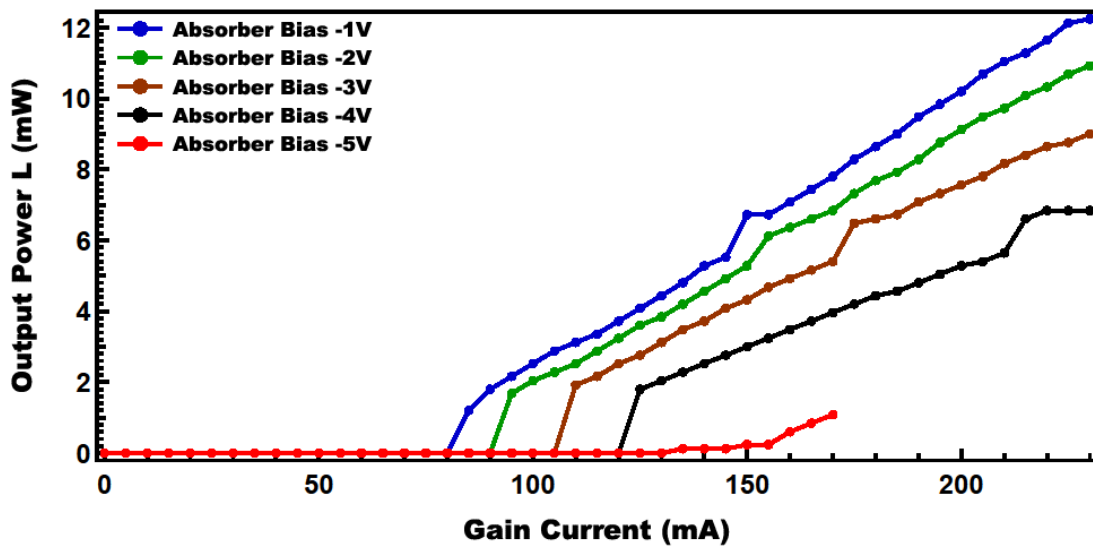
Figure 5-2: *L-I curves as a function of absorber bias for the device under study.*

Based on the L-I curves for the device, it may be inferred that mode-locking performance would likely begin to degrade at a -5V absorber bias. This was later confirmed during the feedback characterization of the device, where it was found that due to the inherently low output power of the pulses emitted from the free-running device at a -5V absorber bias condition, the signal-to-noise ratio after roundtrip propagation through the external cavity (feedback loop) was too low for a reasonable RF and optical characterization.

In order to find the optimum operating conditions for stable mode-locking, the device was first operated in a free-running configuration, without the external feedback loop. Based on the quality of output pulses obtained, a mode-locking map was generated, as shown in Fig. 5-3.
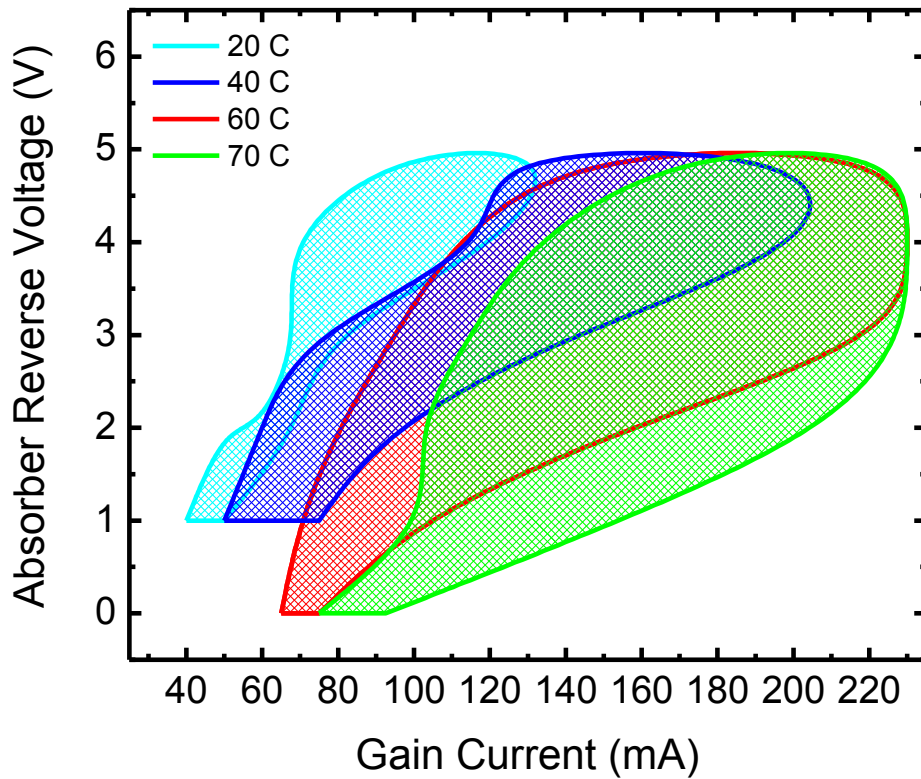
Figure 5-3: *Map showing regions of mode-locked operation as a function of bias conditions.*

As seen clearly from the mode-locking map in Fig. 5-3, the device exhibited the widest region of operational stability (in terms of gain section pump current and absorber reverse bias voltage) at an operating temperature of 70℃. This supports previous experimental work [6-10], where mode-locking performance was found to be optimum in the 50 − 80℃ range. In [6-8], the improved mode-locking performance in this elevated temperature range was attributed to faster absorber recovery times, owing to faster rates of thermionic emission. Furthermore, the findings in [9] and [10] suggest additional factors governing the optimum mode-locking stability, such as reduced values of unsaturated gain and absorption, so that the propagating pulse is subjected to less distortion, and consequently, more gradual shaping.

In the RF domain, the line width of the fundamental frequency of the RF spectrum observed on an electrical spectrum analyzer is a signature of the phase noise of the device. In order to reduce the latter, it is critical to reduce the former to as low a value as possible. Resonant optical feedback, wherein light reflected from an external cavity propagates a distance that is approximately an integer multiple of the length of the laser cavity, has been shown to dramatically reduce RF line width at room temperature. On the other hand, the quality of mode-locked pulses produced by QDMLLs has been shown to improve with temperature, with an optimum mode-locking performance in the 50 − 80℃ range for typical devices. Consequently, the effects of optical feedback at elevated temperature not only offer a natural and important avenue for further investigation, but the complexity added by effects such as absorption saturation, gain/absorption peak "walk-off" and the quantum confined stark effect (QCSE) that become significant in QD systems at elevated temperatures combined with an applied absorber bias voltage, could

potentially result in device behavior that shows a significant departure from performance at lower temperatures. To this end, the following part of this dissertation is devoted to investigating the dynamical trends exhibited by the RF and optical spectra of a passively mode-locked QD laser operating at elevated temperature, with and without the influence of external optical feedback. In accordance with the map shown in Fig. 5-3, the device exhibited optimum mode-locking performance at 70 ℃, so that the operating temperature was fixed at this value. The first step toward the feedback characterization of the device is to acquire the RF and optical spectra of the solitary (free-running) device. The corresponding spectra measured under externally applied optical feedback can then be compared to these spectra. Table 5-1 shows the measured center frequency and RF line width values for the free-running laser at an operating temperature of 70 ℃ and a gain section pump current of 215 mA, as a function of absorber bias voltage.

Table 5-1: *Center Frequency and RF Linewidth Measurements of the Solitary Device (T = 70 ℃ and I$_{gain}$ = 215 mA)*

Absorber Bias (V)	Centre Frequency (GHz)	RF Linewidth (Hz)
1.5	5.38151	25567
2	5.38322	4434
2.5	5.38426	4509
3	5.38595	272770
3.5	5.3864	160055
4	5.40605	28874

The measurements were performed by directly connecting the fiber pigtailed output of the solitary device to a 45 GHz bandwidth photodiode coupled to an RF spectrum analyzer. The variation in the RF line width of the device with applied absorber bias may be plotted as shown in Fig. 5-4.
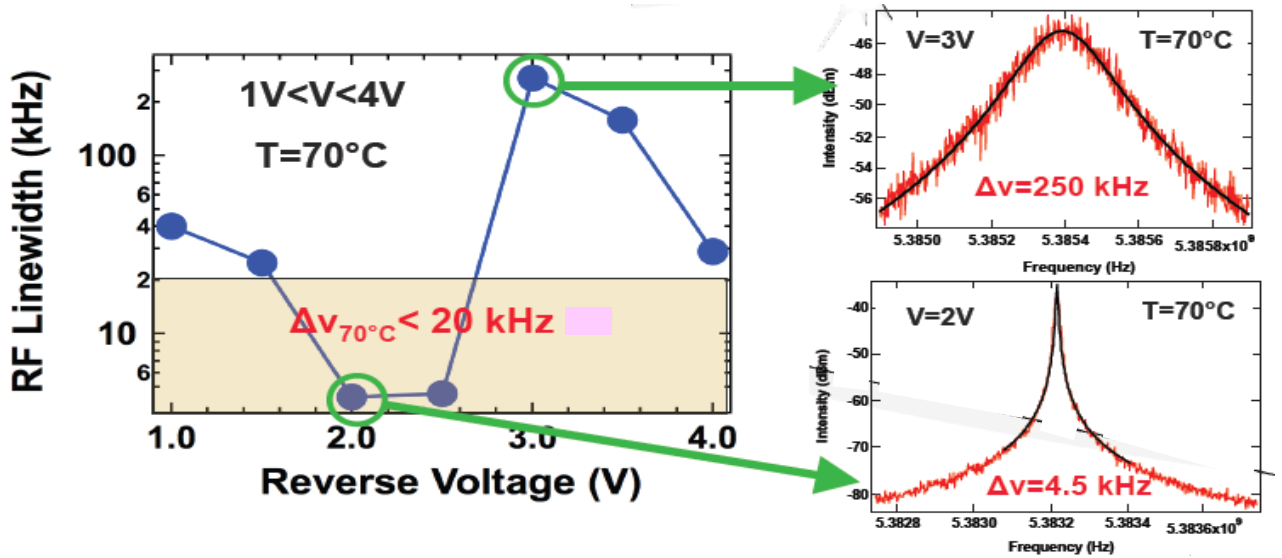
Figure 5-4: *RF linewidth measurements of the solitary device as a function of absorber bias (T = 70 ℃ and I_{gain} = 215 mA).*

As apparent from Fig. 5-4, the RF line width of the device shows a very wide variation over the range of absorber bias voltages applied, from an ultralow value of 4.5 kHz in the -2 to -2.5 V bias range, to a much broader value of 273 kHz at -3 V.

Prior to considering the effect of externally applied optical feedback, it is instructive to study the influence of the applied absorber bias alone. The influence of varying absorber bias voltage on the dynamical behavior of two-section quantum dot lasers with an integrated intracavity saturable absorber has been previously studied in detail in works such as[11] and [12] to account for observed trends such as hysteresis, optical bistability

and wavelength bistability. In [11], the continuous wave bistability in the light-absorber bias characteristic was attributed to a combination of nonlinear absorption saturation and electroabsorption induced by the Quantum Confined Stark Effect (QCSE) caused by an applied electric field. More recent work by Feng et al [12] reported wavelength bistability in a two-section, passively mode-locked quantum dot laser, wherein the device dynamics were attributed to the interplay between spectral hole burning in the gain spectrum of the device and QCSE due to the reverse bias applied on the absorber section. Since QCSE is key to determining device behavior under an applied absorber bias voltage, it behooves us to briefly review this phenomenon here.

5.2.1 The Quantum Confined Stark Effect (QCSE)

Consider a quantum well structure, which can be thought of as an infinite square well potential over a distance L within the semiconductor barrier layer. A particle confined within such a potential has an associated momentum vector $k_z = (n\pi/L)$, assuming confinement in the z-direction. The wavefunction $\psi_n(z)$ associated with a particle of effective mass $m*$ confined in such a potential satisfies the time-independent Schrödinger equation, $\hat{H}_0|\psi_n\rangle = E_n|\psi_n\rangle$

$$\Rightarrow -\frac{\hbar^2}{2}\frac{\partial}{\partial z}\left(\frac{1}{m*}\frac{\partial}{\partial z}\right)\psi_n(z) = E_n\psi_n(z)$$

(5-1)

where, $\hat{H}_0$ represents the *unperturbed* Hamiltonian of the system, whereby the normalized wavefunction $\psi_n(z)$ and eigenenergy E_n are given by:

130

$$\psi_n(z) = \sqrt{\frac{2}{L}} \cos\left(\frac{n\pi}{L} z\right), \text{ for odd n.}$$

$$= \sqrt{\frac{2}{L}} \sin\left(\frac{n\pi}{L} z\right), \text{ for even n.}$$

(5-2)

$$\text{and, } E_n = \frac{\hbar^2}{2m*}\left(\frac{n\pi}{L}\right)^2$$

(5-3)

The corresponding wavefunctions in the valence band and the conduction band are as shown in Fig. 5-5.
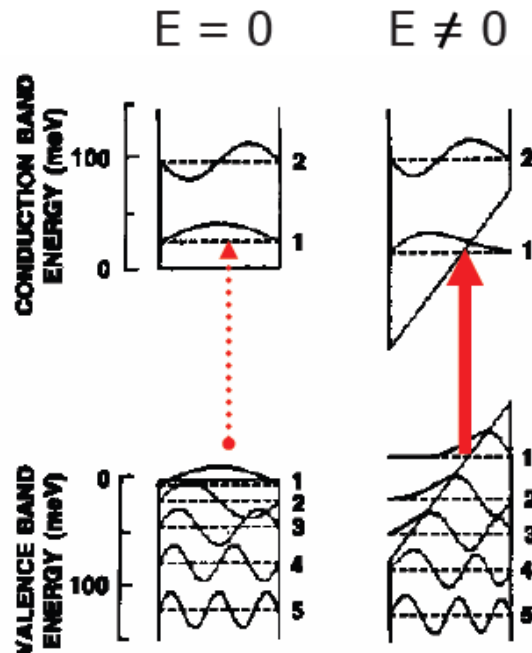
Figure 5-5 [13]: *Valence and Conduction band wavefunction confinement for the cases of no applied bias voltage (E = 0, left) and an applied bias voltage (E ≠ 0, right).*

131

Light incident on the medium causes interband transitions which leads to photon absorption and carrier generation. The transition rate of an electron from an initial state in the valence band to a final state in the conduction band is determined by the overlap of the associated wavefunctions. The wavefunction overlap between an initial state $|\psi_i\rangle = |n,v\rangle$ and final state $|\psi_f\rangle = |m,c\rangle$ determines the absorption coefficient corresponding to the transition. The application of a bias voltage on the absorber section causes a reduction in the energy of the bound states, which, in turn, causes the tails of the wavefunctions in the valence and conduction bands to penetrate the previously-forbidden band gap region, as can be seen from the diagram on the right side of Fig. 5-5. A careful comparison between the energy-level diagrams on the left and right side of Fig. 5-5 reveals that there is a change induced in the energy-level spacing between the valence and conduction band levels upon application of a bias potential. This shift in energy-spacing can be calculated using Perturbation Theory, so that the applied bias voltage is incorporated as a "small" perturbation to the Hamiltonian of the unperturbed system in equation (5-1):

$$\hat{H} = \hat{H}_0 + \lambda \hat{U}_{applied}$$

(5-4)

where λ is an infinitesimal parameter and $\hat{U}_{applied}$ represents the applied absorber bias voltage. The modified Schrödinger equation may be expressed as:

$$\left(\hat{H}_0 + \lambda \hat{U}_{applied}\right)\psi_n' = E_n' \psi_n'$$

(5-5)

where,
$$\psi_n'(\lambda) = \psi_n + \lambda\psi_n^{(1)} + \lambda^2\psi_n^{(2)} + ...$$

<div align="right">(5-6)</div>

and,
$$E_n'(\lambda) = E_n + \lambda E_n^{(1)} + \lambda^2 E_n^{(2)} + ...$$

<div align="right">(5-7)</div>

Under this new formalism, each state undergoes a shift in its energy due to the perturbing potential, which can be calculated as a second-order correction to the unperturbed energy [14]:

$$E_n^{(2)} = \sum_{n \neq m} \frac{\left|\left\langle \psi_m \left| \lambda\hat{U}_{applied} \right| \psi_n \right\rangle\right|^2}{\left(E_n - E_m\right)}$$

<div align="right">(5-8)</div>

Thus, the application of the external bias voltage enables penetration into the previously – forbidden band gap region, which causes an overlap of the electron and hole wavefunctions and a change in the energy level-spacing between the valence and conduction band levels, which can be found from equation (5-8). This, in turn, allows the absorption of photons with energy lower than the band gap of the unperturbed structure. This lower energy has the concomitant effect of red-shifting the absorption band edge ([13], [15]). As reported previously in [12], the overall effect on the laser cavity (absorber plus gain section) is seen as a smoothing-out and filling of any notch/hole in the optical spectrum, followed by the eventual blue-shift of the gain peak.

Similar dynamical trends were observed in the device used in this work (ZLG0016). Optical spectra were recorded using a Yokogawa ANDO AQ6317C Optical Spectrum Analyzer. The device was set at an operating temperature of 70℃, the gain section was

pumped with a current source set to deliver 215 mA, and the absorber bias voltage was varied.

Fig. 5-6a shows the measured optical spectrum for the free-running device at an absorber bias of -1V. This condition was seen to produce the deepest and sharpest spectral hole, with a peak-to-valley extinction ratio > 20 dBm.
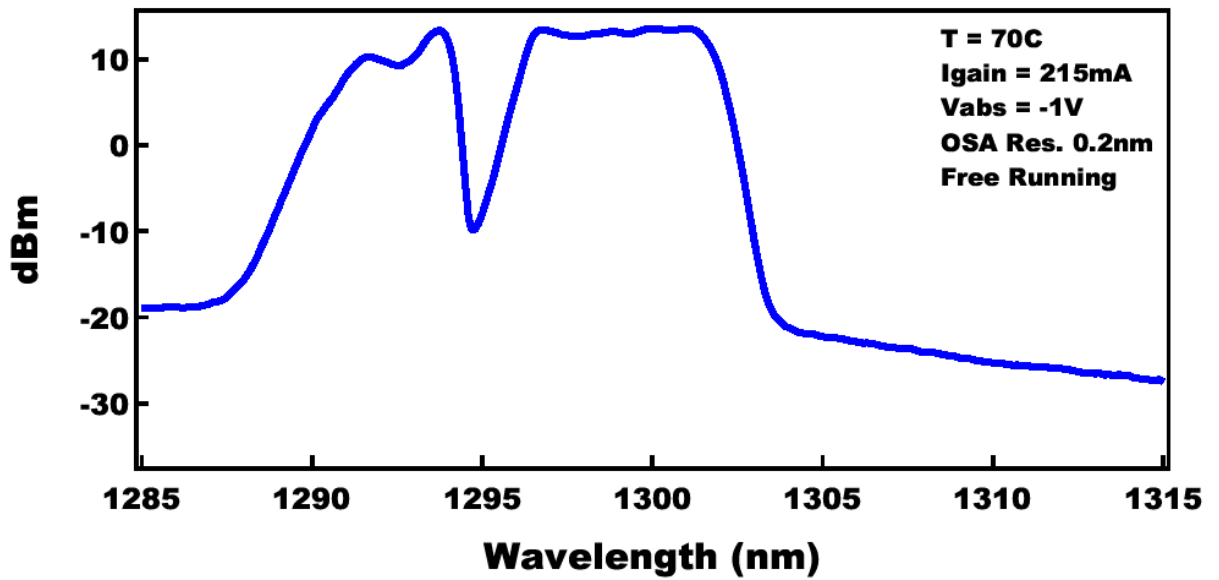
Figure 5-6a: Free-running optical spectrum at $T = 70\,°C$, $I_{gain} = 215$ mA, $V_{abs} = -1V$.

As the absorber bias is increased to -2V, the spectral hole widens and becomes less deep, with a peak-to-valley extinction of ~ 15 dBm. Simultaneously, the optical spectrum broadens on the longer wavelength side, so the tail of the spectrum is now seen to extend past the 1305 nm limit (Fig. 5-6b).
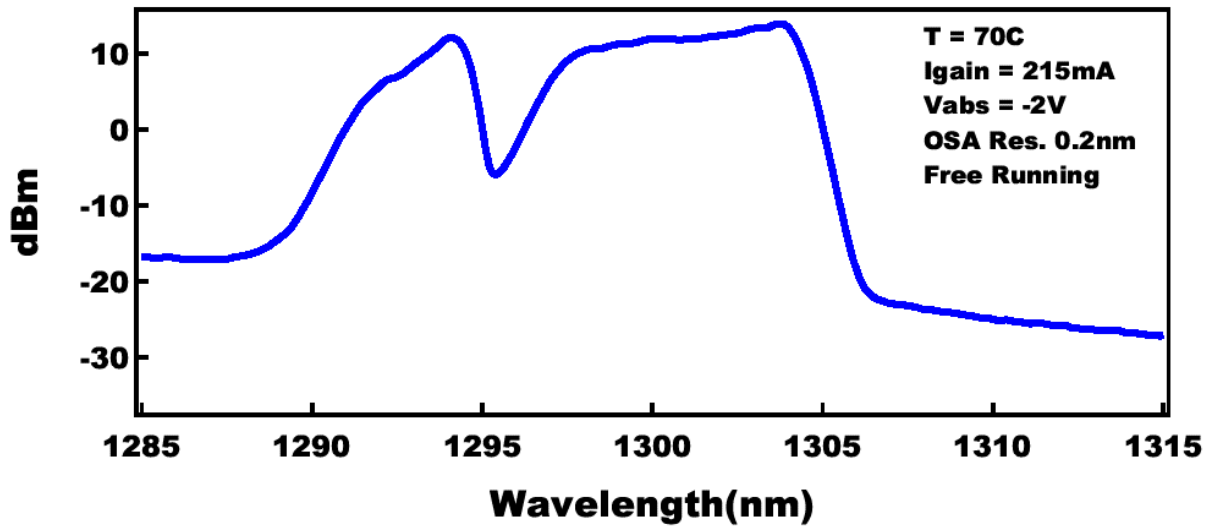
Figure 5-6b: Free-running optical spectrum at T = 70°C, I_{gain} = 215 mA, V_{abs} = -2V.

The same trend is seen as the absorber bias is increased to -3V (Fig. 5-6c) and subsequently to -4V (Fig. 5-6d). The spectral hole appears visibly wider and much shallower than at lower bias voltages, with the peak-to-valley extinction now decreasing to < 10 dBm, and the spectrum extending to 1310 nm.
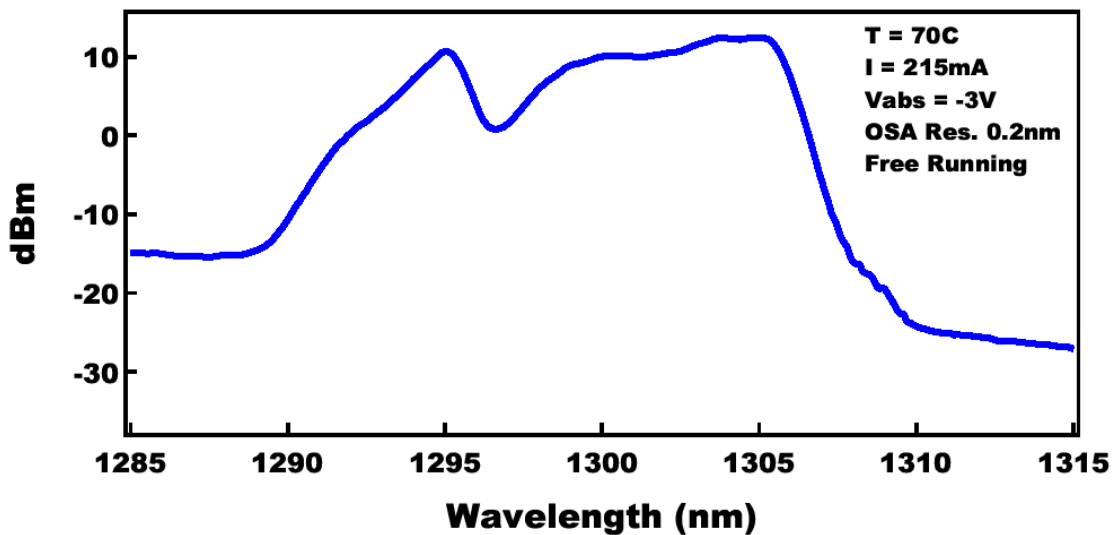
Figure 5-6c: Free-running optical spectrum at T = 70°C, I_{gain} = 215 mA, V_{abs} = -3V.
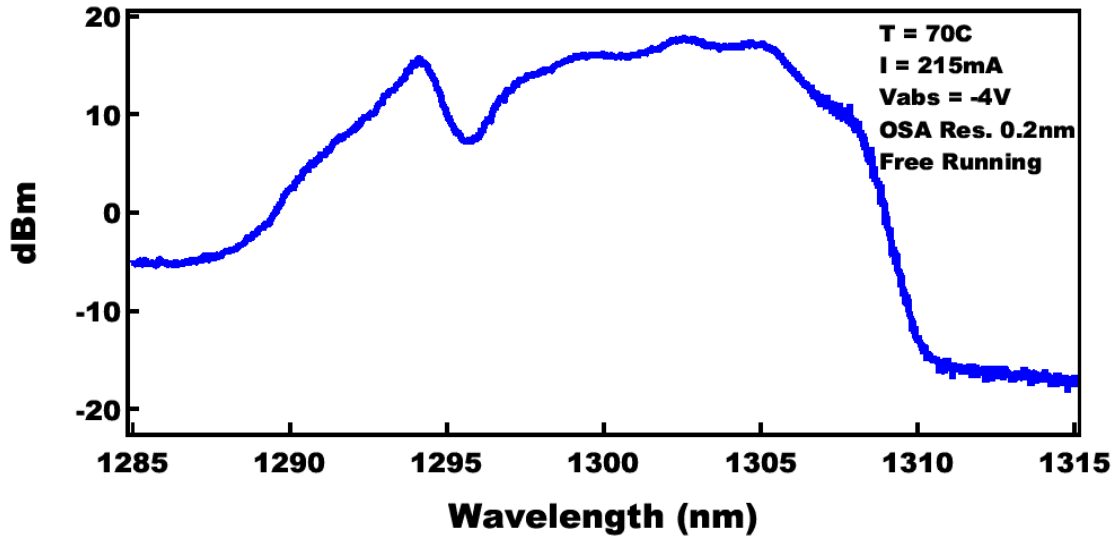
Figure 5-6d: Free-running optical spectrum at $T = 70\,°C$, $I_{gain} = 215\ mA$, $V_{abs} = -4V$.

Past a bias voltage of -4V, however, a drastic and rather interesting change is seen. The spectral hole disappears, leaving a smooth, continuous spectral envelope, and the entire spectrum blue shifts. This is clearly seen below in Fig. 5-6e, where a bias voltage of -4.5V was applied on the absorber section. The entire spectrum is blue-shifted by ~ 6nm, and centred at ~ 1289 nm.
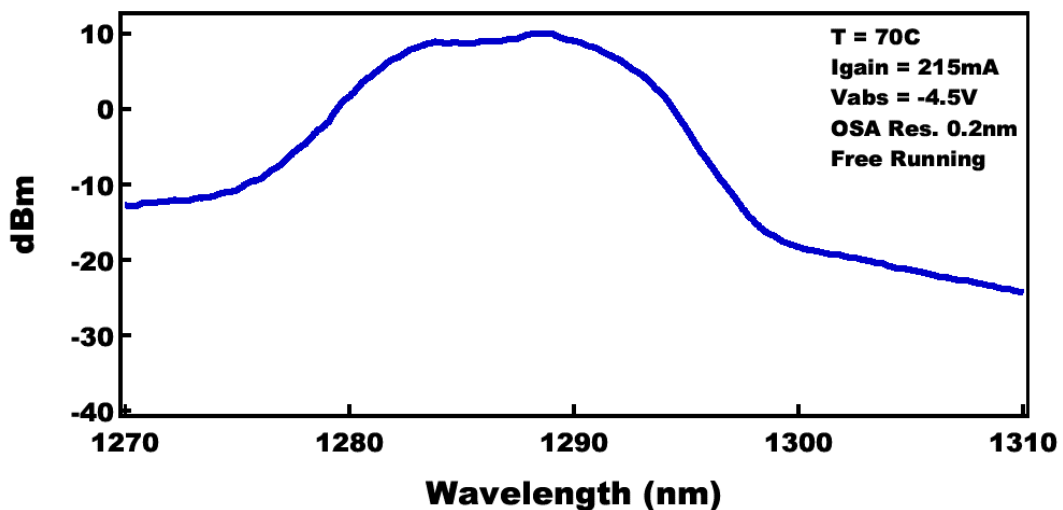
Figure 5-6e: Free-running optical spectrum at $T = 70\,°C$, $I_{gain} = 215\ mA$, $V_{abs} = -4.5V$.

The trends seen in the optical spectra shown above in Fig. 5-6a-e suggest the interplay between two separate effects caused by varying the bias voltage on the absorber section, the formation of a "spectral hole", and the Quantum Confined Stark Effect (QCSE), as being the driving factor behind the behavior of the optical spectrum of the device. At low bias voltages, spectral hole formation dominates, as seen from the depth and the sharpness of the hole formed in the spectrum (Fig. 5-6a and b). As the bias voltage is increased, the QCSE first competes with the hole formation at moderate bias voltages, so that the spectral hole becomes visibly wider and shallower (Fig. 5-6c and d), and eventually dominates, as seen from the complete disappearance of the spectral hole in Fig. 5-6e, accompanied by the blue-shift of the spectrum. This entire sequence of events shows good agreement with the findings presented in [12].

This begs the question of what related effect, if any, is impressed upon the line width of the fundamental line of the RF spectra of the photocurrent generated by the device. This is critical to getting a sense of performance metrics such as phase noise and timing jitter of the device at each operating condition. A glance at Table 5-1 and Fig. 5-4 suggests that while regimes of operation where spectral hole formation is dominant generally exhibit lower RF line widths compared to the cases where QCSE becomes significant, and the transition from the former to the latter could possibly result in a sudden and drastic broadening of the RF line width, no clear trends are otherwise identifiable, particularly within each regime of operation.

These issues are investigated in further detail in the next section, where the effect of externally applied optical feedback on the dynamics of the device is studied.

5.3   Device Characterization under Externally Applied Optical Feedback

The setup used for optical feedback characterization of the device is shown in Fig. 5-7.
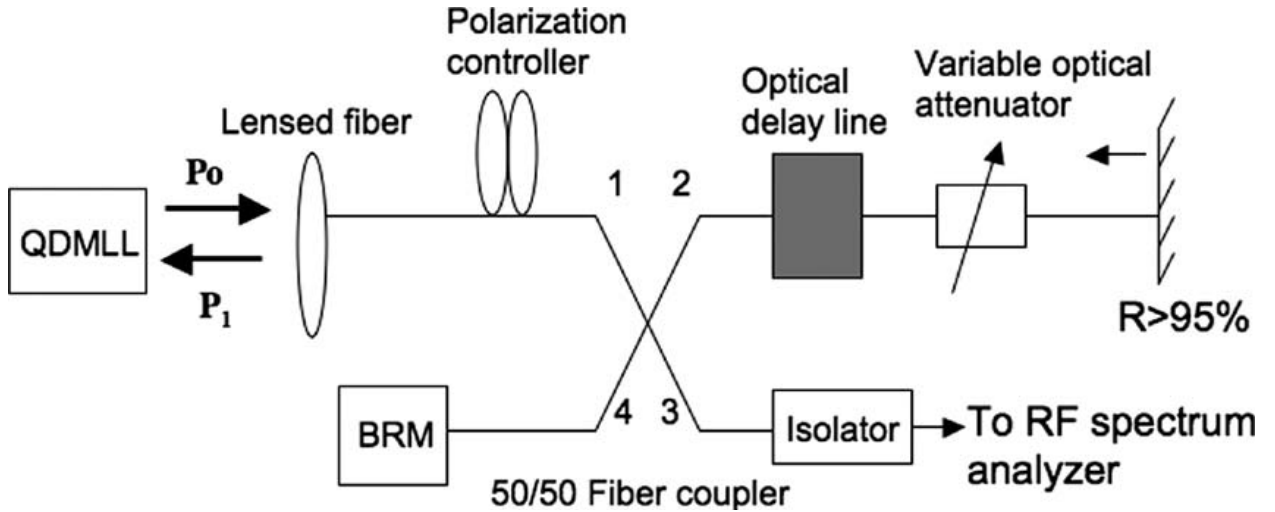
Figure 5-7: Schematic of experimental setup for optical feedback characterization.

A polarization controller is used to make the feedback beam polarization identical to the emitted wave, and the external cavity length in this setup is controlled with an optical delay line (ODL) that has a step-controlled motorized delay stage with a resolution of 1 fs, while the feedback power level is controlled using a variable optical attenuator (VOA). This introduces two additional control parameters, in addition to the absorber bias voltage – the optical delay setting and the feedback strength. In the following, a detailed study of each of these parameters is first performed individually to determine their effect, if any, on the RF linewidth and optical spectrum of the device while all other control parameters are held fixed. Finally, with the optimum settings of the ODL and the VOA determined, the absorber bias voltage is used as the sole control parameter to study and compare device performance under optical feedback, relative to the free-running

configuration. The feedback-regime (strong, moderate or weak), designated FBR in this chapter, is monitored at port 4 using a back reflection monitor (BRM) power meter.

Due to the combination of the losses involved in the long external fiber loop-cavity, combined with the higher mode-locking threshold at elevated temperature, the pump current had to be set above 160 mA in order to get measurable data. Optimum performance was observed at 170 mA and 215 mA.

5.3.1 Effect of Varying the Optical Delay Line (ODL) Setting

i. RF Spectrum Characterization:

Since the free-running characterization of the device showed the -3V bias condition to cause the highest linewidth broadening, and consequently, the worst RF noise performance, it is highly desirable to study the effect of external optical feedback at this absorber bias condition in detail. In this section, the results of RF line width measurement as a function of optical delay are presented. The experiment involved biasing the device at an operating temperature of 70℃, pump current of 170 mA and an absorber bias of -3V. The variable optical attenuator was set to provide a constant back-reflected power level of -25 dBm (monitored on the back reflection monitor at port 4 of the setup).

Table 5-2 shows measured values of center frequency and line width corresponding to the fundamental peak of the RF spectrum recorded on an RF Spectrum Analyzer (Agilent 8565 EC, measurement range 9 kHz – 50 GHz), connected to port 3 of the setup through a fast photodiode with a bandwidth of 45 GHz.

Table 5-2: *Center Frequency & RF Linewidth vs Optical Delay*

Optical Delay (ps)	Center Frequency (GHz)	RF Linewidth (Hz)
0	5.38923	47043
10	5.38956	30197
20	5.38960	31427
30	5.38953	31479
40	5.38951	32149
50	5.38949	33862
60	5.39030	69820
62	**5.38987**	**213310**
70	5.38984	13861
80	5.38935	43160
90	5.38910	41632
100	5.38949	33942
110	5.38949	31833
120	5.38947	29097
130	5.38950	28727
140	5.38948	30005
150	5.38947	29095
160	5.38993	14061
170	5.38946	29083
180	5.38916	29166
190	5.38944	31016
200	5.38946	32032
210	5.38946	25812
220	5.38944	32972
230	5.38943	25517
240	5.38943	42491
250	**5.38982**	**200102**
260	5.38953	32741
270	5.38921	25532
280	5.38930	45165
290	5.38944	28248
300	5.38944	28323
310	5.38943	21474
320	5.38941	23660
330	5.38940	34134

Fig. 5-8 shows a plot of the RF line width values reported in the third column of Table 5-2 as a function of optical delay.
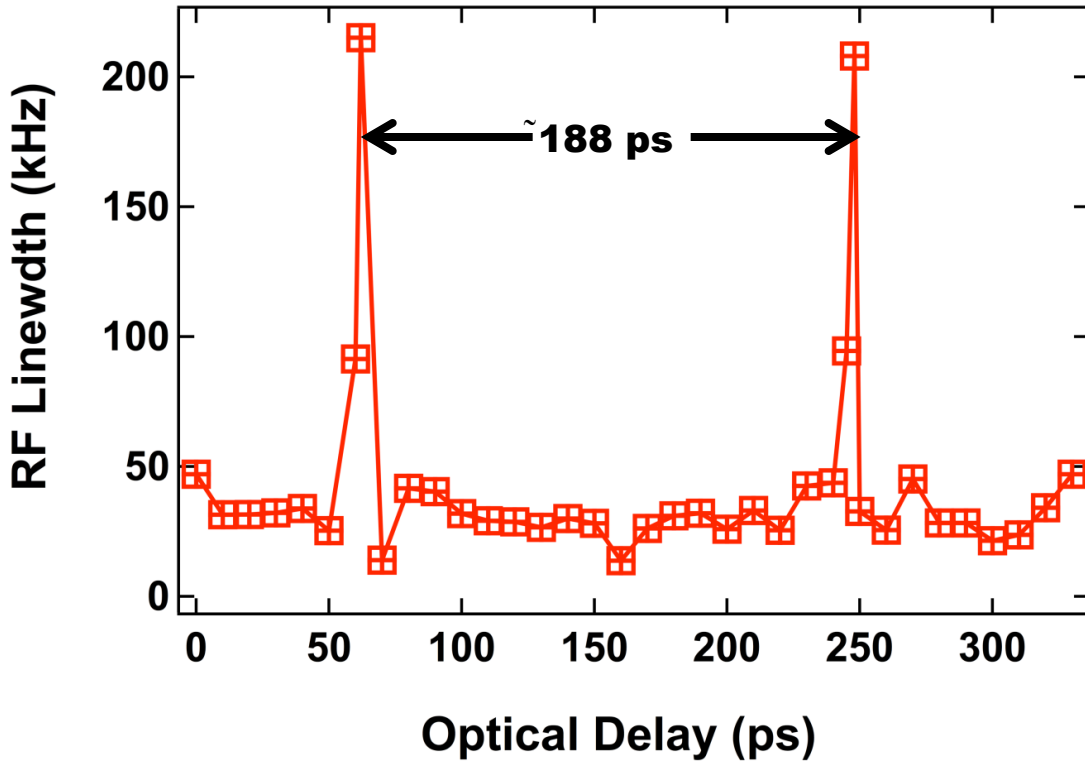
Figure 5-8: RF Linewidth as a function of optical delay (FBR at Port 4 = -25 dBm)

The key features of the plot are a sudden and drastic enhancement of RF line width to over 200 kHz at delay settings of 62 ps and 250 ps (values shown in bold in Table 5-2), followed immediately by an equally dramatic reduction to much lower values of 13.861 kHz and 32.741 kHz at delay settings of 70 ps and 260 ps, respectively. The fundamental line width traces (red) recorded on an RF Spectrum Analyzer, along with their Lorentzian curve fits (black) and extracted optimum 3-dB line widths are shown in Fig. 5-9. The top row (Fig. 5-9a) shows the line width broadening corresponding to the peaks at 62 ps and 250 ps in Fig. 5-8, while the bottom row (Fig. 5-9b) shows the subsequent reduction at 70

141

ps and 260 ps, respectively. In each case, the resolution bandwidth of the RF Spectrum

Analyzer was set to 10 kHz.
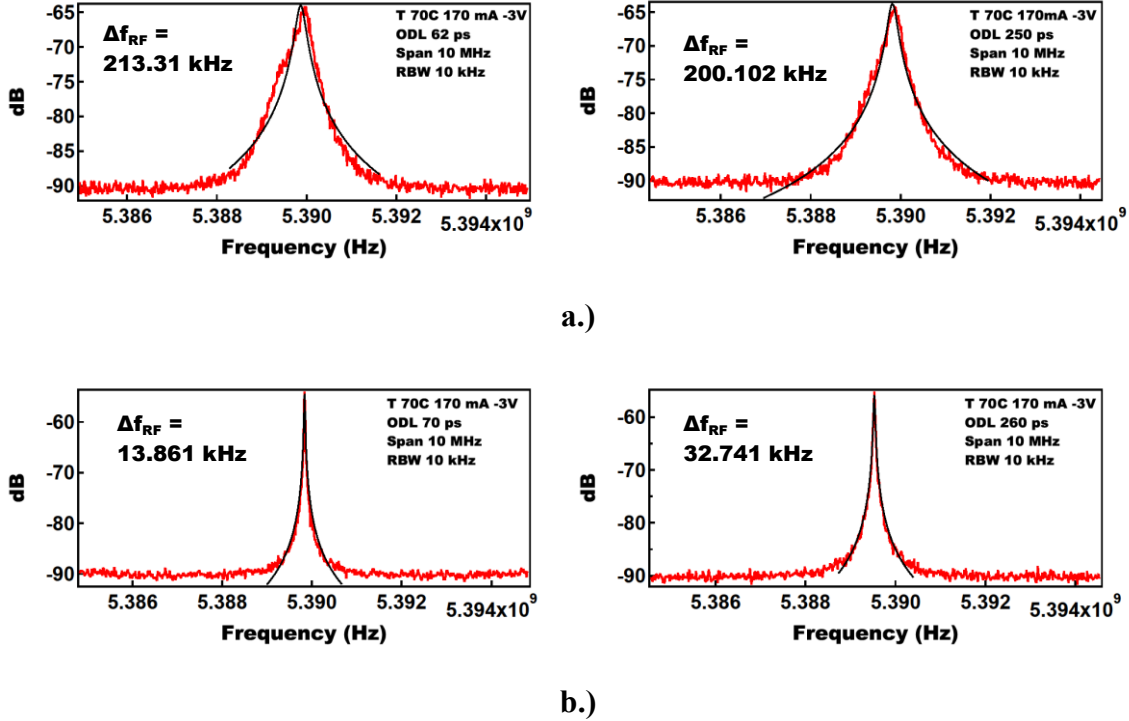
*Figure 5-9: RF Linewidth Measurements **a.)** ODL 62 ps (left) & 250 ps (right), and **b.)** ODL 70 ps (left) & 260 ps (right).*

The broad trends seen in Fig. 5-8 and 5-9 corroborate previous results reported in [2] for

a QDMLL under external optical feedback at 20℃. In particular, the periodicity of RF

line width enhancement seen above in Fig. 5-8 is 188 ps, corresponding approximately to

the fundamental repetition rate of the device. The concomitant shift of center frequency,

seen above in Table 5-2, also confirms the observations in [2] for a QDMLL and in [16]

for a QWMLL.   In addition, the results presented in this chapter also provide

experimental verification at elevated temperature for the nonlinear dynamical regimes

predicted through numerical simulation results in [17]. The line width enhancement at

optical delay settings of 62 ps and 250 ps correspond to the non-resonant case, whereby

the ratio of the external cavity length to the laser cavity length, L_{ext}/L_{las}, is not an integer, as opposed to the near-exactly resonant case for optical delay settings of 70 ps and 260 ps, whereby the ratio L_{ext}/L_{las} is nearly an exact integer value.

ii. Optical Spectrum Characterization:

As in the case of the solitary device, optical spectra were recorded using a Yokogawa ANDO AQ6317C Optical Spectrum Analyzer. The objective of this measurement was to determine any possible perturbations to the optical spectra of the free-running device due to changes in the ODL setting alone. The gain section was pumped at 170 mA and an absorber bias of -3V was applied, while the variable optical attenuator was set to maintain a constant feedback power level of -8 dBm at port 4. Fig. 5-10 shows the measured optical spectra.
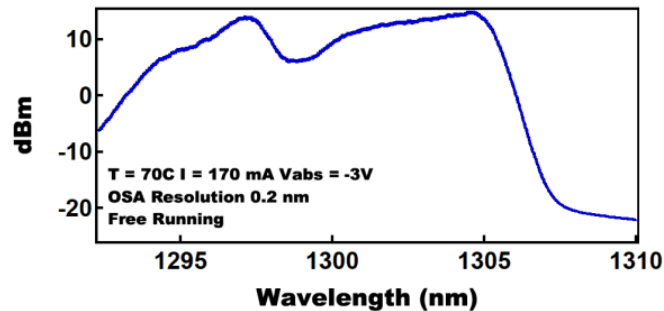
a.)
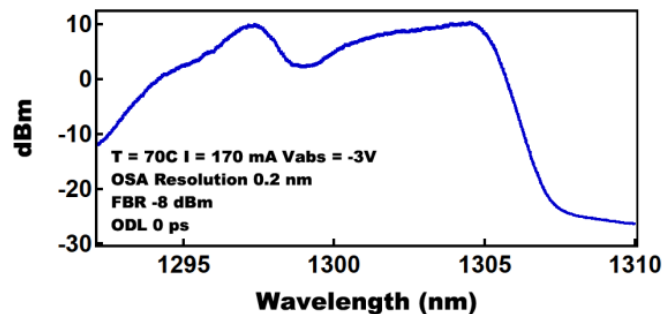
b.)
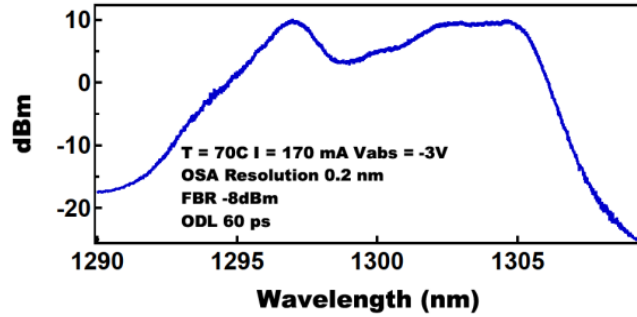
c.)
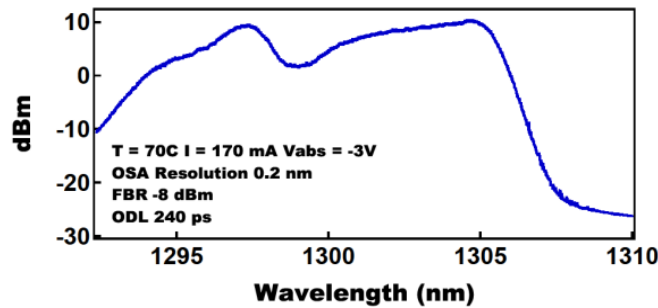
d.)
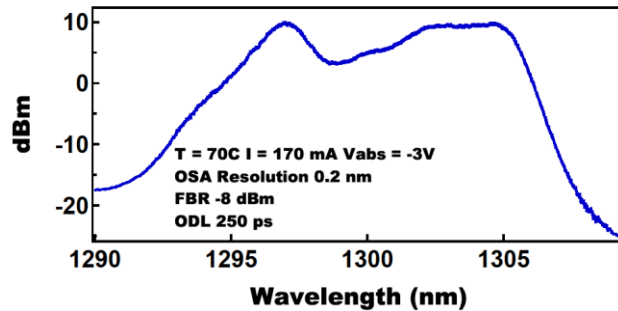
e.)

Figure 5-10: *Optical spectra at T = 70 ℃, I$_{gain}$ = 170 mA, V$_{abs}$ = -3V as a function of optical*

delay: ***a.)*** *Free running* ***b.)*** *0 ps* ***c.)*** *60 ps* ***d.)*** *240 ps and* ***e.)*** *250 ps.*

The impact of varying the delay setting on the optical spectra is seen from a careful

comparison of Fig. 5-10b.) and d.) with the profiles seen in Fig. 5-10c.) and e.). The

spectra in the former case correspond to the nearly-resonant feedback configuration,

characterized by lower RF line widths (47 kHz and 42.5 kHz respectively, seen in Table

5-2), whereas the spectra in the latter case correspond to the non-resonant configuration causing a sudden and drastic enhancement of RF line width (seen in Fig. 5-9a). Interestingly, the perturbation to the optical spectrum as a result of non-resonant feedback appears to be similar to the perturbation caused by the dominance of the QCSE over the spectral hole formation effect for the free-running case(discussed in detail earlier in this chapter) with increasing absorber bias, wherein the spectral hole widens and becomes more shallow.

5.3.2   Effect of Varying the Feedback Strength

i.   RF Spectrum Characterization:

As mentioned before, the strength of applied optical feedback can be adjusted using the variable optical attenuator. Based on this back-reflected power, monitored using a power meter in port 4 of the setup, three broad feedback regimes (FBR) were determined – weak feedback (back-reflected power FBR < -30 dBm), moderate feedback (-30 dBm < back-reflected power FBR < -15 dBm) and strong feedback (back-reflected power FBR > -15 dBm).

As with the case of variable optical delay, the effect of optical feedback as a function of feedback strength for the -3V bias condition is presented first, in view of the severe RF line width broadening observed previously in the free-running configuration. The gain section was pumped at 215 mA, while the optical delay line was set to 0 ps.
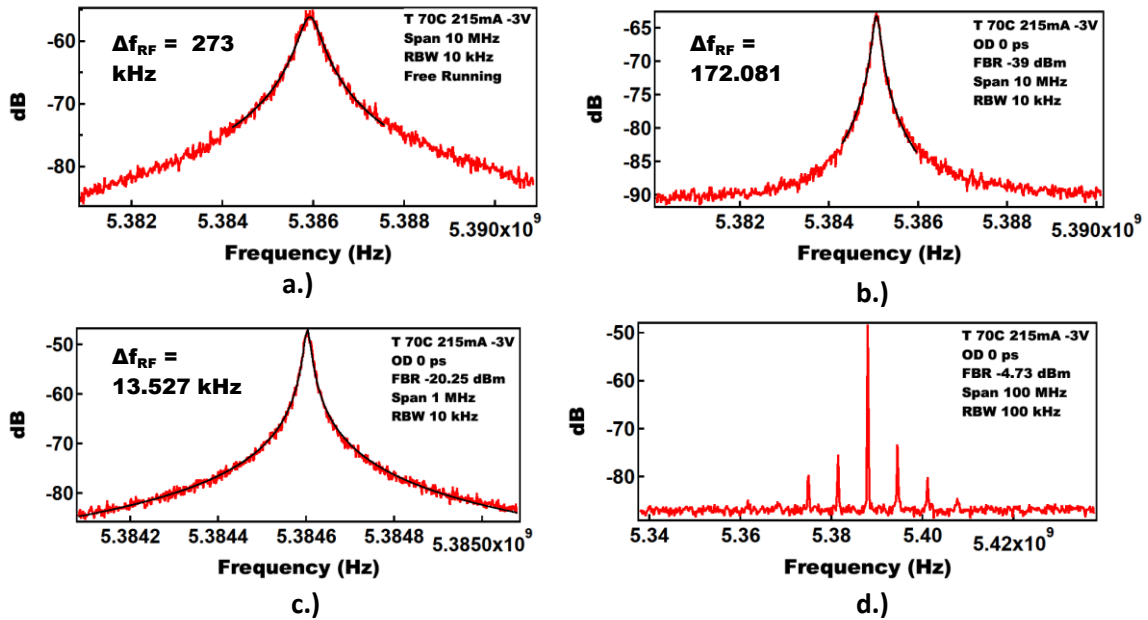
Figure 5-11: *RF Linewidth measurements at T = 70 ℃, I_{gain} = 215 mA, V_{abs} = -3V for different*

back-reflected power values.

The line width data shown in Fig. 5-11 show a clear trend. While weak optical feedback (-39 dBm) helps reduce the line width considerably from 273 kHz for the free-running device to 172.08 kHz, moderate feedback (-20.25 dBm) is much more effective in reducing this figure down to 13.5 kHz (highly desirable for most applications). However, strong feedback (-4.73 dBm) appears to introduce instabilities resembling modulation sidebands surrounding the fundamental frequency, as seen in Fig. 5-11d.

The corresponding set of plots for the -2V absorber bias case show the opposite trend. As seen in Fig. 5-12a, b and c, the free-running configuration shows the best RF performance, with a very low linewidth of 4.5 kHz. This figure broadens slightly to 10.315 kHz under weak external feedback, and continues to broaden as the feedback strength is increased, broadening to nearly 50 kHz at a moderate feedback ratio of -20 dBm. Past -18 dBm, the effect of feedback is to introduce modulation sidebands in the

fundamental peak, as was the case with a -3V absorber bias.
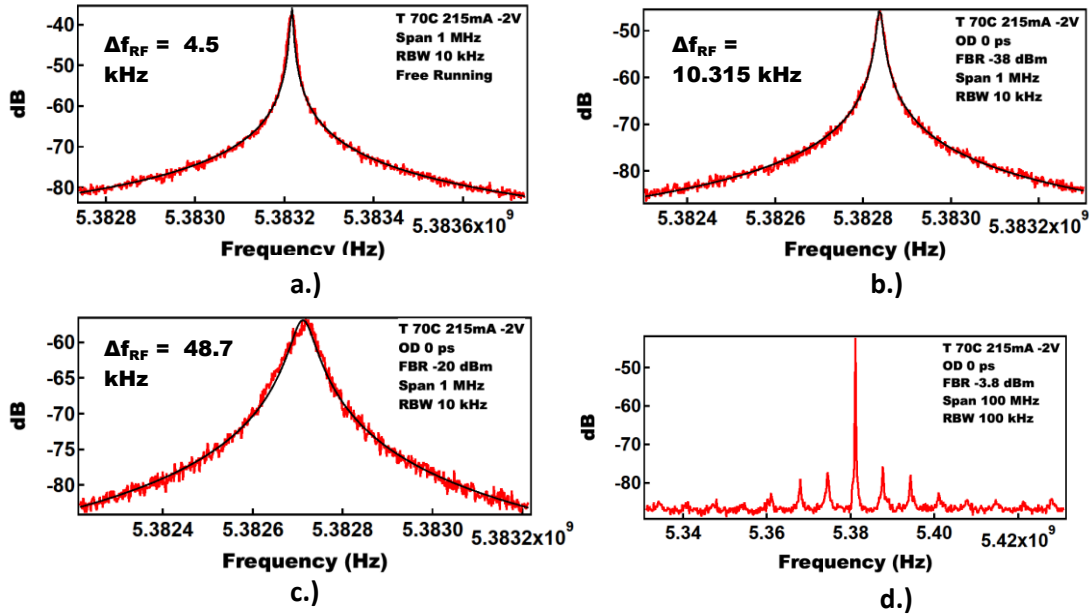
Figure 5-12: *RF Linewidth measurements at T = 70 ℃, I_{gain} = 215 mA, V_{abs} = -2V for different*

back-reflected power values.

This set of trends becomes even more pronounced for an absorber bias condition of -4V, where the line width broadening is much more severe with the application of feedback.
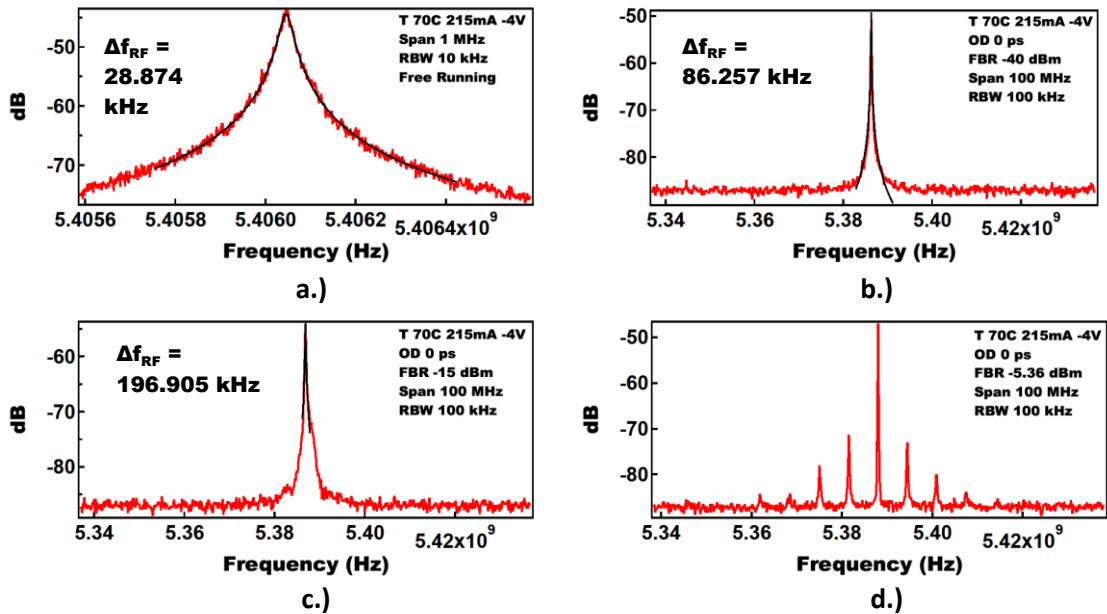
Figure 5-13: *RF Linewidth measurements at T = 70 ℃, I_{gain} = 215 mA, V_{abs} = -4V for different*

back-reflected power values.

147

As seen from Figure 5-13a, b and c, a free-running line width of 28.874 kHz is broadened to 86.257 kHz under weak feedback (-40 dBm), and is further broadened to almost 200 kHz under moderate feedback (-15 dBm). As in previous cases, strong feedback is seen to introduce modulation sidebands into the fundamental peak, as seen in Figure 5-12d for a strong feedback condition of -5.36 dBm.

In order to get further insight into the trends discussed above, it is desirable to study the associated optical spectra.

ii.   Optical Spectrum Characterization:

- **-3V Absorber Bias:**

We recall from Fig. 5-11 a.), b.) and c.) that a dramatic RF performance improvement was observed for the weak and moderate feedback ratio conditions. Consider the behavior of the associated optical spectra, shown below in Fig. 5-14 a.) and b.).

a.)

Figure within plot:

T = 70C I = 215 mA Vabs = -3V
OSA Resolution 0.2 nm
ODL 0 ps
FBR -39 dBm
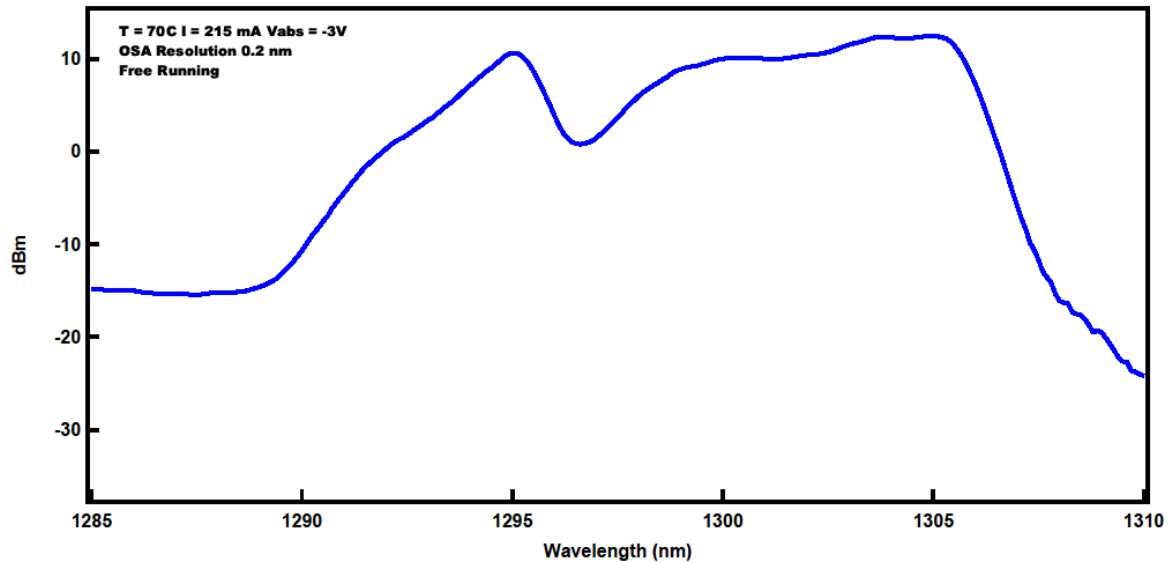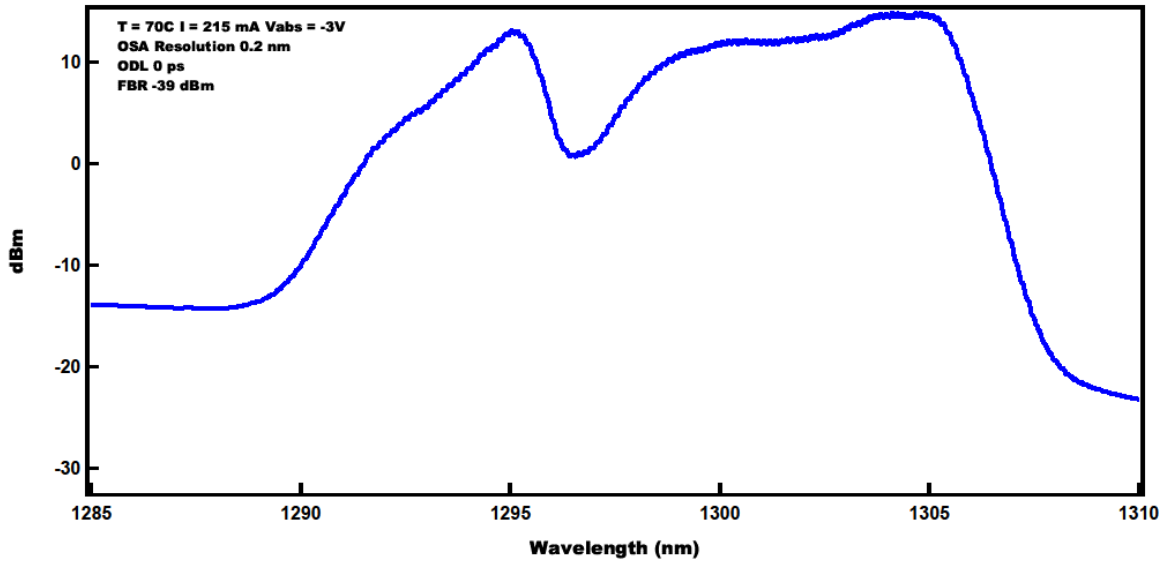
b.)

Figure 5-14: Optical spectra at T = 70 ℃, I_{gain} = 215 mA, V_{abs} = -3V a.) Free-running and b.)

Weak optical feedback (FBR -39 dBm)

As discussed previously in Section 5.2 (Figure 5-6 c.) and Figure 5-14 a.) above), the hole formed in the optical spectrum of free-running device becomes increasingly wider and shallower with increasing absorber bias, a clear indication of the influence of the QCSE beginning to compete with the spectral hole formation effect.

Interestingly, even weak external optical feedback is able to "tip the balance" back in favor of the hole formation effect for this set of operating conditions, as seen from Figure 5-14b, leading to a significant reduction in the RF line width. This effect becomes even stronger in the moderate feedback regime, whereby the spectral hole becomes deeper and sharper, so that the mode-locking process is "sharply peaked" about the center frequency, leading to a drastically reduced RF line width.

- **-2V Absorber Bias:**

As will be seen in this case and the next, the effect discussed above for the -3V bias condition can work both ways, so that a widening of the spectral hole induced by applied optical feedback serves to degrade RF noise performance.
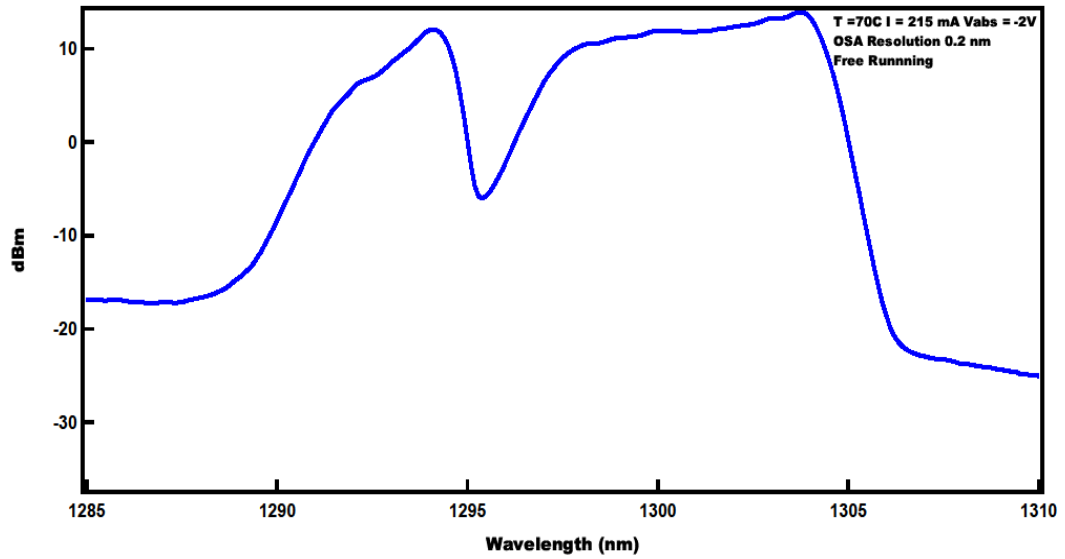
a.)
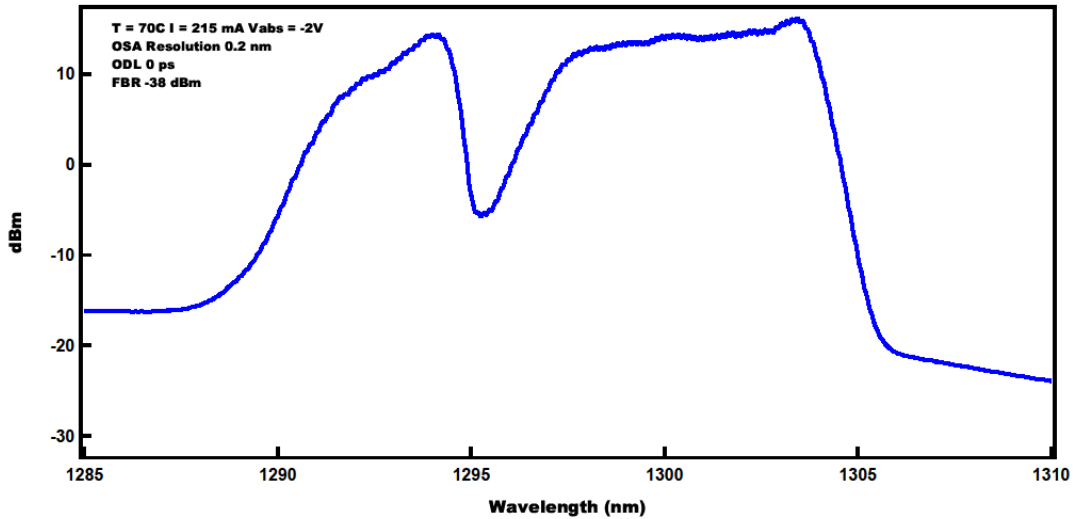
b.)

Figure 5-15: *Optical spectra at T = 70 ℃, I_{gain} = 215 mA, V_{abs} = -2V **a.)** Free-running and*

***b.)** Weak optical feedback (FBR -38 dBm).*

A careful comparison between Fig. 5-15 a.) and b.) reveals the subtle difference between the optical spectra, and, in particular, the corresponding spectral hole shapes for the two cases. The effect of weak optical feedback in this case is to widen the spectral hole slightly, compared to the free-running case. This leads to a slight "flattening" of the bottom tip of the hole, likely triggering a slight mode-competition about the central frequency. This, in turn, causes a slight increase in the RF noise figure, observed directly as a slight increase in the RF linewidth.

- **-4V Absorber Bias:**

The RF measurements presented previously in Fig. 5-13 a.)-d.) suggest that optical feedback also degrades RF noise performance in the -4V absorber bias condition. As in the previous case of a -2V absorber bias condition, the underlying cause for this degradation appears to be a direct consequence of a widening of the spectral hole as a result of the applied feedback, seen in Fig. 5-16.

a.)

T = 70C I = 215 mA Vabs = -4V
OSA Resolution 0.2 nm
ODL 0 ps
FBR -40 dBm
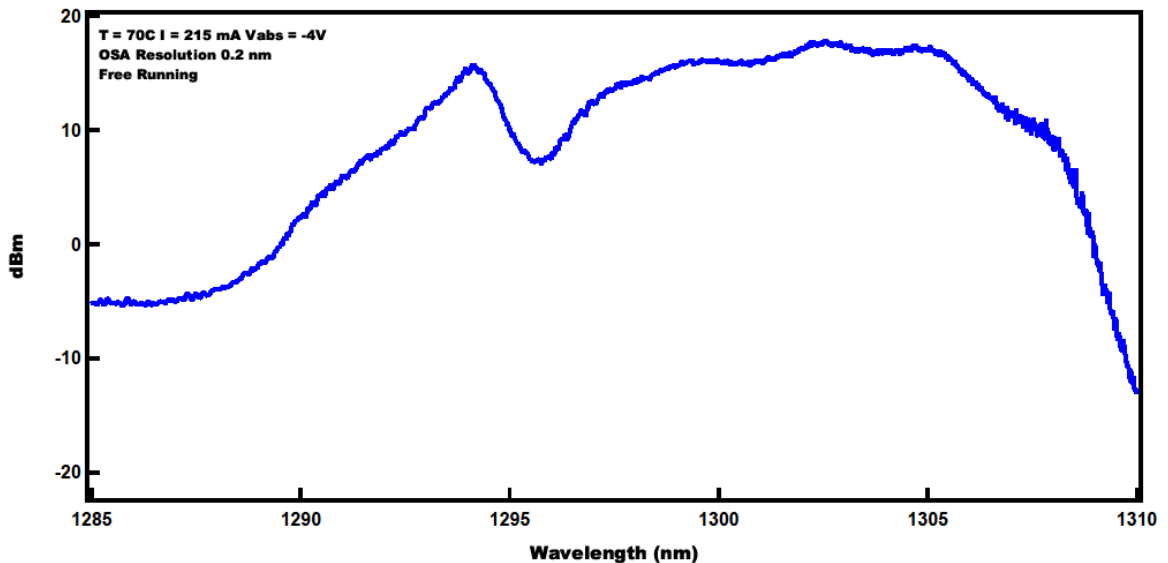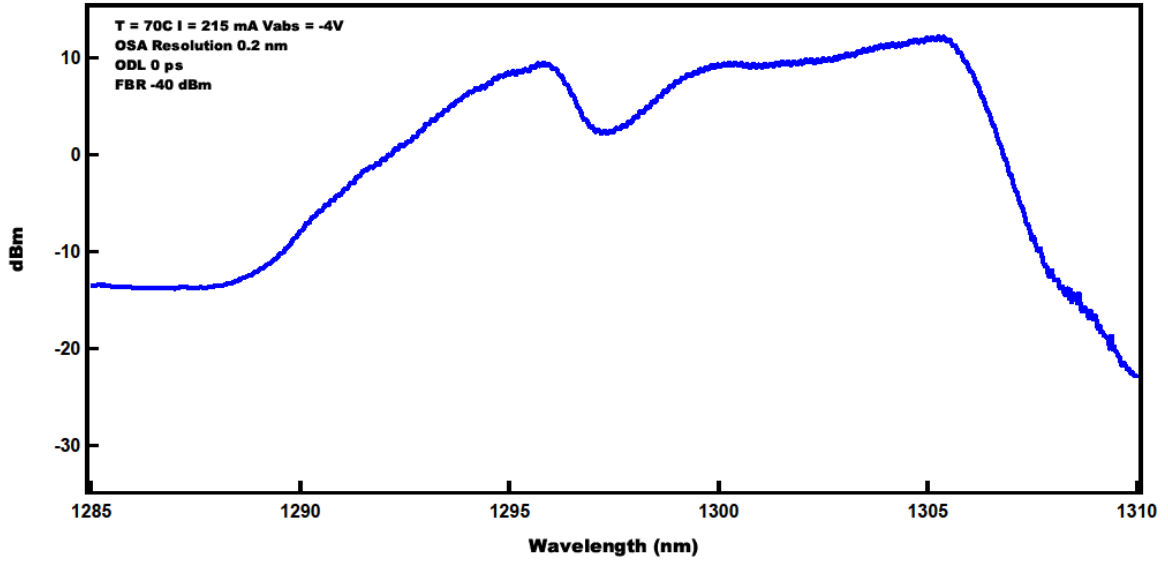
b.)

Figure 5-16: *Optical spectra at T = 70 ℃, I$_{gain}$ = 215 mA, V$_{abs}$ = -4V **a.)** Free-running and*

b.) *Weak optical feedback (FBR -38 dBm)*

The perturbation to the shape of the hole in the spectrum is more pronounced in this case, as compared to the -2V bias condition. Owing to a combination of the increasing dominance of the QCSE at stronger absorber bias voltages and the degradation due to the external optical feedback, a significant widening of the spectral hole occurs, leading to an increased degree of mode-competition about the central wavelength, and the RF noise figure increases significantly from 28.874 kHz for the solitary device to 86.257 kHz for weak optical feedback (-40 dBm).

5.4   Chapter Summary

In devices with an inherent spectral hole formation-tendency, external optical feedback exhibits complicated dynamics that requires careful investigation. In such devices, the interplay between the Spectral Hole Burning (SHB) Effect and the Quantum Confined Stark Effect (QCSE) has been shown previously in [12] to cause wavelength bistability in

the free-running configuration. In this dissertation, this interplay has been shown to also affect the RF noise performance of the device, so that a deep spectral hole with a sharp profile is observed to generally induce a very low RF line width and vice-versa.

Optical feedback adds an additional dimension to this dynamic by either aiding or hindering the shape of the spectral hole. In the former case, the shape of the spectral hole is made deeper and sharper as a result of the feedback, thereby reducing the RF linewidth. This observation supports the findings in [18], where the spectral hole burning process was made highly favorable by use of a wavelength-selective grating to tune the feedback signal to the center frequency of the QD laser.

A comprehensive understanding of the interplay between the above effects in QDMLLs is essential to optimizing high temperature device operation, due to the well-known "walk-off" between gain and absorption peaks at elevated temperatures. While stronger absorber bias voltages have been shown to be an effective technique to mitigate this peak separation and generate better quality pulses [19], the increasing bias voltage is also likely to "wash-out" a deep spectral hole and considerably degrade the RF noise performance of the device, as seen in this chapter. Under these circumstances, external optical feedback, carefully adjusted and optimized to restore the spectral hole to favor the lasing frequency, can offer a simple, yet effective solution to generate stable, high quality pulses with good RF noise performance.

5.5   References for Chapter 5

[1] Grillot, F., Lin, C. Y., Naderi, N. A., Pochet, M., & Lester, L. F. (2009). Optical feedback instabilities in a monolithic InAs/GaAs quantum dot passively mode-locked laser. *Applied Physics Letters*, *94*(15), 153503-153503.

[2] Lin, C. Y., Grillot, F., Naderi, N. A., Li, Y., & Lester, L. F. (2010). rf linewidth reduction in a quantum dot passively mode-locked laser subject to external optical feedback. *Applied Physics Letters*, *96*(5), 051118-051118.

[3] Lin, C. Y., Grillot, F., Li, Y., Raghunathan, R., & Lester, L. F. (2010). Characterization of timing jitter in a 5 GHz quantum dot passively mode-locked laser. *Optics Express*, *18*(21), 21932-21937.

[4] Lin, C. Y., Grillot, F., Li, Y., Raghunathan, R., & Lester, L. F. (2011). Microwave characterization and stabilization of timing jitter in a quantum-dot passively mode-locked laser via external optical feedback. *Selected Topics in Quantum Electronics, IEEE Journal of*, *17*(5), 1311-1317.

[5] Lin, C. Y., Grillot, F., Naderi, N. A., Li, Y., Kim, J. H., Christodoulou, C. G., & Lester, L. F. (2011). RF linewidth of a monolithic quantum dot mode-locked laser under resonant feedback. *IET optoelectronics*, *5*(3), 105-109.

[6] Cataluna, M. A., Rafailov, E. U., McRobbie, A. D., Sibbett, W., Livshits, D. A., & Kovsh, A. R. (2006). Stable mode-locked operation up to 80 C from an InGaAs quantum-dot laser. *Photonics Technology Letters, IEEE*, *18*(14), 1500-1502.

[7] Cataluna, M. A., Viktorov, E. A., Mandel, P., Sibbett, W., Livshits, D. A., Weimert, J., ... & Rafailov, E. U. (2007). Temperature dependence of pulse duration in a mode-locked quantum-dot laser. *Applied Physics Letters*, *90*(10), 101102-101102.

[8] Cataluna, M. A., Malins, D. B., Gomez-Iglesias, A., Sibbett, W., Miller, A., & Rafailov, E. U. (2010). Temperature dependence of electroabsorption dynamics in an InAs quantum-dot saturable absorber at 1.3 μm and its impact on mode-locked quantum-dot lasers. *Applied Physics Letters*, *97*(12), 121110-121110.

[9] Mee, J. K., Crowley, M. T., Patel, N., Murrell, D., Raghunathan, R., Aboketaf, A., ... & Lester, L. F. (2012). A passively mode-locked quantum-dot laser operating over a broad temperature range. *Applied Physics Letters*, *101*(7), 071112-071112.

[10] Mee, J., Crowley, M., Murrell, D., Raghunathan, R., & Lester, L. (2013). Temperature Performance of Monolithic Passively Mode-Locked Quantum Dot Lasers: Experiments and Analytical Modeling.

[11] Huang, X., Stintz, A., Li, H., Rice, A., Liu, G. T., Lester, L. F., ... & Malloy, K. J. (2001). Bistable operation of a two-section 1. 3-micron InAs quantum dot laser-Absorption saturation and the quantum confined stark effect. *IEEE Journal of Quantum Electronics, vol 37*, (3), 414-417.

[12] Feng, M., Brilliant, N. A., Cundiff, S. T., Mirin, R. P., & Silverman, K. L. (2007). Wavelength bistability in two-section mode-locked quantum-dot diode lasers. *Photonics Technology Letters, IEEE*, *19*(11), 804-806.

[13] http://www.rle.mit.edu/sclaser/6.973%20lecture%20notes/Lecture%2013c.pdf

[14] Liboff, R. (1992). *Introductory Quantum Mechanics, 2/e*. Addison-Wesley Publishing Inc.

[15] Malins, D. B. (2008). *Ultrafast dynamics in InAs quantum dot and GaInNAs quantum well semiconductor heterostructures* (Doctoral dissertation, University of St Andrews).

[16] Solgaard, O., & Lau, K. Y. (1993). Optical feedback stabilization of the intensity oscillations in ultrahigh-frequency passively modelocked monolithic quantum-well lasers. *Photonics Technology Letters, IEEE*, *5*(11), 1264-1267.

[17] Avrutin, E. A., & Russell, B. M. (2009). Dynamics and spectra of monolithic mode-locked laser diodes under external optical feedback. *Quantum Electronics, IEEE Journal of*, *45*(11), 1456-1464.

[18] Eliseev, P., Li, H., Stintz, A., Liu, G. T., Newell, T. C., Malloy, K. J., & Lester, L. F. (2000). Tunable grating-coupled laser oscillation and spectral hole burning in an InAs quantum-dot laser diode. *Quantum Electronics, IEEE Journal of*, *36*(4), 479-485.

[19] Crowley, M. T., Murrell, D., Patel, N., Breivik, M., Lin, C. Y., Li, Y., ... & Lester, L. F. (2011). Analytical modeling of the temperature performance of monolithic passively mode-locked quantum dot lasers. *Quantum Electronics, IEEE Journal of*, *47*(8), 1059-1068.

Chapter 6

Summary and Future Work

In this dissertation, a detailed study of the nonlinear dynamical trends of passively mode-locked quantum dot lasers was performed theoretically, using a Delay Differential Equation (DDE) – based modeling scheme, and experimentally, using electrical and optical characterization techniques such as temporal pulse shape and pulse train analysis using a high speed oscilloscope, RF spectrum characterization using an electrical spectrum analyzer and optical spectrum characterization using an optical spectrum analyzer.

The studies undertaken as part of this dissertation resulted in a number of novel and important findings. A chapter-wise summary is given in the following section.

6.1 Dissertation Summary

In chapter 2, a Delay Differential Equation (DDE) model for passive mode-locking in two section semiconductor lasers was introduced as a powerful and versatile, yet computationally less demanding alternative to conventional Traveling Wave models. The following were the key simplifying assumptions made in transforming the Traveling Wave model to the DDE model:

i. The linear cavity was modeled as a ring cavity with unidirectional wave propagation. This allowed for a sequential, lumped-element treatment of the light-matter interaction in each section, thereby simplifying the mathematical complications associated with simultaneous, distributed interactions in all sections.

ii. The barrier-well-dot formalism of the model, which necessitated a comprehensive consideration of dot-to-dot, dot-to-well and other transitions was replaced with a simple rate equation formalism involving a linear dependence on macroscopic carrier concentrations in the gain and the absorber sections. This led to a dramatic simplification in the number of equations and the associated parameter space of the model.

iii. Only ground state lasing was considered.

As a result of the simplifying assumptions in i. – iii. above, the original DDE model (developed in [13] of Chapter 2) comprises a set of three coupled differential equations in the time domain, where the evolution of the intracavity field is described by a delay equation. Not only does this lead to a considerable reduction in the number of model equations, but the simplification of the spatio-temporal evolution of the field to pure temporal evolution enables a substantial reduction of computational cost. In addition, the parameter space of the model is now reduced to a mere 9 parameters. New equations were then derived in order to provide a generalized framework for the transformation of experimentally measured quantities – specifically, gain and absorption measurements on the device under study using the Segmented Contact method ([19] and [20] of Chapter 2) – into dimensionless model parameters to seed the DDE model. This novel scheme greatly enhances the practical utility of the model as an elegant and powerful theoretical guide to next generation device design and analysis.

Chapter 3 served as the first demonstration of how the equations derived in Chapter 2 can be used to transform measurements performed on an actual device over a range of operating conditions into dimensionless inputs for the DDE model, which can then be

used as an extremely powerful tool to gain insight into numerous aspects of the output dynamics of the device. As an added benefit of deriving equations to transform measured quantities into dimensionless model parameters, a novel and innovative technique to estimate the carrier relaxation ratio of the device from basic gain and loss measurements was shown to provide a viable alternative to conventional pump-probe methods. The results of simulation with measurement-extracted parameters indicated the following for stable, fundamental mode-locking in quantum dot devices:

i.   Low values of linewidth enhancement factor in the gain and absorber sections at or near threshold.

ii. Low values of unsaturated gain and absorption for stable locking (which would suggest operation at higher temperatures).

Simulation results also enabled invaluable insight into sudden and unexpected trends in the output dynamics, such as a sudden flipping of the pulse asymmetry, which are typically obscured by autocorrelation measurements. This nonlinear dynamical trend was confirmed for the first time with FROG measurements on the device, while the model was used to acquire insight into the underlying physical mechanism governing the trend by analyzing the interplay between gain and absorber dynamics. This chapter showed numerous instances of how several of the properties unique to QD systems are, in fact, manifest in the parameters extracted from the device, so that the model, in its original form, with no additional equations or parameters can, in itself, act as a robust and powerful theoretical framework to analyze device behavior. This paves the way for device-specific dynamical studies, as discussed in the following section.

Next, in chapter 4, the predictive capabilities of the DDE model were explored in a couple of different contexts of practical importance. With a parameter space of just nine parameters, seven of which can be experimentally-extracted from measurements on the specific device under study, the model offers a powerful theoretical tool to study the nonlinear dynamics unique to that device. First, the model was constrained as usual with measurement-extracted parameters, and the impact of unequal values of the linewidth enhancement factor in the gain and absorber sections on pulse structure was studied. While the results showed a degraded pulse structure for all cases with a significant difference of linewidth enhancement factors in the gain and absorber sections, the instabilities were predicted to be particularly severe for devices with a low gain-bandwidth profile (characterized by lower values of the spectral filtering coefficient γ) operated at lower temperatures, which included a combination of pulse-splitting and satellite lobes. For such devices, operation at higher temperatures was predicted to temper the instabilities to some extent, but they were still found to be significant. Next, for devices with a wide gain-dispersion profile (characterized by higher values of the spectral filtering coefficient γ), a difference of the linewidth enhancement factors in the two sections predicted a closely-related dynamical instability, split-pulsing, wherein the individual pulse structures are characterized by two split lobes, varying in relative intensity over each round trip. The dynamic was interpreted as a synergistic interaction between the lobes of each pulse with the medium, following which the response of the medium was to apply a feedback on the pulse, by perturbing the gain and absorber dynamics of the device, thereby conditioning the pulse shape during each round trip, resulting in one or the other of the two split lobes growing at the expense of the other.

This prediction was confirmed with high-speed oscilloscope measurements of a device fabricated with a wide gain-dispersion profile. In the second part of the chapter, the DDE model was shown to offer a robust predictive modeling capability toward achieving higher pulse repetition rates for two-section, passively mode-locked quantum dot lasers. Consequently, the model was used to first find the regimes of mode-locked operation of a given device wherein the device was predicted to exhibit fundamental or harmonic mode locking, as a function of the dimensionless model parameters. The model parameters were then mapped to externally-controllable parameters (gain section pump current and absorber bias voltage), and the regimes of mode-locked operation were represented on a map, as a function of the parameters that can be interactively controlled while the device is in operation. Excellent agreement was observed between the predictions of the model and high-speed oscilloscope measurements of the output pulse dynamics of fundamental and second-harmonic mode-locking for two devices with a similar epitaxial-layer structure, the first consisting of a 7 mm gain/1 mm absorber section, and the second with a 7.2 mm gain/0.8 mm absorber section (both with a 5-μm ridge waveguide design). A noisy, but stationary pulse-tripling regime was experimentally observed at a bias condition predicted by the model for one particular device. The approach not only presents an invaluable guideline toward achieving higher repetition rates without the need to re-engineer the device, but also points toward the highest repetition rates achievable in principle for a given two-section device.

Finally, in Chapter 5, the effect of externally applied optical feedback at elevated temperature was studied experimentally, and a detailed RF and optical spectral characterization of the device was carried out as a function of optical delay, feedback

ratio and applied absorber bias. It was found that in devices with an inherent spectral hole forming-tendency, external optical feedback exhibits complicated dynamics that requires careful investigation. In such devices, the Spectral Hole Burning (SHB) Effect and the Quantum Confined Stark Effect (QCSE) have been previously shown to compete in the free-running configuration. In this dissertation, this interplay has been shown to also affect the RF noise performance of the device, so that a deep spectral hole with a sharp profile is observed to generally induce a low RF line width and vice-versa. Optical feedback adds an additional dimension to this dynamic by either aiding or hindering the shape of the spectral hole. In the former case, the shape of the spectral hole is made deeper and sharper as a result of the feedback, thereby reducing the RF linewidth. A comprehensive understanding of the interplay between the above effects in QDMLLs is essential to optimizing high temperature device operation, due to the well-known "walk-off" between gain and absorption peaks at elevated temperatures. While stronger absorber bias voltages have been shown to be an effective technique to mitigate this peak separation and generate better quality pulses, the increasing bias voltage is also likely to "wash-out" a deep spectral hole and severely degrade the RF noise performance of the device, as seen in this chapter. Under these circumstances, external optical feedback, carefully adjusted and optimized to restore the spectral hole to favor the lasing frequency, can offer a simple, yet effective solution to generate stable, high quality pulses with good RF noise performance.

6.2   Future Work

As seen from Chapters 2, 3 and 4, the DDE model for passive mode-locking in semiconductor lasers offers a powerful theoretical framework to model QD lasers, where

162

the model parameters are extracted from experimental measurements on the device under study. Using this approach, not only does the model capture various properties specific to QD lasers, but the fact that the parameter space is constrained to measured values provides a simple, yet versatile and powerful framework to investigate the nonlinear dynamics specific to the device under study [1, 2].

This opens up exciting prospects for future investigation as follows. As we might recall from previous chapters, the DDE model has a parameter space of just 9 parameters and using the method developed in [1], 7 of them may be extracted from experimental measurements on the device, leaving an absolute minimum of two free parameters. These two parameters, namely, the linewidth enhancement factors (LEFs) corresponding to the gain and saturable absorber sections, are related to pulse quality measures, such as pulse chirp, RF phase noise and pulse-to-pulse timing jitter. Thus, reducing the LEF to the lowest possible value (ideally 0) is critical to improving pulse quality. Based on the Nonlinear Dynamics – formalism of the Delay model, mathematical ideas such as bifurcation analyses can be used to study the output dynamics of the system as a function of a control parameter that cannot be directly obtained by experimentation – for instance, the LEF. The results of such an analysis can then be compared to the output behavior of the device measured experimentally, in order to get a sense of the values that the LEF might take under a given set of operating conditions.

Furthermore, recent efforts in optically-injected systems involving a combination of experimental measurements and numerical calculations based on a legacy optical – injection model have shown the existence of specific operating points with reduced sensitivity to systemic fluctuations [3, 4]. These techniques expand upon and complement

the recent use of specifically engineered nonlinear oscillators that use nonlinear dynamics to suppress oscillator phase noise. Importantly, the efforts highlight the nontrivial changes in the response of a nonlinear system subjected to external perturbations, and the fact that at specific operating points, nonlinearly-shifted perturbations are suppressed while otherwise appearing similar in characteristics to nearby operating points. This has obvious technological relevance to numerous frequency-reference applications requiring a high degree of precision. It is expected that some of the same techniques, possibly applied to the DDE model, could yield valuable information about stable operating points with reduced sensitivity to systemic fluctuations.

Recent work [5-7] has also shown the role of externally applied optical feedback in reducing RF linewidth, phase noise and pulse-to-pulse timing jitter. However, despite the extensive efforts to study and characterize the RF performance of QD devices, there has been very little progress in characterizing the optical pulse characteristics under externally applied feedback. The novel formalism developed in this dissertation to seed the DDE model with measurement-extracted parameters, can be easily and naturally extended to the case of the DDE model incorporating external optical feedback [8]. Again, the main advantage of this approach is expected to be the fact that by extracting model parameters from the device under study, nonlinear dynamics specific to that particular device under a particular set of operating conditions can be studied.

On the one hand, such an analysis could be used to estimate the values of the LEF that the pulse experiences with and without optical feedback, which can then provide valuable insight into performance metrics such as the pulse chirp and RF phase noise. But more importantly, from the standpoint of technological applications, such a mathematical

model could also be used to calculate the lowest possible value for external cavity length (feedback arm) for which the output dynamics will still be stable. This information is extremely important for the fabrication of a device with a monolithic/on-chip feedback arm, because it provides a design guide for how short the external cavity can be made theoretically, and hence, how small the monolithic device can be made. Also, this can be relevant for the practical design of multi-device systems integrated on a single chip, where such an analysis could provide a mathematical limit for the minimum acceptable separation between adjacent devices.

Pulse compression techniques have received considerable attention in recent years, because of the basic limitations inherent to semiconductor lasers . Unlike other types of lasers (such as solid state and gas lasers), where stimulated emission arises from discrete transitions between atomic or molecular levels, the fundamental physical mechanism governing stimulated emission in semiconductor lasers is band-to-band transitions, owing to their band structure. Thus, pulses generated by mode-locked semiconductor lasers tend to be considerably broader than other types of lasers. The narrowest pulses obtainable from mode-locked QD lasers for instance, are typically on the order of 1-2 ps (compared to < 100 fs easily achievable with solid state lasers). Furthermore, these narrowest pulses are usually observed near threshold, so they tend to be very low power pulses. In order to get high power pulses, the bias conditions have to be well above threshold, but under these circumstances the pulses broaden to several ps. Thus, in order to accomplish the dual-objectives of narrow pulses with high peak power for non-linear optics applications, pulse compression techniques are important to investigate.

For this theme of research, theoretical work could potentially extend the DDE model to include a method to more accurately model the LEF experienced by the pulse as it propagates through the laser cavity. One possible method of implementing such a dynamic variation is to make use of a power-scaling model for the above threshold LEF [9, 10]. Experimental work is proposed to extract the pulse chirp from Frequency Resolved Optical Gating (FROG) measurements. The goal is to investigate whether pulse width reduction and pulse chirp minimization can be accomplished simultaneously, and if so, to what extent. The impact of this research can be easily seen to be of considerable importance, since pulse chirp minimization is critical to telecommunications applications, while pulse width reduction is important for good pulse quality, critical to numerous applications, including non-linear optics applications.

6.3   References for Chapter 6

[1] Raghunathan, R.; Crowley, M.T.; Grillot, F.; Yan Li; Mee, J.K.; Kovanis, V.; Lester, L.F., "Pulse Characterization of Passively Mode-Locked Quantum-Dot Lasers Using a Delay Differential Equation Model Seeded With Measured Parameters," *Selected Topics in Quantum Electronics, IEEE Journal of* , vol.19, no.4, pp.1100311,1100311, July-Aug. 2013.

[2] Raghunathan, R., Mee, J. K., Crowley, M. T., Grillot, F., Kovanis, V., & Lester, L. F. (2013, March). Modeling and characterization of pulse shape and pulse train dynamics in two-section passively mode-locked quantum dot lasers. In *SPIE OPTO* (pp. 86190C-86190C). International Society for Optics and Photonics.

[3] Simpson, T. B., Liu, J. –M., Almulla, M., Usechak, N. G., Kovanis, V., Novel Limit-Cycle Dynamics with Reduced Sensitivity to Perturbations, Phys. Rev. Lett. (submitted).

[4] Simpson, T., Liu, J., AlMulla, M., Usechak, N., & Kovanis, V. (2013). Linewidth Sharpening via Polarization-Rotated Feedback in Optically-Injected Semiconductor Laser Oscillators.

[5] Grillot, F., Lin, C. Y., Naderi, N. A., Pochet, M., & Lester, L. F. (2009). Optical feedback instabilities in a monolithic InAs/GaAs quantum dot passively mode-locked laser. *Applied Physics Letters*, *94*(15), 153503-153503.

[6] Lin, C. Y., Grillot, F., Naderi, N. A., Li, Y., & Lester, L. F. (2010). rf linewidth reduction in a quantum dot passively mode-locked laser subject to external optical feedback. *Applied Physics Letters*, *96*(5), 051118-051118.

[7] Lin, C. Y., Grillot, F., Naderi, N. A., Li, Y., Kim, J. H., Christodoulou, C. G., & Lester, L. F. (2011). RF linewidth of a monolithic quantum dot mode-locked laser under resonant feedback. *IET optoelectronics*, *5*(3), 105-109.

[8] Otto, C., Lüdge, K., Vladimirov, A. G., Wolfrum, M., & Schöll, E. (2012). Delay-induced dynamics and jitter reduction of passively mode-locked semiconductor lasers subject to optical feedback. *New Journal of Physics*, *14*(11), 113033.

[9] Su, H., & Lester, L. F. (2005). Dynamic properties of quantum dot distributed feedback lasers: high speed, linewidth and chirp. *Journal of Physics D: Applied Physics*, *38*(13), 2112.

[10] Grillot, F., Dagens, B., Provost, J. G., Su, H., & Lester, L. F. (2008). Gain Compression and Above-Threshold Linewidth Enhancement Factor in 1.3-< formula formulatype=. *Quantum Electronics, IEEE Journal of*, *44*(10), 946-951.

Appendix A

The Delay Differential Equation (DDE) Model

In order to derive the system of differential equations describing passive mode-locking in a semiconductor laser, the semiconductor laser cavity is modeled as a 4-mirror ring cavity as shown below in Fig. 1 [1]:
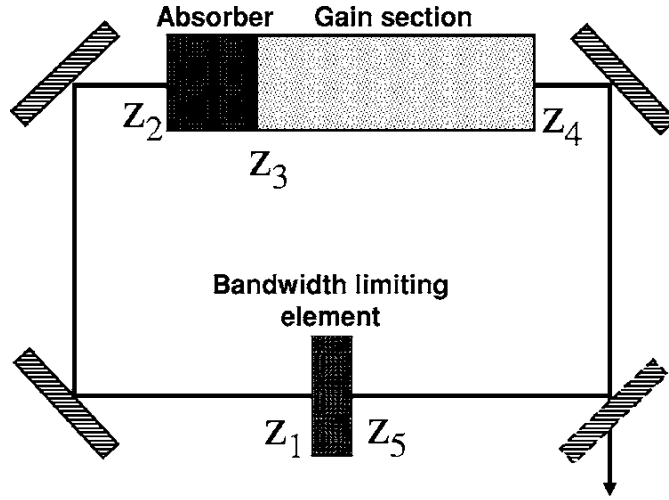
Fig. 1: *Schematic representation of a passively mode-locked, 4-mirror ring laser cavity.*

Coordinate z is measured along the cavity axis. Interval $z_2 < z < z_3 (z_3 < z < z_4)$ corresponds

to the absorbing (amplifying) section. A spectral filtering (bandwidth limiting) element is placed

between $z = z_5$ and $z = z_1 + L$, where L is the total cavity length. Intervals $z_1 < z < z_2$ and

$z_4 < z < z_5$ represent passive medium [1].

The light-matter interactions governing the evolution of the electric field envelope $E(t,z)$ can be represented by a system of traveling-wave equations:

$$\frac{\partial E(t,z)}{\partial z} + \frac{1}{v}\frac{\partial E(t,z)}{\partial t} = \frac{g_k \Gamma_k}{2}(1 - i\alpha_k)[N_k(t,z) - N_k^{tr}]E(t,z)$$

(A1)

$$\frac{\partial N_k(t,z)}{\partial t} = J_k - \frac{N_k(t,z)}{\tau_k} - vg_k\Gamma_k[N_k(t,z) - N_k^{tr}]|E(t,z)|^2$$

(A2)

168

Here, the subscript $k = g (k = q)$ corresponds to the gain (absorber) section. The variables $N_g(t,z)$ and $N_q(t,z)$ describe carrier densities in the gain and absorber sections, respectively. The parameters $N_{g,q}^{tr}$ are the gain and absorber carrier densities evaluated at transparency threshold. The parameter v is the group velocity of the propagating light field, which is assumed to be constant and equal in all five sections. The parameters $\alpha_{g,q}, g_{g,q}, \Gamma_{g,q}$ and $\gamma_{g,q}$ are, respectively, the linewidth enhancement factors, differential gains, transverse modal fill factors and carrier density relaxation rates in the gain and absorber sections. The parameter J_g describes injection current in the gain section. For the absorber section, $J_q = 0$, since the absorber section is not pumped with an injection current, but simply biased with a voltage.

Since the passive sections do not contain gain or absorber material, and consequently, no carrier densities, the evolution of the electric field in these sections may be written as:

$$\frac{\partial E(t,z)}{\partial z} + \frac{1}{v}\frac{\partial E(t,z)}{\partial t} = 0$$

(A3)

Material gain dispersion, including dispersive effects due to artificial elements such as distributed Bragg reflectors, are incorporated through the lumped spectral filtering section. If $\hat{f}(\omega)$ represents the frequency domain spectral filtering function, the transformation of the electric field envelope by this section may be expressed as:

$$\hat{E}(\omega, z + L) = \hat{f}(\omega)\hat{E}(\omega, z_5)$$

(A4)

where, $\hat{E}(\omega, z_5)$ and $\hat{E}(\omega, z_1 + L)$ are the Fourier transforms of $E(t, z_5)$ and $E(t, z_1 + L)$, respectively.

Equations (A1) and (A2) may be re-cast in terms of the normalized coordinates $(t,z) \rightarrow (\tau,\zeta)$, where $\tau = \gamma_q (t - (z/v))$, $\zeta = (z\gamma_q/v)$, and the normalizing factor is the absorber recovery time $\tau_q = (1/\gamma_q)$. The absorber recovery time determines the pulse width, which, in turn, sets the pulse repetition rate, so that the advantage of making this parameter the characteristic timescale is to normalize all quantities in the equation to a critical timescale in the problem, which ensures that there is sufficient temporal resolution to obtain complete information for all constituent processes. With this coordinate transformation, equations (A1) and (A2) may be expressed as:

$$\frac{\partial E(t,z)}{\partial z} + \frac{1}{v}\frac{\partial E(t,z)}{\partial t} = \frac{g_k \Gamma_k}{2}(1 - i\alpha_k)\left[N_k(t,z) - N_k^{tr}\right]E(t,z)$$

$$\Rightarrow \left\{\frac{\partial E(\tau,\zeta)}{\partial \zeta}\frac{\partial \zeta}{\partial z} + \frac{\partial E(\tau,\zeta)}{\partial \tau}\frac{\partial \tau}{\partial z}\right\} + \left(\frac{1}{v}\right)\frac{\partial E(\tau,\zeta)}{\partial \tau}\frac{\partial \tau}{\partial t} = \frac{g_r \Gamma_r}{2}(1 - i\alpha_r)\left[N_r(t,z) - N_r^{tr}\right]E(t,z)$$

$$\Rightarrow \left\{\left(\frac{\gamma_q}{v}\right)\frac{\partial E(\tau,\zeta)}{\partial \zeta} + \left(-\frac{\gamma_q}{v}\right)\frac{\partial E(\tau,\zeta)}{\partial \tau}\right\} + \left(\frac{1}{v}\right)\frac{\partial E(\tau,\zeta)}{\partial \tau}\frac{\partial \tau}{\partial t} = \frac{g_r \Gamma_r}{2}(1 - i\alpha_r)\left[N_r(\tau,\zeta) - N_r^{tr}\right]E(\tau,\zeta)$$

$$\Rightarrow \left(\frac{\gamma_q}{v}\right)\frac{\partial E(\tau,\zeta)}{\partial \zeta} - \left(\frac{\gamma_q}{v}\right)\frac{\partial E(\tau,\zeta)}{\partial \tau} + \left(\frac{\gamma_q}{v}\right)\frac{\partial E(\tau,\zeta)}{\partial \tau} = \frac{g_r \Gamma_r}{2}(1 - i\alpha_r)\left[N_r(\tau,\zeta) - N_r^{tr}\right]E(\tau,\zeta)$$

$$-\left\{\because \frac{\partial \zeta}{\partial z} = \left(\frac{\gamma_q}{v}\right), \frac{\partial \tau}{\partial z} = -\left(\frac{\gamma_q}{v}\right) and \frac{\partial \tau}{\partial t} = \gamma_q\right\}.$$

$$\frac{\partial E(\tau,\zeta)}{\partial \zeta} = \frac{v g_r \Gamma_r}{\gamma_q}\left(\frac{1 - i\alpha_r}{2}\right)\left[N_r(\tau,\zeta) - N_r^{tr}\right]E(\tau,\zeta)$$

(A5)

Similarly, we can use the coordinate transformation above to get expressions for the evolution of the carrier densities in the gain and absorber sections:

$$\frac{\partial N_g(t,z)}{\partial t} = J_g - \gamma_g N_g(t,z) - vg_g\Gamma_g\left[N_g(t,z) - N_g^{tr}\right]|E(t,z)|^2$$

$$\Rightarrow \gamma_q \frac{\partial N(\tau,\zeta)}{\partial \tau} = J_g - \gamma_g N_g(\tau,\zeta) - vg_g\Gamma_g\left[N_g(\tau,\zeta) - N_g^{tr}\right]|E(\tau,\zeta)|^2$$

$$\frac{\partial N_g(\tau,\zeta)}{\partial \tau} = \left(\frac{J_g}{\gamma_q}\right) - \left(\frac{\gamma_g}{\gamma_q}\right)N_g(\tau,\zeta) - \frac{vg_g\Gamma_g}{\gamma_q}\left[N_g(\tau,\zeta) - N_g^{tr}\right]|E(\tau,\zeta)|^2$$

<div align="right">(A6)</div>

$$\frac{\partial N_q(t,z)}{\partial t} = J_q - \gamma_q N_q(t,z) - vg_q\Gamma_q\left[N_q(t,z) - N_q^{tr}\right]|E(t,z)|^2$$

$$\Rightarrow \gamma_q \frac{\partial N_q(\tau,\zeta)}{\partial \tau} = J_q - \gamma_q N_q(\tau,\zeta) - vg_q\Gamma_q\left[N_q(\tau,\zeta) - N_q^{tr}\right]|E(\tau,\zeta)|^2$$

$$\Rightarrow \frac{\partial N_q(\tau,\zeta)}{\partial \tau} = \left(\frac{J_q}{\gamma_q}\right) - N_q(\tau,\zeta) - \frac{vg_q\Gamma_q}{\gamma_q}\left[N_q(\tau,\zeta) - N_q^{tr}\right]|E(\tau,\zeta)|^2$$

<div align="right">(A7)</div>

In order to simplify equations (A5) – (A7) and reduce them to an adimensional form, we perform the following transformations:

$$A(\tau,\zeta) = E(\tau,\zeta)\sqrt{\left(vg_g\Gamma_g/\gamma_q\right)}$$

$$n_{g,q}(\tau,\zeta) = \left(vg_{g,q}\Gamma_{g,q}/\gamma_q\right)\left[N_{g,q}(\tau,\zeta) - N_{g,q}^{tr}\right]$$

$$j_g = \left(vg_g\Gamma_g\left(J_g - \gamma_g N_g^{tr}\right)/\gamma_q^2\right)$$

$$j_q = \left(vg_g\Gamma_g N_q^{tr}/\gamma_q\right)$$

$$\Gamma = \left(\gamma_g/\gamma_q\right) \text{ and } s = \left(g_q\Gamma_q/g_g\Gamma_g\right)$$

<div align="right">(A8)</div>

Multiplying both sides of equation (A5) by $\sqrt{vg_g\Gamma_g/\gamma_q}$, we have:

$$\sqrt{\left(\frac{vg_g\Gamma_g}{\gamma_q}\right)}\frac{\partial E(\tau,\varsigma)}{\partial \varsigma}=\left(\frac{1-i\alpha_r}{2}\right)\left(\frac{vg_r\Gamma_r}{\gamma_q}\right)\left[N_r(\tau,\varsigma)-N_r^{tr}\right]\left\{\sqrt{\left(\frac{vg_g\Gamma_g}{\gamma_q}\right)}E(\tau,\varsigma)\right\}$$

$$\Rightarrow\frac{\partial}{\partial \varsigma}\left(\sqrt{\frac{vg_g\Gamma_g}{\gamma_q}}E(\tau,\varsigma)\right)=\left(\frac{1-i\alpha_r}{2}\right)\left(\frac{vg_r\Gamma_r}{\gamma_g}\right)\left[N_r(\tau,\varsigma)-N_r^{tr}\right]\left\{\sqrt{\left(\frac{vg_g\Gamma_g}{\gamma_q}\right)}E(\tau,\varsigma)\right\}$$

$$\frac{\partial A(\tau,\varsigma)}{\partial \varsigma}=\left(\frac{1-i\alpha_{g,q}}{2}\right)n_{g,q}(\tau,\varsigma)A(\tau,\varsigma)$$

- (using the definitions in (A8) above)

(A9)

Next, multiplying both sides of (A6) by $\left(vg_g\Gamma_g/\gamma_q\right)$, we have:

$$\left(\frac{vg_g\Gamma_g}{\gamma_q}\right)\frac{\partial N_g(\tau,\varsigma)}{\partial \tau}=\left(\frac{vg_g\Gamma_g}{\gamma_q}\right)\left(\frac{J_g}{\gamma_q}\right)-\left(\frac{vg_g\Gamma_g}{\gamma_q}\right)\left(\frac{\gamma_g}{\gamma_q}\right)N_g(\tau,\varsigma)-\left(\frac{vg_g\Gamma_g}{\gamma_q}\right)\left[N_g(\tau,\varsigma)-N_g^{tr}\right]\left(\left(\frac{vg_g\Gamma_g}{\gamma_q}\right)\left|E(\tau,\varsigma)\right|^2\right)$$

Adding and subtracting a factor of $\left(vg_g\Gamma_g/\gamma_q^2\right)\left(\gamma_g N_g^{tr}\right)$ on the right hand side of the

above equation, we get:

$$\frac{\partial}{\partial \tau}\left[\left(\frac{vg_g\Gamma_g}{\gamma_q}\right)\left(N_g(\tau,\varsigma)-N_g^{tr}\right)\right]=\left(\frac{vg_g\Gamma_g}{\gamma_q^2}\right)J_g-\left(\frac{vg_g\Gamma_g}{\gamma_q^2}\right)\left(\gamma_g N_g^{tr}\right)+\left(\frac{vg_g\Gamma_g}{\gamma_q^2}\right)\left(\gamma_g N_g^{tr}\right)-\left(\frac{vg_g\Gamma_g}{\gamma_q}\right)\left(\frac{\gamma_g}{\gamma_q}\right)N_g(\tau,\varsigma)$$

$$-\left(\frac{vg_g\Gamma_g}{\gamma_q}\right)\left[N_g(\tau,\varsigma)-N_g^{tr}\right]\left(\left(\frac{vg_g\Gamma_g}{\gamma_q}\right)\left|E\right|^2\right)$$

$$-\left\{\because \frac{\partial N_g^{tr}}{\partial \tau}=0\right\}$$

$$\Rightarrow \frac{\partial n_g(\tau,\varsigma)}{\partial \tau}=\left(\frac{vg_g\Gamma_g}{\gamma_q^2}\right)\left(J_g-\gamma_g N_g^{tr}\right)-\left(\frac{\gamma_g}{\gamma_q}\right)\left[\left(\frac{vg_g\Gamma_g}{\gamma_q}\right)\left(N_g(\tau,\varsigma)-N_g^{tr}\right)\right]$$

$$-\left[\left(\frac{vg_g\Gamma_g}{\gamma_q}\right)\left(N_g(\tau,\varsigma)-N_g^{tr}\right)\right]\left\{\left(\frac{vg_g\Gamma_g}{\gamma_q}\right)\left|E\right|^2\right\}$$

172

$$\Rightarrow \frac{\partial n_g(\tau,\zeta)}{\partial \tau} = j_g - \Gamma n_g(\tau,\zeta) - n_g(\tau,\zeta)|A(\tau,\zeta)|^2$$

- (using the definitions in (A8) above)

(A10)

Using a similar set of transformations, equation (A7) may be re-expressed as:

$$\frac{\partial n_q(\tau,z)}{\partial \tau} = -j_q - n_q(\tau,z) - sn_q(\tau,z)|A(\tau,z)|^2$$

(A11)

Also, the passive sections have no gain or absorber medium, so that the evolution of the optical field in these sections may be expressed as:

$$\frac{\partial A(\tau,\zeta)}{\partial \zeta} = 0$$

(A12)

From (A12) and the schematic in Fig. 1, we have:

$$A(\tau,\zeta_2) = A(\tau,\zeta_1)$$

and, $A(\tau,\zeta_5) = A(\tau,\zeta_4)$ where, again, $\zeta_k = (z_k \gamma_q / v)$.

(A13)

Next, the evolution of the optical field in the gain and absorber sections may be obtained by integrating equation (A9) in the corresponding section as follows:

- Gain section $(\zeta_3 < \zeta < \zeta_4)$:

$$\frac{\partial A(\tau,\zeta)}{\partial \zeta} = \left(\frac{1-i\alpha_g}{2}\right) n_g(\tau,\zeta) A(\tau,\zeta)$$

$$\Rightarrow \frac{\partial A(\tau,\zeta)}{A(\tau,\zeta)} = \frac{1}{2}(1-i\alpha_g) n_g(\tau,\zeta)\partial \zeta$$

$$\Rightarrow \int_{\zeta_3}^{\zeta_4} \frac{\partial A(\tau,\zeta)}{A(\tau,\zeta)} = \frac{1}{2}(1-i\alpha_g)\int_{\zeta_3}^{\zeta_4} n_g(\tau,\zeta)\partial\zeta$$

$$\Rightarrow \left[\ln|A(\tau,\zeta)|\right]_{\zeta_3}^{\zeta_4} = \frac{1}{2}(1-i\alpha_g)G(\tau), \text{ with } \int_{\zeta_3}^{\zeta_3} n_g(\tau,\zeta)d\zeta = G(\tau) \equiv \text{saturable gain.}$$

Thus, $A(\tau,\zeta_4) = e^{\frac{1}{2}(1-i\alpha_g)G(\tau)} A(\tau,\zeta_3)$

$$(A14)$$

- Absorber section $(\zeta_2 < \zeta < \zeta_3)$:

$$\frac{\partial A(\tau,\zeta)}{\partial\zeta} = \left(\frac{1-i\alpha_q}{2}\right) n_q(\tau,\zeta) A(\tau,\zeta)$$

$$\Rightarrow \int_{\zeta_2}^{\zeta_3} \frac{\partial A(\tau,\zeta)}{A(\tau,\zeta)} = \frac{1}{2}(1-i\alpha_q)\int_{\zeta_2}^{\zeta_3} n_q(\tau,\zeta)\partial\zeta$$

$$\Rightarrow \left[\ln|A(\tau,\zeta)|\right]_{\zeta_2}^{\zeta_3} = -\frac{1}{2}(1-i\alpha_q)Q(\tau), \text{ with } \int_{\zeta_2}^{\zeta_3} n_q(\tau,\zeta)d\zeta = -Q(\tau) \equiv \text{saturable}$$

absorption.

Thus, $A(\tau,\zeta_3) = e^{-\frac{1}{2}(1-i\alpha_q)Q(\tau)} A(\tau,\zeta_2)$

$$(A15)$$

Next, equations (A10) and (A11) need to be integrated over ζ to find the evolution equations of the saturable gain and absorption:

$$\partial_\tau \int_{\zeta_3}^{\zeta_4} dn_g(\tau,\zeta) = \int_{\zeta_3}^{\zeta_4} j_g d\zeta - \Gamma \int_{\zeta_3}^{\zeta_4} n_g(\tau,\zeta)d\zeta - \int_{\zeta_3}^{\zeta_4} n_g(\tau,\zeta)|A(\tau,\zeta)|^2 d\zeta$$

$$\Rightarrow \partial_\tau G(\tau) = g_0 - \Gamma G(\tau) - \int_{\zeta_3}^{\zeta_4} n_g(\tau,\zeta)|A(\tau,\zeta)|^2 d\zeta$$

$$(A16)$$

174

$$\partial_\tau \int_{\zeta_2}^{\zeta_3} dn_q(\tau,\zeta) = \int_{\zeta_2}^{\zeta_3} j_q d\zeta - \int_{\zeta_2}^{\zeta_3} n_q(\tau,\zeta) d\zeta - \int_{\zeta_2}^{\zeta_3} n_q(\tau,\zeta) |A(\tau,\zeta)|^2 d\zeta$$

$$\Rightarrow \partial_\tau Q(\tau) = q_0 - Q(\tau) - s \int_{\zeta_2}^{\zeta_3} n_q(\tau,\zeta) |A(\tau,\zeta)|^2 d\zeta$$

(A17)

In order to evaluate the integral on the right side of equations (A16) and (A17), we use equation (A9) as follows:

$$\frac{\partial A(\tau,\zeta)}{\partial \zeta} = \left(\frac{1-i\alpha_{g,q}}{2} \right) n_{g,q}(\tau,\zeta) A(\tau,\zeta)$$

$$\Rightarrow A^*(\tau,\zeta) \frac{\partial A(\tau,\zeta)}{\partial \zeta} = \left(\frac{1-i\alpha_{g,q}}{2} \right) n_{g,q}(\tau,\zeta) |A(\tau,\zeta)|^2$$

(A18)

$$\text{Also,} \ \left(\frac{\partial A(\tau,\zeta)}{\partial \zeta} \right)^* = \left(\left(\frac{1-i\alpha_{g,q}}{2} \right) n_{g,q}(\tau,\zeta) A(\tau,\zeta) \right)^*$$

$$\Rightarrow \frac{\partial A^*(\tau,\zeta)}{\partial \zeta} = \left(\frac{1+i\alpha_{g,q}}{2} \right) n_{g,q}(\tau,\zeta) A^*(\tau,\zeta)$$

(A19)

And, from (A19), we get:

$$A(\tau,\zeta) \frac{\partial A^*(\tau,\zeta)}{\partial \zeta} = \left(\frac{1+i\alpha_{g,q}}{2} \right) n_{g,q}(\tau,\zeta) |A(\tau,\zeta)|^2$$

(A20)

Adding equations (A18) and (A20), we have:

$$A^*(\tau,\zeta) \frac{\partial A(\tau,\zeta)}{\partial \zeta} + A(\tau,\zeta) \frac{\partial A^*(\tau,\zeta)}{\partial \zeta} = \left[\left(\frac{1-i\alpha_{g,q}+1+i\alpha_{g,q}}{2} \right) n_{g,q}(\tau,\zeta) |A(\tau,\zeta)|^2 \right]$$

$$\Rightarrow \frac{\partial |A(\tau,\zeta)|^2}{\partial \zeta} = n_{g,q}(\tau,\zeta)|A(\tau,\zeta)|^2$$

$$(A21)$$

Integrating (A21) over the gain and absorber sections, we get:

$$\int_{\zeta_3}^{\zeta_4} n_g(\tau,\zeta)|A(\tau,\zeta)|^2 \, d\zeta = -|A(\tau,\zeta_4)|^2 + |A(\tau,\zeta_3)|^2$$

$$(A22)$$

$$\int_{\zeta_2}^{\zeta_3} n_q(\tau,\zeta)|A(\tau,\zeta)|^2 \, d\zeta = -|A(\tau,\zeta_3)|^2 + |A(\tau,\zeta_2)|^2$$

$$(A23)$$

Using (A22) and (A23) in (A16) and (A17) respectively, we get:

$$\Rightarrow \partial_\tau G(\tau) = g_0 - \Gamma G(\tau) - |A(\tau,\zeta_4)|^2 + |A(\tau,\zeta_3)|^2$$

$$(A24)$$

$$\Rightarrow \partial_\tau Q(\tau) = q_0 - Q(\tau) + s|A(\tau,\zeta_3)|^2 - s|A(\tau,\zeta_2)|^2$$

$$(A25)$$

Now, equation (A4) for the spectral filtering element may be expressed in the time domain as:

$$A(\tau,\zeta_1 + T) = \int_{-\infty}^{\tau} f(\tau - \theta)A(s,\zeta_5) \, d\theta$$

$$(A26)$$

where, $T = (\gamma_q L/v)$ is the normalized cold cavity round trip time.

Substituting equations (14) and (15) into (26) and re-expressing the field transformation condition in the form $A(\tau, \zeta + T) = A(\tau + T, \zeta)$, we have:

$$A(\tau + T) = \int_{-\infty}^{\tau} f(\tau - \theta) R(\theta) A(\theta) d\theta$$

(A27)

with, $R(\tau) = \sqrt{\kappa} e^{\left[\left\{(1-i\alpha_g)\frac{G(\tau)}{2}\right\} - \left\{(1-i\alpha_q)\frac{Q(\tau)}{2}\right\}\right]}$.

(A28)

Using a Lorentzian line shape function for the spectral filtering element,

$$f(\tau) = \gamma \exp\left[(-\gamma + i\Omega)\tau\right]$$

(A29)

Substituting (A28) and (A29) into (A27), we get:

$$A(\tau + T) = \int_{-\infty}^{\tau} \gamma \exp\left[(-\gamma + i\Omega)(\tau - \theta)\right] \sqrt{\kappa} \exp\left[\frac{1}{2}\left\{(1 - i\alpha_g)G(\theta) - (1 - i\alpha_q)Q(\theta)\right\}\right] A(\theta) d\theta$$

(A30)

Differentiating both sides of equation (30) w.r.t dimensionless time τ, and using the coordinate change $A \rightarrow A \exp(i\Omega\tau)$, we get:

$$\partial_\tau A(\tau + T) = \frac{\partial}{\partial \tau}\left[\int_{-\infty}^{\tau} \gamma \exp\left\{-\gamma(\tau - \theta)\right\} \sqrt{\kappa} \exp\left(\frac{1}{2}\left\{(1 - i\alpha_g)G(\theta) - (1 - i\alpha_q)Q(\theta)\right\}\right) A(\theta) d\theta\right]$$

$$= \gamma\sqrt{\kappa} \int_{-\infty}^{\tau} \frac{\partial}{\partial \tau}\left[\exp\left\{-\gamma(\tau - \theta)\right\} \exp\left\{\frac{1}{2}(1 - i\alpha_g)G(\theta) - \frac{1}{2}(1 - i\alpha_q)Q(\theta)\right\} A(\theta)\right] d\theta$$

$$= \gamma\sqrt{\kappa} \int_{-\infty}^{\tau} -\gamma \exp\left\{-\gamma(\tau - \theta)\right\} \exp\left\{\frac{1}{2}(1 - i\alpha_g)G(\theta) - \frac{1}{2}(1 - i\alpha_q)Q(\theta)\right\} A(\theta) d\theta$$

$$+ \gamma\sqrt{\kappa} \exp\left\{\frac{1}{2}(1 - i\alpha_g)G(\tau) - \frac{1}{2}(1 - i\alpha_q)Q(\tau)\right\} A(\tau)$$

177

$$- \text{(since } \frac{d}{dt}\left\{\int_{-\infty}^{t} a(t-t')b(t')dt'\right\} = \int_{-\infty}^{t} \frac{da(t-t')}{dt}b(t')dt' + a(0)b(t)).$$

$$\Rightarrow \partial_\tau A(\tau+T) = -\gamma A(\tau+T) + \gamma\sqrt{\kappa}\exp\left\{\left(1-i\alpha_g\right)\frac{G(\tau)}{2} - \left(1-i\alpha_q\right)\frac{Q(\tau)}{2}\right\}A(\tau)$$

Or, equivalently,

$$\partial_\tau A(\tau) + \gamma A(\tau) = \gamma\sqrt{\kappa}\exp\left\{\left(1-i\alpha_g\right)\frac{G(\tau)}{2} - \left(1-i\alpha_q\right)\frac{Q(\tau)}{2}\right\}A(\tau-T)$$

(A31)

Equation (A31) represents a Delay Differential Equation in A.

The equations governing the evolution of the saturable gain and absorption are obtained

from equations (A22) and (A23), by using equations (A13), (A14) and (A15) to express

$A(\tau,\zeta_2), A(\tau,\zeta_3)$ and $A(\tau,\zeta_4)$ in terms of $A(\tau) = A(\tau,\zeta_1)$.

The complete system of equations describing passive mode-locking in a semiconductor

laser may, thus, be expressed in the form:

$$\frac{dA(\tau)}{d\tau} = \gamma\sqrt{\kappa}\exp\left[\frac{1}{2}\left(1-i\alpha_g\right)G(\tau-T) - \frac{1}{2}\left(1-i\alpha_{abs}\right)Q(\tau-T)\right]A(\tau-T) - \gamma A(\tau)$$

$$\frac{dG(\tau)}{d\tau} = g_0 - \Gamma G(\tau) - e^{-Q(\tau)}\left(e^{G(\tau)}-1\right)|A(\tau)|^2$$

$$\frac{dQ(\tau)}{d\tau} = q_0 - Q(\tau) - s\left(1-e^{-Q(\tau)}\right)|A(\tau)|^2$$

(A32)

Thus, we have transformed the spatio-temporal traveling wave equations for light–matter

interaction in a passively mode-locked semiconductor laser cavity from equations (A1)

and (A2) into a system of three coupled differential equations in time alone, one delay

and two ordinary, as seen from (32).

This formalism facilitates the use of the model to analyze the dynamical regimes of operation of a passively mode-locked semiconductor laser using standard techniques such as bifurcation analysis [1, 2].

References for Appendix A

[1]. Vladimirov, A. G., & Turaev, D. (2005). Model for passive mode locking in semiconductor lasers. *Phys. Rev. A*, *72*(3), 033808.

[2]. Usechak, N. G., Xin, Y., Lin, C. Y., Lester, L. F., Kane, D. J., & Kovanis, V. (2009). Modeling and direct electric-field measurements of passively mode-locked quantum-dot lasers. *Selected Topics in Quantum Electronics, IEEE Journal of*, *15*(3), 653-660.